HZB Helmholtz Zentrum Berlin

SCHRIFTENREIHE DES HZB · EXAMENSARBEITEN

Hydrogen Passivation of Polycrystalline Si Thin Film Solar Cells

Benjamin Gorka

Dissertation

Institut für Silizium-Photovoltaik E-I1

Dezember 2010

HZB–B 9

ISSN 1868-5781

Helmholtz-Zentrum Berlin für Materialien und Energie · Hahn-Meitner-Platz 1 · D-14109 Berlin · Telefon +49 30 8062 0 · Telefax +49 30 8062 42181 · www.helmholtz-berlin.de

Hydrogen Passivation of Polycrystalline Si Thin Film Solar Cells

vorgelegt von
Diplom-Physiker

Benjamin Gorka
aus Berlin

Von der Fakultät IV - Elektrotechnik und Informatik
der Technischen Universität Berlin
zur Erlangung des akademischen Grades
Doktor der Naturwissenschaften
Dr. rer. nat.
genehmigte Dissertation

Promotionsausschuss:

Vorsitzender:	Herr Prof. Dr. Christian Boit
Berichter:	Herr Prof. Dr. Bernd Rech
Berichter:	Herr Prof. Dr. Uwe Rau (Forschungszentrum Jülich)

Tag der wissenschaftlichen Aussprache: 17.12.2010

Berlin, 2010
D 83

Contents

Zusammenfassung

Die Wasserstoffpassivierung ist ein zentraler Prozess in der Herstellung von polykristallinen Si (poly-Si) Dünnschichtsolarzellen. Im Rahmen der Arbeit wurde ein RF-Parallelplattenreaktor für die Wasserstoffbehandlung eingesetzt. Schwerpunkte der Untersuchungen waren (i) die Rolle von Plasmaparametern (wie Druck, Elektrodenabstand und Leistung), (ii) die Dynamik der Wasserstoffbehandlung und (iii) das Zusammenspiel aus Passivierung und Materialeigenschaften. Die Charakterisierung erfolgte anhand von Messungen der Leerlaufspannung V_{OC} an poly-Si Referenzzellen.

Durch Messungen der Plasma-Durchschlagspannung V_{brk} wurden optimale Bedingungen für die Passivierung gefunden. Beste Ergebnisse wurden bei Elektrodenabständen erzielt, bei denen V_{brk} für den jeweiligen Druck ein Minimum hatte. Es wurden Plasmasimulationen durchgeführt, die nahe legen, dass dies einer Minimierung der Ionenenergie entspricht. Eine Erhöhung des Wasserstoffgehaltes im Plasma führte dagegen zu keiner Verbesserung der Passivierung. Untersuchungen zur Dynamik zeigten, dass eine Wasserstoffbehandlung bei geringen Temperaturen ($\leq$ 400°C) mehrere Stunden dauert. Dagegen kann diese bei erhöhten Temperaturen von 500°C bis 600°C in nur 10 min (Plateauzeit) erfolgreich durchgeführt werden. Anhaltende Behandlungen führten zu einer Verschlechterung von V_{OC}, vor allem ober- und unterhalb des beobachteten Optimums (<500°C und >600°C). Als alternatives Verfahren zur Herstellung von poly-Si Schichten wurde die Elektronenstrahlverdampfung untersucht. Unterschiedliche Materialeigenschaften wurden durch Variation der Depositionstemperatur $T_{dep} = 200 - 700$°C eingestellt und mithilfe von Raman und ESR untersucht. Große Körner wurden nach Festphasenkristallisation von amorphem Si, das bei 300°C abgeschieden wurde, erreicht. Die Anzahl offener Si-Bindungen konnte mittels Passivierung um etwa eine Größenordnung reduziert werden. Die niedrigste Konzentration von $2.5 \cdot 10^{16}$ cm^{-3} wurde für poly-Si mit den größten Körnern gefunden und steht im Einklang zu den besten Solarzellenergebnissen (nach RTA und Passivierung).

Die Wasserstoffpassivierung von poly-Si Filmen konnte bei hohen Temperaturen von 500°C bis 600°C mittels Plasmabehandlung erfolgreich durchgeführt werden. Jedoch scheinen im Laufe der Plasmabehandlung auch neue Defekte zu entstehen, die mit andauernder Passivierung zu einer Verschlechterung von V_{OC} führen. Dieser Effekt sollte minimiert werden. Um hohe Leerlaufspannungen oberhalb von 450 mV zu erreichen, wird zunehmend auch eine niedrige Rekombination an Grenzflächen wichtig.

Abstract

Hydrogen passivation is a key process step in the fabrication of polycrystalline Si (poly-Si) thin film solar cells. In this work a parallel plate rf plasma setup was used for the hydrogen passivation treatment. The main topics that have been investigated are (i) the role of plasma parameters (like hydrogen pressure, electrode gap and plasma power), (ii) the dynamics of the hydrogen treatment and (iii) passivation of poly-Si with different material properties. Passivation was characterized by measuring the open-circuit voltage V_{OC} of poly-Si reference samples.

Optimum passivation conditions were found by measurements of the breakdown voltage V_{brk} of the plasma for different pressures p and electrode gaps d. For each pressure, the best passivation was achieved at a gap d that corresponded to the minimum in V_{brk}. Plasma simulations were carried out, which indicate that best V_{OC} corresponds to a minimum in ion energy. V_{OC} was not improved by a larger H flux. Investigations of the passivation dynamic showed that a plasma treatment in the lower temperature range (≤ 400°C) is slow and takes several hours for the V_{OC} to saturate. Fast passivation can be successfully achieved at elevated temperatures around 500°C to 600°C with a plateau time of 10 min. It was found that prolonged hydrogenation leads to a loss in V_{OC}, which is less pronounced within the observed optimum temperature range (500°C − 600°C). Electron beam evaporation has been investigated as an alternative method to fabricate poly-Si absorbers. The material properties have been tuned by alteration of substrate temperature $T_{dep} = 200 - 700$°C and were characterized by Raman, ESR and V_{OC} measurements. Largest grains were obtained after solid phase crystallization (SPC) of a-Si, deposited in the temperature range of 300°C. The defect concentration of Si dangling bonds was lowered by passivation by about one order of magnitude. The lowest dangling bond concentration of $2.5 \cdot 10^{16}$ cm^{-3} after passivation was found for poly-Si with largest grains and coincides with best solar cell results, obtained after rapid thermal annealing and hydrogen passivation.

Hydrogen passivation of poly-Si films was successfully achieved with a parallel plate rf H plasma treatment at elevated temperatures around 500°C to 600°C. Yet it seems that treatment induced defect generation causes a loss in V_{OC} with prolonged passivation time and should be minimized. In order to achieve high open circuit voltages larger than 450 mV, in addition to hydrogen passivation, low recombination at the interfaces becomes more and more important.

1 Introduction

Solar cells are photovoltaic (PV) devices that can convert sunlight directly into electricity, providing a clean and decentralized renewable energy source. The PV market in the year 2009 was still dominated by Si wafer based solar cell technology, which amounted to 81 % of the overall market [1]. However, the trend in PV goes towards thin film technologies, in order to reduce production costs and material consumption. Polycrystalline Si (poly-Si) thin films on foreign low cost substrates such as glass offer the potential of high cell efficiencies [2, 3, 4] combined with the advantages of thin film technology and vast Si abundance.

First investigations about low cost polycrystalline Si (poly-Si) thin film solar cells on foreign substrates date well back into the mid 70's [2, 5]. In the recent years noticeable progress has been made. In 2006, first solar modules based on poly-Si on glass substrate have entered into commercial mass production [6, 7]. One of the key process steps relies on defect passivation of the poly-Si layers by a hydrogen treatment, which can potentially multiplicate the efficiency of a poly-Si solar cell [8, 9].

Crystalline Si can be categorized by grain size. Here the following definition will be used:

- monocrystalline Si (c-Si) for single-crystal,
- multicrystalline Si (mc-Si) with an average grain size of > 100 µm
- polycrystalline Si (poly-Si) with an average grain size between 100 µm and 0.1 µm
- microcrystalline (µc-Si) with crystallites smaller than 0.1 µm, usually embedded in an amorphous network.

A poly-Si thin film solar cell consists of fully crystalline poly-Si absorber layer. The complete stack with a typical thickness between one to several micrometers cannot support itself and needs to be grown onto a foreign substrate. The average grain size is between 0.1 µm and 100 µm and hence much smaller than

the grain size of multicrystalline Si. Grain boundaries are source of defects that deteriorate the efficiency of the solar cell. One approach to improve the device quality focuses on increasing the average grain size and thereby reducing grain boundary induced defects. Large grained poly-Si (~10 µm) can be achieved through a method based on aluminum induced crystallization (AIC) of a thin amorphous Si layer [10]. Even larger grained (~100 µm) layers were obtained by laser crystallization of amorphous Si with a scanning cw laser beam [11]. Both methods produce a poly-Si thin film that in a next step can be used as a seed layer for subsequent epitaxial growth of the absorber [12, 13, 14]. Nevertheless, the most successful method to produce poly-Si absorber layers is based on solid phase crystallization (SPC). Amorphous Si layers are annealed in a furnace at typically 600°C for several hours until a completely crystallized poly-Si film is formed (grain size: 1-3 µm). Matsuyama et al. (Sanyo) could demonstrate a cell efficiency of 9.2% [15]. CSG Solar recently achieved a mini module efficiency of 10.4% [4] and is to date the first and only company that went into industrial production of poly-Si thin film solar cells [7].

Poly-Si films exhibit numerous extended and point defects mainly in the form of Si dangling bonds. These dangling bonds form electrically active defect states within the bandgap, which act as recombination centers for charge carriers and thus deteriorate the device quality. Hydrogen has the ability to diffuse in Si and in particular to bond to dangling bonds, resulting in a passivation of the defects [16]. However, due to the high process temperatures almost no hydrogen remains in the poly-Si layers. Therefore hydrogen needs to be introduced by post-deposition exposure to atomic hydrogen.

First studies about hydrogen in Si date back to the 1950s, when Van Wieringen and Warmoltz determined diffusion coefficient and activation energy for hydrogen diffusion in single crystal silicon [17]. Great interest in hydrogen arose with the discovery in 1976 that incorporation of H strongly improves the properties of amorphous Si [18]. Amorphous Si lacks any long range order and exhibits a high degree of unpaired Si bonds. Hydrogen can passivate the unpaired Si dangling bonds which otherwise form defect states in the band gap of a-Si and act as recombination centers for the charge carriers [19].

A similar beneficial effect has also been found for grain-boundary passivation by H in poly-Si [20, 21, 16]. First studies, performed in 1979 by Seager et al. on hydrogen plasma treatments of grain boundaries in mc-Si, demonstrated a significant reduction of potential barrier and density of states due to the plasma treatment [21]. In the following year the authors could report on

the improvement of the dark-current IV characteristic of poly-Si solar cell structures by H plasma treatment [22].

Since then hydrogen passivation has been recognized as an essential process step in many solar cell concepts. For industrial bulk passivation of wafer based mc-Si solar cells, hydrogen passivation is done by firing of hydrogenated Si nitride (SiN:H) [23]. Hydrogen containing SiN films are deposited onto the surface of mc-Si wafers and hydrogen is driven into the material during an anneal for some seconds at temperatures of around 750°C [23]. However, in case of poly-Si thin film solar cells, a hydrogen plasma treatment at 400°C for 30 min is able to supply a larger amount of hydrogen [24, 25]. Compared to SiN:H firing, plasma hydrogenation consistently led to better solar cell results, as well [25].

Higher substrate temperatures during plasma treatments have been investigated by CSG-Solar AG. It was observed that poly-Si films were most effectively hydrogenated (in terms of cell performance) at rather high temperatures of ~610°C, resulting in a strong improvement of the open circuit voltage from 233 mV to 497 mV [8]. Stimulated by this report other groups have successfully applied temperatures above 600°C [26, 27, 28, 29]. Temperature dependence was investigated by Fosca et al. in the temperature range of 200 - 550°C [30]. The authors found an optimum temperature of 450°C with respect to open circuit voltage of poly-Si solar cells. Research by Carnel et al. indicated an optimum at 420°C [9], although later results on open circuit voltage showed no strong influence in the range of 265 - 440°C [25]. However Carnel et al. reported a much stronger dependence of open circuit voltage on the pressure with an optimum at around 2 mbar [9]. Especially towards smaller pressures (0.5 mbar) the open circuit voltage fell off sharply.

So far the question how the best H plasma treatment can be achieved is still not answered. In particular results about the optimum substrate temperature during plasma process diverge and there is a broad range of applied and optimum temperatures. Plasma parameters like pressure can have a significant impact on the final result. In order to establish a better understanding of the H plasma process further research is required.

This work therefore will focus on researching thoroughly important process parameters (like temperature and duration) and plasma parameters (like pressure, geometrical setup and plasma power). The structure is the following:

Chapter 2 presents fundamental knowledge about hydrogen diffusion and defect passivation in Si. In addition a short overview is given about existing

sources for hydrogenation of Si and the state-of-the-art of hydrogen passivation of poly-Si thin film solar cells.

Chapter 3 responds to sample preparation and characterization. Experimental setups used for rapid thermal annealing (RTA) and hydrogen passivation (HP) are described in detail.

The further chapters are dedicated to the experimental results.

Chapter 4 investigates the role of plasma parameters like hydrogen pressure, electrode gap and plasma power. These parameters could have a significant impact on hydrogen density, ion bombardment and on solar cell performance. To establish a better understanding, simulations of the plasma reactor are presented.

Chapter 5 reports on the dynamics of the hydrogen treatment, i.e. the time and temperature dependence within the temperature range of 350 - 650°C. Hydrogen diffusion will be mainly affected by those two parameters.

Chapter 6 researches the interaction of passivation and material properties. Solar cells based on poly-Si absorbers, deposited by electron beam evaporation (EBE) are fabricated. The material properties of these layers are varied by tuning the deposition temperature in the range of $T_{dep} = 200 - 700$°C. In this context also defect annealing by RTA is investigated.

Chapter 7 aims to establish a link between the measured open-circuit voltage data and the material properties in terms of an effective diffusion length.

Chapter 8 is devoted to a final discussion of the results before finally concluding in **Chapter 9**.

2 Fundamentals

The general aim of the investigation of hydrogen passivation of poly-Si thin film solar cells is to understand and control the dynamics of the hydrogen treatment in terms of H diffusion and defect passivation for the purpose of achieving high material quality and best solar cell performance. In order to understand the dynamics of hydrogen passivation, the first part of this chapter provides an overview of hydrogen diffusion in mono-, multi- and polycrystalline Si.

There exist several techniques to introduce H into Si bulk material. Possible sources for hydrogenation include molecular H_2 sources, plasma sources and H originating from hydrogenated Si nitride. This will be covered within the second section where a general introduction is given to the different hydrogenation methods.

Hydrogen passivation of defects and grain boundaries in poly-Si has been widely studied. It has been successfully applied to mc-Si and poly-Si solar cells, resulting in improvements of cell efficiencies. Investigations and results that have preceded this work or have been obtained simultaneously are summarized in the last section addressing the state-of-the-art of HP of poly-Si solar cells.

2.1 Hydrogen Diffusion and Passivation in Si

Great interest in hydrogen in semiconductors arose with the discovery of the fact that the incorporation of H strongly improved the properties of amorphous Si (aSi:H) [18]. This improvement is due to the ability of H to passivate Si dangling bonds which otherwise form defect states in the band gap of a-Si and act as recombination centers for the charge carriers [19]. A similar beneficial effect has also been found for grain-boundary passivation by H in poly-Si [20, 21, 16]. Since then H has received attention in various fields, such as to passivate Si-SiO_2 interfaces of metal-oxide-semiconductor (MOS) devices [31, 32] and poly-Si grain boundaries for thin-film transistor (TFT) display applications [33, 34, 35].

In the following sections a short overview about hydrogen diffusion and hydrogen passivation in Si will be given. It should be noted that a complete description of this topic goes well beyond the scope of this chapter. For profound reading, the reader may be referred to Refs. [36, 37, 38, 39, 40].

2.1.1 Hydrogen Diffusion in Monocrystalline Si

The diffusion of hydrogen in single crystal silicon (c-Si) follows Fick's law, where in one dimension the flux $J(x)$ is proportional to the gradient of the concentration $C(x)$

$$J(x) = -D \cdot \frac{\partial C(x)}{\partial x} \tag{2.1}$$

D is the diffusion coefficient of H in Si. The second Fick's law states how the concentration will change over time

$$\frac{\partial C(x)}{\partial t} = D \cdot \frac{\partial^2 C(x)}{\partial x^2} \tag{2.2}$$

A simple solution to this problem can be given for the special case, where the concentration at the Si surface ($x = 0$) is kept constant: $C(x = 0, t) = C_0$ and $C(x > 0, t = 0) = 0$. The solution then is given by:

$$C(x,t) = C_0 \cdot \mathrm{erfc}\left(\frac{x}{2\sqrt{Dt}}\right) \tag{2.3}$$

and $l_{dif} = 2\sqrt{Dt}$ can be defined as the diffusion length, where the concentration will have decayed to $0.157 \times C_0$.

The diffusivity of H was first investigated in the 1950s by Van Wieringen and Warmoltz (VWW) (VWW('56) in Fig. 2.1). They showed that within the temperature range of ~1100-1200°C hydrogen diffuses in single crystal silicon with a low activation energy of $E_A = 0.48$ eV [17]

$$D = D_0 \cdot \exp\left(-\frac{E_A}{kT}\right) \tag{2.4}$$

Here k is the Stefan-Boltzmann constant and T the absolute temperature. D_0 was determined to be $9.67 \cdot 10^{-3}$ cm^2/s [17]. A number of subsequent studies at lower temperatures and for low H and low impurity concentrations confirmed the extrapolated diffusivity determined by Van Wieringen and Warmoltz (Fig. 2.1[41, 42, 43, 44, 45], overview taken from Ref. [23]).

Grey symbols in Fig. 2.1 show the diffusion coefficients for the impurities

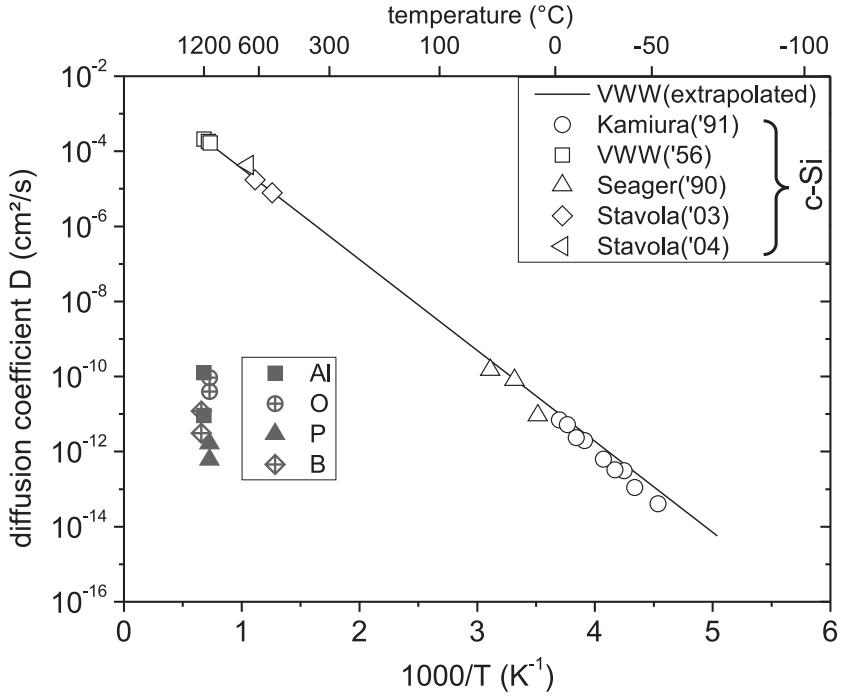

Figure 2.1: Selected data for the diffusion coefficient of H (or D) in c-Si, as determined by Van Wieringen and Warmoltz (VWW) (VWW('56) [17] and other groups [23]. Also shown are diffusion coefficients for the impurities Al, O, P, and B.

Al, O, P, and B for comparison. The values are taken from Ref. [46, 47] (for Al), [48, 49] (for O), [50, 51](for P) and [52, 53] (for B), respectively. They are shown for a temperature between 1100°C and 1250°C to illustrate the difference in diffusivity of more than 6 orders of magnitude, compared to diffusion of hydrogen in c-Si. Also the activation energy is higher ($\geq$ 2.5 eV for O and P and $\geq$ 3 eV for B and Al), which leads to a steeper slope of the diffusivity with temperature [46, 47, 48, 49, 50, 51, 52, 53].

Mobile H that takes part in diffusion can be present in three different charge states H^+, H^0, H^- in c-Si. The positive charge state H^+ is most stable at the bond-center (BC) site in c-Si due to the high electronic charge density of the covalent bonding. It forms a three-center bond with the two adjacent Si atoms and acts as a donor. The donor level is located at about 200 meV below the conduction band [54]. In its neutral charge state, H^0 still prefers the BC site, but because of the extra electron the H^0 state is less stable and therefore unoccupied. In the negative charge state (H^-), H can be found at the tetrahedral interstitial site T_d and acts as an acceptor. The acceptor level is located at about 600 meV below the conduction band [54]. Because H can be found in both charge states (i.e. $H^+$and H^-) it is also called an amphoteric

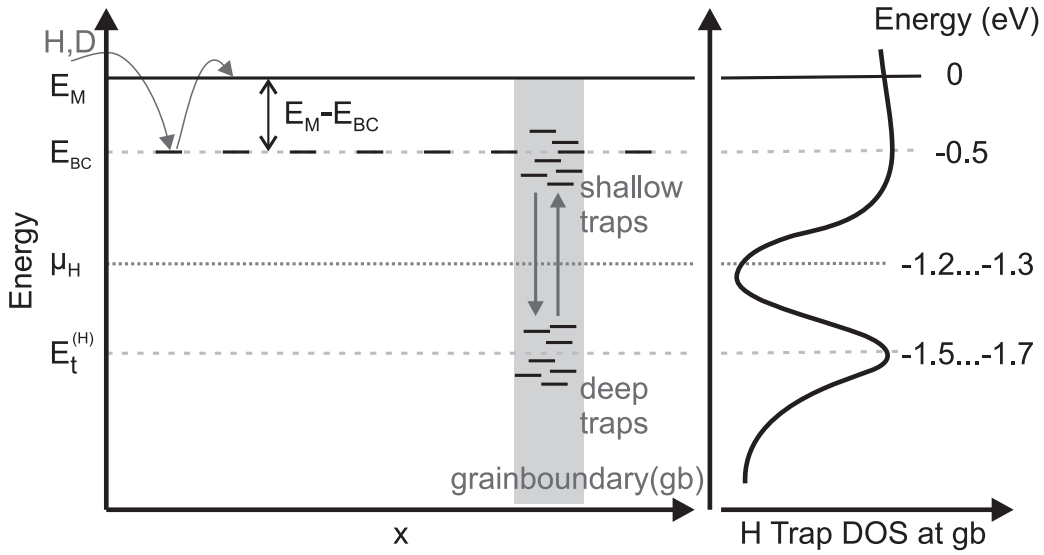

Figure 2.2: Illustration of the H diffusion mechanism in c-Si and poly-Si (after [55]). E_{BC} and E_M represent the energy levels for the Si-Si bond-center position for H and the migration barrier for interstitial H diffusion in c-Si, respectively. Strained Si-Si bonds and Si dangling bonds, originating from grain boundaries lead to additional shallow and deep traps for H diffusion, with energy levels at E_{BC} and $E_t^{(H)}$, respectively . At the right hand side the corresponding density-of-states (DOS) distribution of H traps is illustrated.

impurity.

The diffusion mechanism for monocrystalline p-type Si (and poly-Si, which will be discussed in the next section) is illustrated in Fig. 2.2. As just learned, mobile hydrogen is situated at the Si-Si bond-center (BC) position. To diffuse between sites, H must overcome the energy barrier $E_M - E_{BC}$ (illustrated on the left hand side in Fig. 2.2). E_{BC} and E_M represent the energies for the bond-center position and the migration barrier for interstitial diffusion, respectively. The energy difference corresponds to the activation energy for H diffusion in Eq. 2.4, as by determined by Van Wieringen and Warmoltz [17]. In n-type c-Si hydrogen diffuses via T_d sites in the negative H^- charge state.

2.1.2 Trap-limited Hydrogen Diffusion in Silicon

It is now broadly accepted, that the diffusivity determined by Van Wieringen and Warmoltz [17] is consistent with diffusion of H^+ in Si at low H and impurity concentrations, where H^+ does not interact with other species [56, 57, 23]. However, under non-perfect conditions, with high concentrations of impurities or defects and hydrogenation of doped material by plasma, the effective diffu-

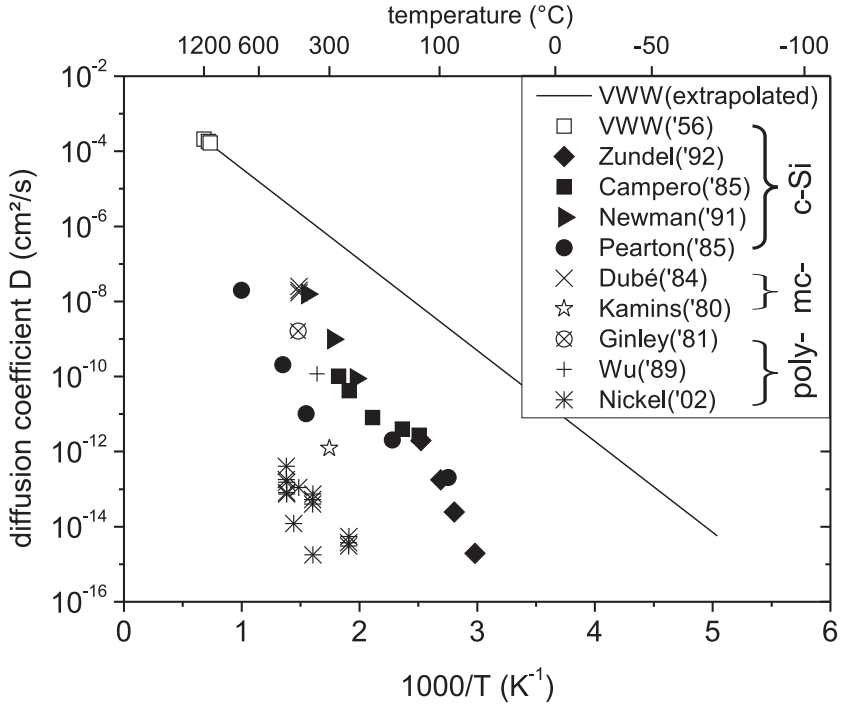

Figure 2.3: Selected data for the diffusion coefficient of H (or D) in different Si materials and under different conditions [23]. See text for details.

sivity of H can differ from the ideal case. In comparison to monocrystalline Si, multicrystalline (mc-Si) and polycrystalline Si (poly-Si) exhibit higher defect densities, due to a large number of grain boundaries and intra-grain defects. As a consequence, H diffusion differs from the diffusion in monocrystalline Si and can be quite similar to diffusion in disordered a-Si. H diffusion in poly-Si has been widely investigated by Nickel and co-workers [16, 58, 55, 40]. Secondary-ion-mass spectroscopy (SIMS) is certainly the most prominent technique to observe the diffusion of hydrogen. Concentration profiles can be obtained and to achieve a better sensitivity usually the isotope deuterium is used which duplicates hydrogen chemistry.

Fig. 2.3 shows the diffusion coefficient of H in Si for different experimental conditions (overview taken from Ref. [23]). Filled symbols in Fig. 2.3 reveal that H diffusion in c-Si scatters and is 2-9 orders of magnitude lower than the prediction by Van Wieringen and Warmoltz [17] (solid line). This difference is due to significant H either trapped by impurities, dopants, defects or forming H_2 molecules [59, 56, 40]. Data in Fig. 2.3 include H diffusion in boron-doped c-Si (Zundel('92) [60]), diffusion in the presence of Au (Pearton('85) and Campero('85) [61, 62]) and H interacting with oxygen (Newman('91) [63]).

The same phenomenon can be evidenced in the presence of grain boundaries

for mc-Si and poly-Si (cross symbols). The high defect concentration traps H very efficiently and significantly restrains the diffusivity [64, 55]. Grain boundary diffusion in mc-Si was first time observed using the electron beam induced current (EBIC) mode of the scanning electron microscopy (SEM) and lower diffusivity compared to bulk diffusion was observed (Dube('84) [65]). Work on H diffusion in poly-Si (Kamins('80), Ginley('81), Wu('89) and Nickel('99) [33, 66, 67, 40]) showed similar results of a high scattering and a much slower H diffusion.

It was suggested, that the presence of numerous defects in form of Si dangling bonds and strained Si—Si bonds act as deep traps for H migration as illustrated in Fig. 2.2 [38, 40]. The energetic distribution of these defects is around the energy level $E_t^{(H)}$. H is captured and released from these traps. Indicated at the right hand side is the density-of-states distribution for H at the grain boundary. The occupation of the states is, similarly to the Fermi-level for electrons, determined by the hydrogen chemical potential μ_H. Experimentally it was observed that the diffusion profile differed from the typical erfc shape in low-pressure CVD (LPCVD) grown poly-Si [55]. Below a critical H concentration the profiles exhibited a kink and an exponential decay in the concentration was evidenced. The difference can be attributed to trap-limited diffusion [40]. In addition it was also found that the diffusion depended on the Fermi-level [40]. This can be explained by H trapping-release processes of deep traps via Si—H bonds, which require a change of the charge state of H. When trapped at a Si dangling bond, it forms a neutral Si-H bond. To be released, H needs to change its charge state to H^+ or H^- in p-type and n-type Si, respectively. The additional charge is provided by the semiconductor, which leads to a Fermi-level dependent activation energy. Once H diffuses within the transport states (BC and T_d sites), the charge state does not change and the diffusion barrier (E_M) will be independent on the Fermi level. A detailed description about trap-limited hydrogen diffusion in poly-Si can be found in [40].

2.1.3 Passivation of Defects

The most prominent defects in poly-Si are Si dangling bonds originating from under-coordinated Si atoms. This results in an unpaired electron of the Si dangling bond whose energy level will move into the band gap. The Si dangling bond has three different charge states (D^+, D^-, D^0) and tends to occupy mostly the neutral charge state D^0, pinning the Fermi level at around midgap.

Because of the unpaired electron the neutral dangling bond is paramagnetic and can be detected by electron spin resonance (ESR) measurements (Sec. 3.3.2). Hydrogen can easily bind to the unpaired Si dangling bond [68]. This will eliminate the associated defect states of the Si dangling bond from within the band gap, passivating the dangling bond defect.

Besides this beneficial passivation effect of dangling bonds, H is also able to passivate shallow dopant impurities. A deactivation or passivation was observed for B in p-type Si [69, 70, 71] and not that severely for P in n-type Si[72] at low temperatures. The B-H complex is however not very temperature stable and dissociates at temperatures above 220 °C [73]. Passivation of other shallow defects by H was also observed for Al, Ga, In, As and Sb [74, 75].

Interaction of H with deep level defects associated with transition metals has been investigated with deep-level transient spectroscopy. Deep levels related to Au, Cu, Ni, Pd, Pt and Cr could be passivated by H [76, 77, 78, 79]. For other defects, like Ti or V, no passivation effect was observed [79]. Hydrogen induced generation of acceptor-like states in intentionally undoped n-type poly-Si was observed upon prolonged hydrogenation [80, 81]. H is also known to form interstitial H_2 [82] and two-dimensional H clusters (platelets) [83, 84].

2.2 Sources for Hydrogenation of Si

Atomic H is required for the passivation of defects in Si. For a-Si it was demonstrated that in order to passivate Si dangling bonds, atomic hydrogen is needed [85, 20]. Furthermore, molecular H_2 is rather immobile compared to atomic H in bulk Si [86]. Therefore H must be introduced into Si via atomic H. There are several ways to introduce atomic H into bulk Si [87]. In the following section, methods will be discussed that can provide atomic H for hydrogenation and defect passivation of poly-Si.

2.2.1 Molecular H_2 Source

The investigations on H diffusion by Van Wieringen and Warmoltz were conducted in molecular H_2 ambient in the temperature range of 1092 °C and 1200°C [17]. This seems to be contradictory to the fact thatH_2 can be atomized by heating only at high temperatures (~2000 °C) [88]. The adsorption energy barrier for H_2 on a perfect Si surface was determined to be 0.8 eV [89]. Nevertheless, H passivation from a molecular H_2 source is reported also

elsewhere for lower temperatures [90, 91]. In conjunction with dopant passivation studies it was found that bulk passivation of shallow impurities could be achieved by annealing in H_2 at temperatures > 900 °C, followed by a rapid quench [91].

One possible explanation on how the molecular H_2 dissociates is given by *ab initio* tight-binding molecular-dynamic simulations. The calculations concluded that interstitial H_2 spontaneously dissociates when placed inside a vacancy. Interstitial H_2 cannot remain in molecular form inside such a defect [92]. The configuration does not feature a local minimum in potential energy, but is unstable resulting in two Si—H bonds. Secondary-ion mass spectrometry studies showed no hydrogenation effects from the exposure of a perfect surface to H_2 (~1 h, 400 °C). Under the same conditions, H penetration of 6-8 mm was observed after softly damaging the Si surface with a cotton swab and a 0.3 micron abrasion [92, 93]. Since damaging the surface produces strained Si—Si bonds, H_2 can readily dissociate and bind to the surface. For surfaces it can be concluded, that hydrogenation from a molecular H_2 gas source at a few hundred degrees Celsius is very inefficient, except in the presence of surface damage [92, 94].

2.2.2 Plasma Sources

A plasma represents an effective method to dissociate H_2 gas and provide sufficient atomic H for passivation. Plasma is often called a fourth state of matter. It contains a quasi-neutral confinement of ionized species in which the density of negatively charged species is well balanced by the density of positively charged species. Depending on how the plasma is excited, it can be divided into:

- direct current (DC) glow discharges: the plasma is ignited by an arch discharge
- capacitively coupled plasmas (CCP's): are maintained between two electrodes, that are usually in direct contact with the plasma and are operated with a radio frequency (rf) excitation
- inductively coupled plasmas (ICP's): are formed by an alternating current running through coils generating alternating magnetic fields that heat the plasma. The excitation frequency can be in the MHz (rf) to GHz (microwave (mw)) range.

DC glow discharge represents a simple and inexpensive way to generate atomic H. First studies demonstrated the potential of H passivation as an application to improve the performance of mc-Si and poly-Si based solar cell devices [95]. Nevertheless, a simple DC glow discharge has the disadvantage of a strong voltage drop, that is localized around the cathode ("cathode fall"). This implies strong acceleration of the H ions of several hundred eV. While sputtering by H can be neglected, as the sputtering yield for H is very low [96], H bombardment with high ion energies of 100-500 eV can lead to surface damage [97]. At even higher energies amorphization of the surface was observed [97, 98].

The cathode fall can be mostly avoided in discharges with alternating currents. Several groups [21, 69, 71, 99, 78, 73, 83, 100, 101] have used rf driven plasma sources in a ICP or CCP remote setup. In these remote setups, the heated samples are separated from the plasma. Such a "downstream" source can prevent ion bombardment of the surface and in some cases baffles were used for optical isolation of the plasma. Hence ions and UV irradiation cannot reach the substrate and damage the surface.

2.2.3 Solid Source (Firing)

Firing of hydrogenated Si nitride (SiN:H) is a well established method and industrially applied to passivate multi-crystalline Si wafers [23]. Hydrogen containing SiN films are deposited onto the surface of mc-Si wafers by PE-CVD. The layer serves simultaneously as a source of H for bulk passivation [102], an anti-reflective coating and provides emitter surface passivation [103]. The hydrogen is driven into the material during the contact firing, which usually takes place at temperatures around 750°C [23]. High temperatures are needed for the H to diffuse entirely through the wafer (thickness: ~100 µm). However, thermal processing at such high temperatures simultaneously also leads to a dissociation of defect-H complexes and reactivation of deep level defects, associated with transition metals or grain boundary defects [74]. During the thermal process, H release, diffusion, binding and retention of H need to be balanced at the same time. For an anneal at 750°C, it was shown recently that a drive in time of one second, followed by a rapid thermal quench, allows for higher lifetimes and efficiencies of EFG and String Ribbon based Si solar cells compared to durations of 10 s and longer [104].

2.3 Hydrogen Passivation of Poly-Si Thin Film Solar Cells: State-of-the-Art

Early investigations in 1979 by Seager et al. on hydrogen plasma treatments of grain boundaries in mc-Si demonstrated a significant reduction of potential barrier and density of states due to the H plasma treatment [21]. Passivation was achieved using a remote ICP source at a H_2 pressure of 0.13 mbar at 400°C for several hours. In the following work the authors could report on the improvement of the dark-current IV characteristic of a poly-Si solar cell structure by H plasma treatment [22]. H treatment was performed at 350°C for 16 hours. Nowadays firing of hydrogenated Si nitride (SiN:H) at high temperatures is the method of choice for industrial bulk passivation of mc-Si solar cells [23]. Recently it was found that an annealing time of one second at ~750°C is sufficient for high solar cell efficiencies, resulting in 18.2 and 17.8% for edge-defined film-fed grown and string ribbon multicrystalline silicon solar cells, respectively [104]. A duration of 10 s led to smaller improvements [104]. The effect of hydrogenation in multicrystalline Si seems to be more significant for low-quality, high-defective multicrystalline material like ribbon grown Si [105].

The firing of SiN:H was also applied to poly-Si films. For hydrogenation, the atomic density of the SiN layer is considered to be important for the efficiency of the hydrogenation process [106, 107]. However, the refractive index of SiN layers usually needs to be tuned between 2.0 and 2.2 to serve as an anti-reflective coating. As a consequence the SiN layer is able to provide only a limited amount of hydrogen atoms. Poly-Si exhibits a higher defect density than mc-Si. Therefore in the past it was assumed that the passivation effect would not be sufficient for poly-Si, due to the limited amount of hydrogen. The passivation of poly-Si layers through a firing at moderate temperatures of 600°C of SiN:H only led to limited success [108, 109].

Hydrogenation of poly-Si layers for solar cell application using SiN:H firing at higher temperatures of 750°C was researched by Carnel, et al. [24, 25, 110]. For large-grained (grain size: 5 µm) poly-Si absorbers the open-circuit voltage could be improved from 325 to 421 mV by firing of SiN:H while the efficiency was enhanced from 2.4 to 3.8% [25]. A comparable effect of hydrogen passivation was seen for small-grained (grain size: 0.2 µm) poly-Si. Here the open-circuit voltage enhanced from 229 mV to 355 mV and the efficiency from 1% to 1.6% [25].

Carnel, et al. also investigated the influence of a H plasma treatment [9, 111, 112, 110] and compared it to SiN:H firing [24, 25, 110]. Plasma treatment was carried out in a conventional CCP rf CVD system at a H_2 pressure of 1.3 mbar and a power of 60 mW/cm^2. The open-circuit voltage of fine-grained poly-Si absorbers with improved hetero-emitter was enhanced by the plasma treatment from 341 mV (0.8% efficiency) to 460 mV (2.3%) [111]. The passivation was carried out at 400°C for 30 min. In comparison to SiN:H firing (410 mV) plasma hydrogenation showed better results (i.e. 460 mV) [25]. Consistently the amount of H in the layer after plasma treatment was up to 10 times larger than after firing [24, 25]. Investigations of the temperature during the plasma treatment indicated an optimum in V_{OC} at 420°C [9], although later results showed no strong influence in the range of 265 - 440°C for fine-grained poly-Si cells [25]. The plasma was kept ignited while cooling down slowly for 30 min to 200°C. Therefore the long cooling down phase should be kept in mind. The influence of pressure showed a much stronger dependence with an optimum in V_{OC} at around 2 mbar [9]. Especially towards smaller pressures (0.5 mbar) V_{OC} fell of sharply. Note that the poly-Si films, investigated by Carnel were deposited at high temperatures of ~1100°C. Therefore these films usually exhibit larger open-circuit voltages and the results cannot be compared directly to solid-phase crystallized cells.

Higher temperatures during H plasma treatments have been applied by CSG-Solar AG which is to date the first and only company that went into mass production of poly-Si thin film solar cells [7]. For hydrogenation an ICP remote system was used. It was observed that poly-Si films were most effectively hydrogenated (in terms of cell performance) if hydrogenated at rather high temperatures of ~610°C resulting in an improvement of V_{OC} from 233 mV to 497 mV [8].

A defect passivation treatment at high plateau temperatures of up to 650°C was also applied by the poly-Si group at the University of New South Wales (UNSW) [26, 27, 28]. Using a low-pressure chemical vapor deposition (LPCVD) system with an inductively coupled remote plasma source, Kunz et al. achieved open-circuit voltages of 435 mV and efficiencies above 5% [28]. Earlier investigations by Straub et al. indicated benefits by going from 350°C to higher temperatures of 480°C [113]. A remote microwave plasma source has been used by Andrae et al. with H_2 diluted in Ar at a temperature of 600°C [29].

Temperature dependence was investigated by Fosca et al. in an electron cyclotron resonance (ECR) plasma system in the temperature range of 200 -

550°C [30]. The authors found an optimum temperature of 450°C with respect to V_{OC} of poly-Si solar cells.

Summing up it can be stated that hydrogenation has been recognized as an important treatment to passivate defects in poly-Si and to improve the device performance. Hydrogen passivation via H plasma treatment seems to be the preferred method leading to good results [109, 25]. However, no common opinion has been established yet on how the best H plasma treatment can be achieved. In particular results about the optimum substrate temperature during hydrogen plasma treatments diverge and there is a broad range of applied and optimum temperatures. In addition the passivation experiments have been carried out on a highly diverse and unequal set of poly-Si thin film solar cells. This sets the motivation for the investigations that will be presented here. Important process parameters (e.g. temperature, duration) and plasma parameters (e.g. pressure, geometrical setup, power) will be investigated thoroughly and a better understanding will be established.

3 Experimental Procedures

The following chapter describes structure and preparation of poly-Si samples and the characterization methods that have been used for the hydrogen passivation experiments of this work.

3.1 Sample Preparation

In the course of this work two different types of poly-Si samples were used. State-of-the-art solar cells based on SPC of PE-CVD grown a-Si were used as reference samples because of their high quality. These samples were extracted from the industrial production cycle of CSG Solar AG, Thalheim, Germany [7]. The other set of samples was obtained by using electron-beam evaporation (EBE) instead of CVD for absorber deposition.

3.1.1 Polycrystalline Si Solar Cells formed by SPC of PE-CVD grown a-Si:H

State-of-the-art poly-Si thin films were provided by CSG Solar AG [7]. The sample structure is illustrated in Fig. 3.1 . The following steps were performed by CSG: (1) Glass substrates (Schott Borofloat®33, 1.1×1.25 m^2, thickness 3.3 mm) were (2) surface-textured by CSG by dip-coating the samples with a solution of silica beats (0.5 µm diameter) . The samples were loaded into an Oerlikon Kai-1200 system [7] and subsequently coated with the following layers: (3) SiN:H layer, that serves simultaneously as diffusion barrier for contaminants of the glass and an antireflection coating (ARC); (4) about 50 nm of highly (n^+)-type phosphorous doped a-Si:H layer that represents the emitter of the solar cell; (5) around 1.3 µm thick (p)-type boron doped a-Si:H absorber layer and (6) about 50 nm of highly (p^+)-type boron doped a-Si:H layer that forms a back surface field at the rear side of the solar cell structure. All films were deposited within the same run by plasma-enhanced CVD (PE-CVD) with a total thickness of about 1.4 µm Si. It should be noted that the a-Si:H films

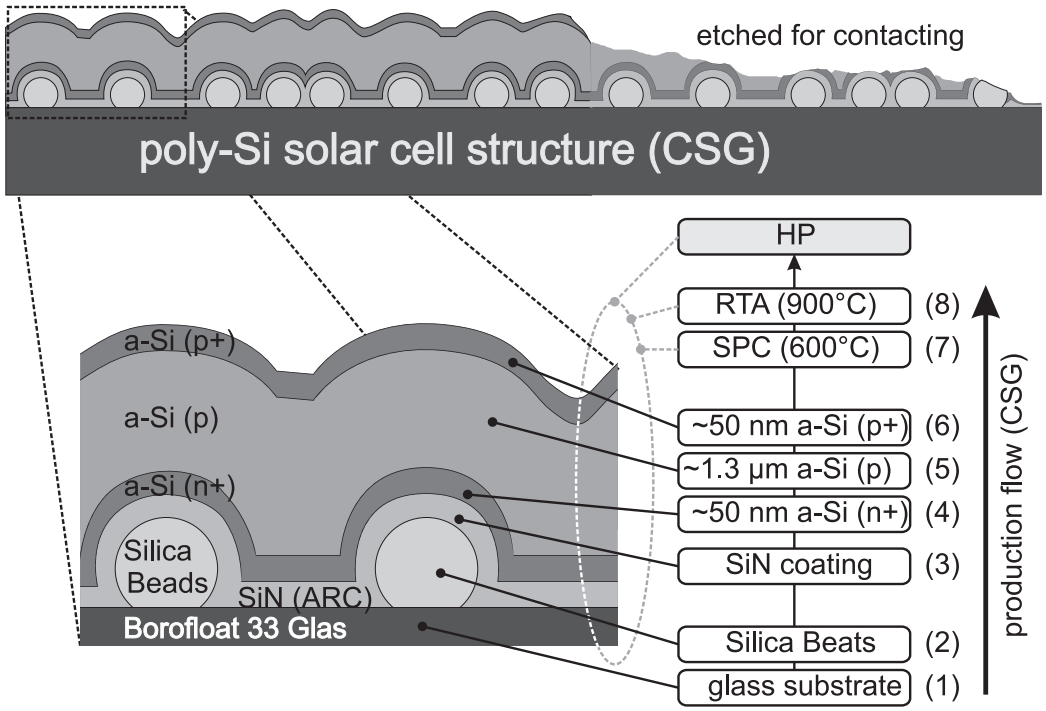

Figure 3.1: Structure and the production flow of a poly-Si solar cell, manufactured at CSG. The upper part shows an illustration of the cross section through the sample, where part of it is etched down afterwards to contact the (n^+) layer. The lower part shows the production flow and an enlargement of the structure. SPC and partially RTA were carried out at CSG. HP will be investigated in this work.

will still contain some amount of hydrogen prior to annealing, due to the deposition by CVD. The complete stack of initially amorphous Si films was annealed at around 600°C for several hours until the films were fully crystallized (7). This step is called solid phase crystallization (SPC). After SPC a rapid thermal annealing (RTA) step was performed (8), by heating up the samples briefly to over 900°C [6]. For this work two sets of samples were used, one with RTA and one without. Therefore samples were taken out of the solar module production line after the SPC step (7) and after the RTA treatment (8). The large samples (1.1×1.25 m^2) were broken into identical parts. Due to breaking the size of the small samples did vary slightly and was around 50×30 mm^2. Both types of samples (RTA and non-RTA treated) were then used for hydrogen plasma investigations. The aim was to study the influence of different H passivation treatments on the solar cell device and the interplay of HP with an additional RTA treatment.

In order to characterize the samples by photovoltage measurements, one corner of the samples was etched down to contact the Si(n^+) layer. For this a poly-Si etch solution was applied for 3 min at RT consisting of HNO_3 (65%),

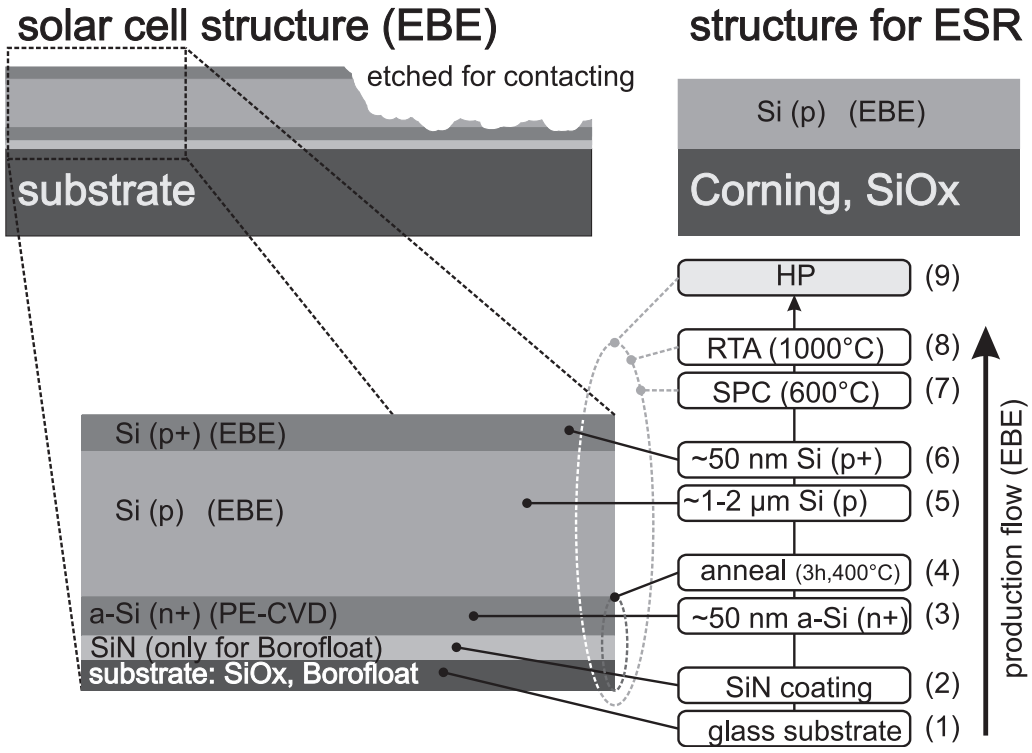

Figure 3.2: Structure and the production flow of a poly-Si solar cell and structure of a sample used for ESR measurements. The upper part shows an illustration of the cross section through the cell, where part of it is etched down afterwards to contact the (n^+) layer. For ESR only the absorber is deposited directly onto the substrate. The lower part shows the production flow and an enlargement of the cell structure.

H_3PO_4 (85%), HF (50%) and H_2O (30:10:1:15).

3.1.2 Polycrystalline Si Solar Cells formed by SPC of E-Beam Evaporated a-Si

Electron beam evaporation was tested in a new solar cell concept for the deposition of the absorber layer, because it offers many advantages in comparison to CVD (like higher deposition rates, lower system costs and the lack of toxic gases). Fig. 3.2 shows the structure of the samples.

Similar to the PE-CVD based approach described in Section (3.1.1) SiN:H coated Borofloat glasses (Schott Borofloat®33, 25×25 mm^2, thickness 3.3 mm) from CSG were used as foreign substrates (1) for the solar cell structures (shown in Fig. 3.2 on the left hand side). In this case no texturing with Silica beats was done but the sample was coated with SiN:H, acting as a diffusion barrier and ARC by CSG Solar AG (2). As alternative substrates, Si wafers with a 150 nm thick thermal oxide were used (1). The Si wafers serve as

an ideal model substrate where any potential contamination effects can be disregarded. The thermal oxide exhibits an amorphous structure and prevents epitaxial growth during the following processes.

Next an (n^+) phosphorus doped 30 nm thick a-Si:H emitter was grown in a conventional parallel plate 13.53 MHz PE-CVD reactor at HZB (3). For deposition the following conditions were used: substrate temperature 210 °C, base pressure 1×10^{-6} mbar, SiH_4 at 10 SCCM (standard cubic centimeters per minute) and 1% PH_3 diluted in H_2 at 1 SCCM. This layer was then annealed for 3h at 400°C to lower the hydrogen concentration. High concentrations of H would otherwise lead to problems during the subsequent thermal treatments.

After this step, between 1 and 2 µm thick low p-type ($\sim 1 \times 10^{16}$ cm^{-3}) doped Si was deposited by EBE [14] (4) followed by 50 nm thick highly (p^+) ($\sim 1 \times 10^{19}$ cm^{-3}) doped Si (5). Deposition was performed at a base pressure of $\sim 1 \times 10^{-7}$ mbar and a rate of ~ 300 nm/min. Doping was achieved by co-evaporation of boron using a boron effusion cell. Steps (4) and (5) were done without vacuum break. The influence of the substrate deposition temperature T_{dep} was investigated in the temperature range of 100 to 700°C. A subsequent thermal anneal was carried out at 600°C for 12 hours in a tube furnace in N_2 ambient, to solid phase crystallize the remaining a-Si (SPC) (6) [114]. Prior to HP the solar cell structures received an RTA treatment (7) [115]. Details about RTA and HP are given in Sec. 3.1.3 and 3.1.4, respectively.

To investigate the dangling bond concentration by electron spin resonance (ESR), a second set of samples was prepared (shown in Fig. 3.2 on the upper right hand side). In this case only bare Si absorber layers have been deposited by EBE (with the same parameters as taken for step (5)) directly onto thermally oxidized Si wafers (1000°C, 160 nm thick oxide) or Corning 1737 glass substrates. RTA was not carried out for the uncoated samples, to prevent indiffusion of contaminants originating from the glass.

Sample size was limited by the substrate holder of EBE to 25×25 mm^2.The samples could be either contacted directly because of the deposition of the absorber via a shadow mask (20×20 mm^2) or the absorber was etched the same way as described in Section (3.1.1) by a poly-Si corner etch.

3.1.3 Rapid Thermal Annealing

Rapid Thermal Annealing (RTA) was carried out under nitrogen atmosphere in a Heatpulse 210T system from AG Associates. The setup consisted of a quartz chamber, two banks of tungsten-halogen lamps and a microcontroller

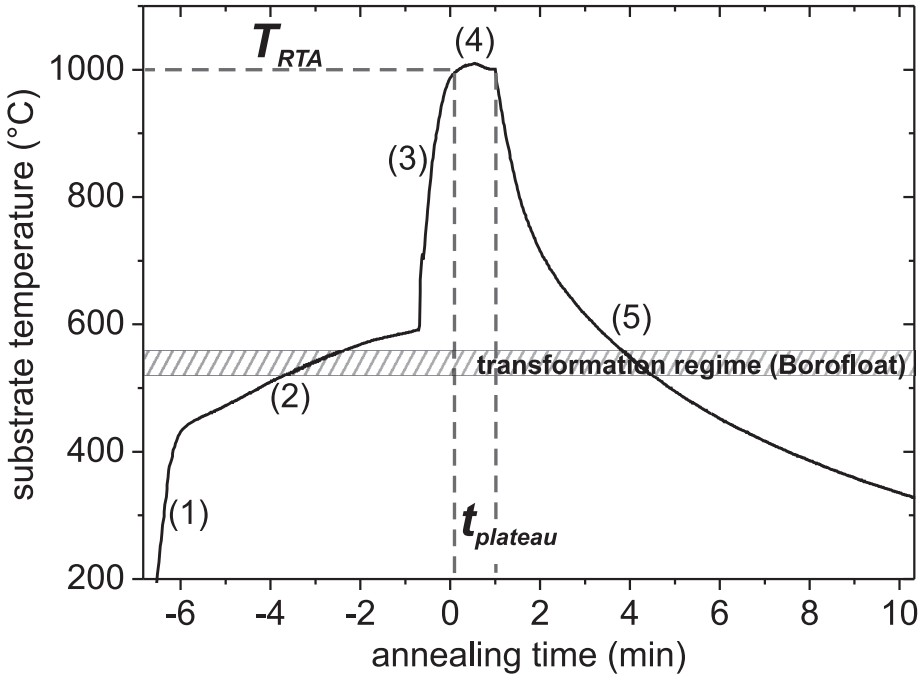

Figure 3.3: Substrate temperature during RTA. The samples were annealed at $T_{RTA} = 1000\,°\mathrm{C}$ for $t_{plateau} = 60\,\mathrm{sec}$.

unit [115]. A graphite wafer was used as a carrier. No specific cleaning procedure was applied to the samples. Beside the annealing temperature and duration, it is necessary to adapt the annealing profile to the properties of the glass. Therefore, adapted heating and cooling rates have been used for different temperature regimes. The crucial temperature regime for an RTA treatment of a glass-based sample is around the transformation temperature T_g (for Borofloat®33: $T_g = 525$ °C). The corresponding transformation regime of Borofloat® 33 is between 518°C (strain point) and 560°C (annealing point) [116]. Below the strain point the thermal expansion coefficient closely matches that of Si. Above the annealing point the glass softens slightly. Although the expansion mismatch becomes larger, stress between glass and Si is reduced. Between strain and annealing point, the expansion coefficient of the glass changes nonlinearly and slow heating and cooling rates are required to relax the glass and avoid cracking of the Si film. We applied a heating rate of about 0.7K/s and a cooling rate of about −1K/s for the transformation regime. Fig. 3.3 shows schematically the RTA profile applied in this work. The annealing started in the pre-heated chamber (around 100°C) directly after sample loading at a high rate (1), followed by a slow rate through the transformation regime (2) to about 620°C. A fast ramp (14K/s) (3) was ap-

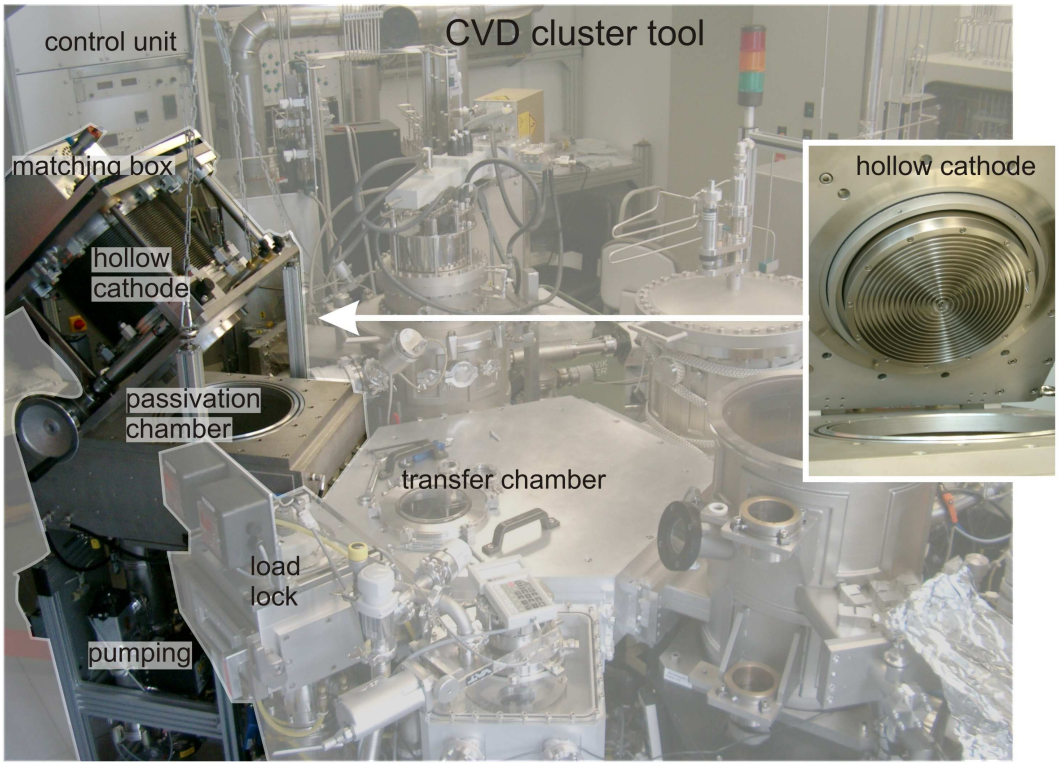

Figure 3.4: Opened passivation chamber, attached to the CVD cluster tool and magnification of the hollow cathode in the lid.

plied subsequently and the samples reached the final annealing temperature of $T_{RTA} = 1000°C$ with a plateau time of $t_{plateau} = 60$ s (4). The samples were cooled down afterwards again with a reduced rate through the transformation regime (5). The annealing chamber was opened between 200°C to 300°C and the samples were removed from the RTP system at about 100°C (not shown here).

3.1.4 Hydrogenation

A hydrogen plasma passivation tool (developed by FAP Dresden, Germany and HZB) was used to expose the samples to atomic hydrogen. The passivation chamber is attached to a CVD cluster tool. A photograph of the tool is seen in Fig. 3.4 . The inset shows a magnification of the hollow cathode in the open lid. A corresponding sketch of the vacuum system is depicted in Fig. 3.5 .

For a hydrogen treatment, samples were placed onto an 8 inch Si carrier and loaded into the load lock directly after the native oxide was removed and the samples have been dried by blowing with dry nitrogen. Native oxide on the sample surface was removed by 2% hydrofluoric acid (HF) for 3 min. At

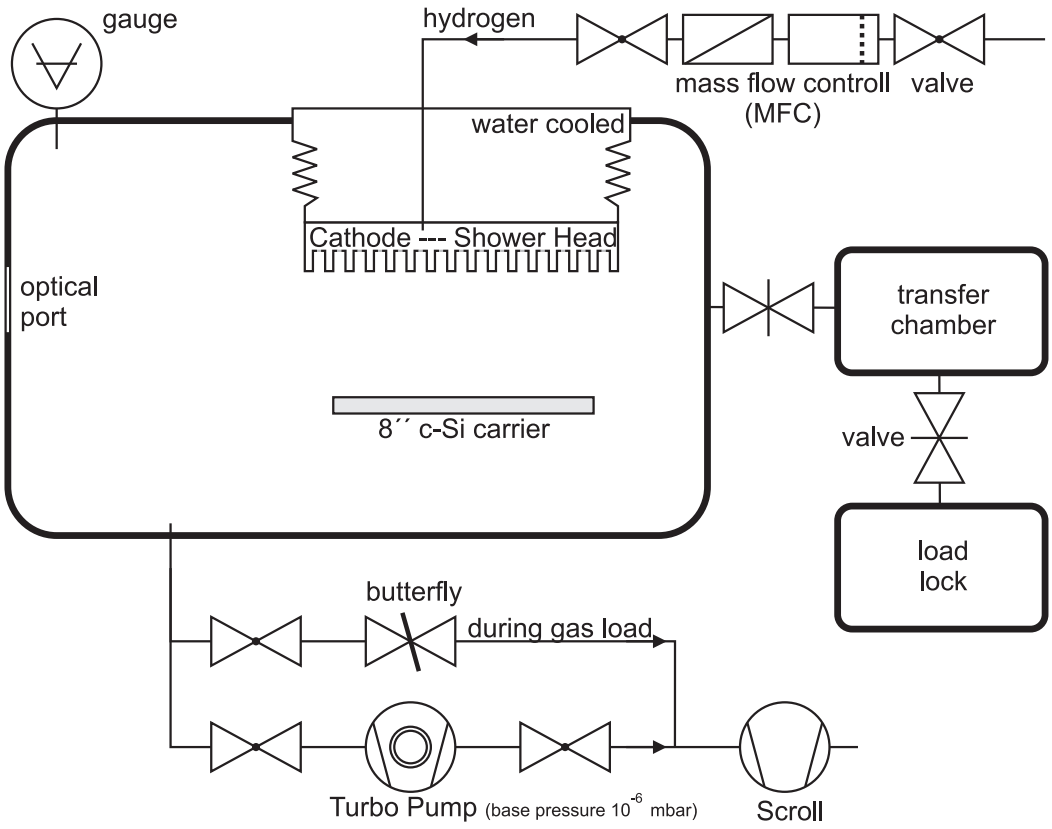

Figure 3.5: Sketch of the passivation chamber, attached to the CVD cluster tool. For details see text.

a pressure of $< 1 \times 10^{-5}$ mbar, samples were transferred into the transfer chamber and at a pressure of $< 2 \times 10^{-7}$ mbar into the passivation chamber. Base pressure (i.e. without gas load) of the passivation chamber was $\leq 1 \times 10^{-6}$ mbar. Vacuum was established via a fore-vacuum scroll pump (BOC-Edwards XDS35i) and a turbo pump (TPH450H).

After the samples had been transferred, the H process pressure p was established. Therefore H flux was controlled by mass flow control (MFC, Celerity Multiflow™ 7300). The cathode serves as a shower head for the process hydrogen gas and H_2 partial pressure p was varied between 0.1 and 10.0 mbar. At pressures of 1.0 mbar and above, pumping was done by the scroll pump and pressure was controlled at a constant H flux of 100 sccm by a butterfly valve. Below 1.0 mbar, pumping capacity of the scroll was limited and the chamber was therefore pumped via the turbo pump and pressure was controlled by H flux.

After the pressure stabilized, the samples were heated. A sketch of the passivation system, including heating system, plasma generation, electrodes, and magnification of the hollow cathode (right hand side) is illustrated in

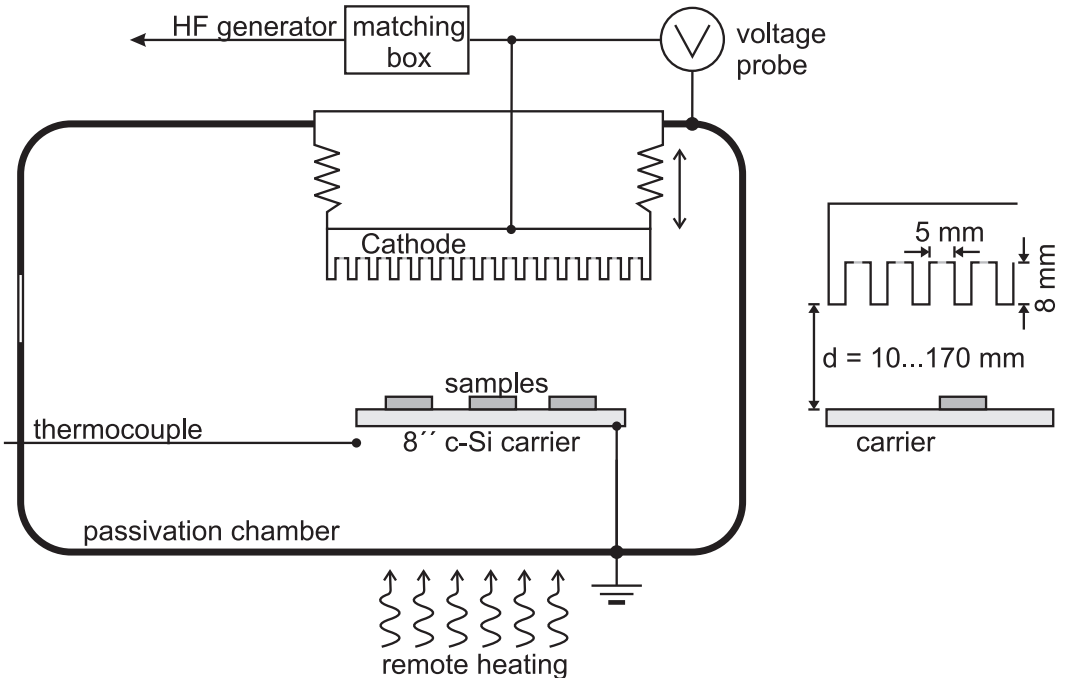

Figure 3.6: Sketch of the passivation chamber, including plasma generation, electrodes, heating system and magnification of the hollow cathode (right hand side). For details see text.

Fig. 3.6 . The heating system features a remote lamp radiation heater that allows controlled rapid heating and cooling phases with rates up to 200 K/min and substrate temperatures of up to 650°C. Temperature was controlled by a thermocouple and was calibrated beforehand. The corresponding temperature ramp is shown in Fig. 3.7. Heating rate was adapted to the Borofloat glass by heating up the samples slowly when passing the transformation regime between 518°C (strain point) and 560°C (annealing point) (step 2).

The plasma was ignited when the samples had reached the desired plateau temperature T_{HP} (here: 600°C, step 3). Therefore a hollow cathode, made out of stainless steel, was used in a diode configuration. The grooves are 5 mm wide, 8 mm deep (right hand side in Fig. 3.6) and are arranged helically over the whole cathode. The Si carrier was grounded and acted as a counter-electrode, while the surface of the samples remained on floating potential due to isolating substrates. The separation d between the carrier and the cathode (electrode gap) could be varied in the range of 10-170 mm. Plasma power was generated with a Cesar 136 (13.56 MHz, 600W) from Dressler Hochfrequenztechnik GmbH, Germany. Impedance matching was done with the matching box VM 1500 (Dressler).

After a plateau time $t_{plateau}$ (here: 10 min) the samples were cooled down

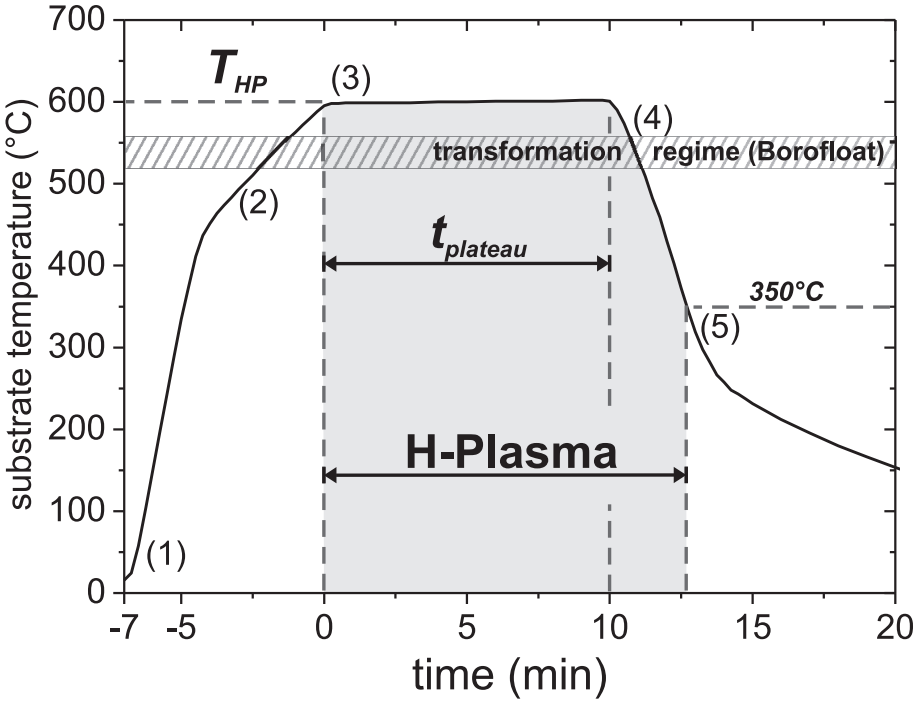

Figure 3.7: Substrate temperature during the hydrogen passivation at T_{HP} = 600°C. The plasma is ignited when the plateau temperature is reached (3). After the time $t_{plateau}$ the samples are cooled down (4) and the plasma is switched off, when the temperature of 350°C is reached (5).

rapidly while keeping the plasma ignited to prevent any out-diffusion of the hydrogen (step 4 in Fig. 3.7). The plasma was switched off at 350°C (5). The end-temperature of 350°C was chosen intentionally to counterbalance two effects: i) H out-diffusion, which requires low end-temperatures and ii) the etching of the Si surface by atomic H, which starts to become relevant at temperatures below 350°C [117]. After switching of the plasma, H flux was interrupted, the chamber was pumped to a pressure of 1×10^{-5} mbar and samples were transferred into the main chamber at a temperature of around 200°C (not shown here).

If not stated otherwise in the text, the following parameters were taken as a standard for the hydrogen plasma treatment. The temperature profile was chosen, as shown in Fig. 3.7 with a plateau temperature of $T_{HP} = 600$°C and a plateau time of $t_{plateau} = 10$ min. Plasma was ignited at a hydrogen pressure p of 1.0 mbar and an electrode gap d of 20 mm and run stable with a power density of 0.1 W/cm^2.

3.2 Plasma Characterization

The hydrogen plasma was characterized by measuring the breakdown voltage V_{brk} and also power P_{brk} necessary to ignite the plasma. Results, presented in Chapter 4, reveal that both quantities can provide helpful orientation, in order to optimize plasma geometry and hydrogen pressure. The plasma power of the generator was increased slowly in steps of 1 W each 5 s until ignition of the plasma took place. The applied voltage V_{pk} was measured peak to peak with an oscilloscope and a 1:10 attenuation voltage probe, attached after the matching box directly to the cathode (see voltage probe in Fig. 3.6). The current was not measured. The breakdown voltage V_{brk} and power P_{brk} needed to ignite the plasma were recorded in dependence of electrode gap d (Fig. 3.6) and H pressure p.

3.3 Sample Characterization

The material properties of poly-Si films and the electrical properties of poly-Si solar cell structures have been characterized by the following methods.

3.3.1 Raman - Phonon Scattering

Raman is a fast and nondestructive tool to characterize stress, defects and crystallinity of poly-Si films. The Raman spectra of poly-Si exhibits a line at 520 cm^{-1}, characteristic for the LO-TO phonon mode of c-Si. Its peak position and FWHM are affected by stress, defects and grain size. Tensile and compressive stress affect the LO-TO peak position of the c-Si spectrum. A redshift (negative $\triangle\omega$, shift to lower wavenumbers) of the Raman frequency indicates tensile strain, while a blueshift indicates compressive strain [118]. Small crystallites and high defect densities in poly-Si films can cause asymmetry and broadening of the Raman spectrum due to phonon scattering from the microcrystalline boundaries and intragrain defects [119, 120]. Defect scattering destroys the lattice translational symmetry and relaxes the momentum conservation rule during phonon-photon interaction [120]. Smaller crystallites lead to a downshift towards lower energy and a broadening, e.g. increase of the Raman FWHM.

For the measurements a micro-Raman spectrometer DILOR/ISA LabRAM 010 in backscattering configuration was used with an unpolarized HeNe laser for excitation (wavelength 632.82 nm, spectral resolution 1 cm^{-1}). The laser

beam intensity was chosen such that it did not induce any crystallization of the a-Si films during measurements.

3.3.2 Electron Spin Resonance

The Si dangling bond concentration of the Si films can be investigated by electron spin resonance (ESR) measurements [121]. Therefore a series of samples was prepared (as shown in Fig. 3.2 on the right hand side). In this case only bare Si absorber layers have been deposited by EBE (with the same parameters as used for step (5) in Sec. 3.1.4) directly onto Corning 1737 substrates. This was necessary because SiN contains a high amount of Si dangling bonds which happen to exhibit the same characteristic ESR spectra as dangling bonds in poly-Si. It is impossible to differentiate between dangling bonds from the Si film and the SiN. Therefore SiN coated glass substrates are not suited for ESR measurements. Standard room temperature electron spin resonance (ESR) was utilized for spin density measurements of the Si dangling bonds. For this purpose the samples were cut into an appropriate size (4×10 mm^2) and placed in a continuous-wave (cw) ER4104OR resonator of a Bruker ESP300 X-Band (9.5 GHz) spectrometer [122]. A magnetic-field modulation of 0.4 mT at a frequency of 100 kHz was used. The microwave power was set to 2 mW such that saturation effects did not occur. The spin density calibration was achieved by comparing the ESR response of the samples to a known spin standard.

3.3.3 Open Circuit Voltage and Suns-Voc

The open circuit voltage V_{OC} was measured steady-state in a conventional sun simulator under standard test conditions (STC) which are AM1.5 spectra with 100 mW/cm^2 and 25°C substrate temperature. The samples were contacted simply by needles without any sophisticated metallization scheme.

Furthermore quasi-steady state Suns-Voc measurements were performed. Suns-Voc as a measurement has been first introduced by Sinton and Cuevas in 2000 and is now an established method for solar cell characterization [123]. It involves the measurement of the open-circuit voltage V_{OC}^{suns} during a illumination with a short light flash $J_{flash}(t)$. The intensity of the light flash is measured simultaneously and given in units of one sun, i.e. $J_{flash}(t) = \text{suns}(t)$. The characteristic time constant of the decaying light flash is in the range of 4 ms and long in comparison to the lifetime of the minority charge carriers (order of ns). This way the sample is operated in a quasi-steady-state mode.

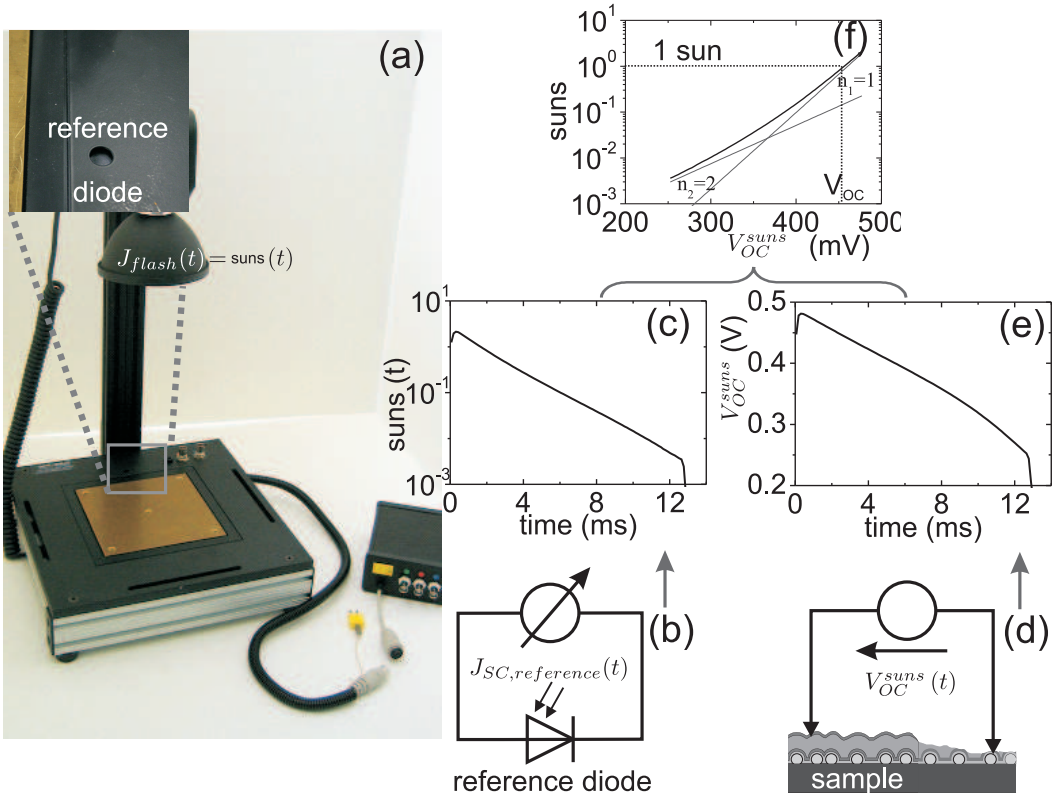

Figure 3.8: Principle of Suns-Voc measurements: a) Sinton setup, b) reference diode, c) flash illumination intensity $J_{flash}(t) = \text{suns}(t)$, d) poly-Si solar cell sample, e) $V_{OC}^{suns}(t)$ and f) Suns-Voc data $V_{OC}^{suns}(\text{suns})$.

The Sinton setup [123] is shown on the left hand side of Fig. 3.8 (a). It consists of a triggered Xenon flash light (Quantum® QFlash®), a temperature controlled chuck to place the samples and a reference diode (shown in the magnification). The right hand side illustrates the measurement principle. The intensity of the light flash is measured time-resolved via the short-circuit current $J_{SC,reference}(t) = J_{SC,reference}(t)|_{1\text{sun}} \times \text{suns}(t)$ of a known reference diode (b). The illumination level suns(t) is varied between suns$(t) = 3$ and $1/100$ (c).

Simultaneously the open-circuit voltage $V_{OC}^{suns}(t)$ of the sample (d) is measured time-resolved during the light flash (e). From both data of (c) and (e) the Suns-Voc curve is deduced (f).

Fitting of Suns-Voc Data: The IV characteristic of a poly-Si solar cell device can be modeled within the two-diode model. Under open circuit conditions (current density $J = 0$) the series resistance R_s of the solar cell can be omitted.

For Suns-Voc measurements, the IV characteristic therefore reduces to

$$J_{ph}^{suns} = J_{01}\left(\exp\left(\frac{V_{OC}^{suns}}{n_1 V_t}\right) - 1\right) + J_{02}\left(\exp\left(\frac{V_{OC}^{suns}}{n_2 V_t}\right) - 1\right) + \frac{V_{OC}^{suns}}{R_{sh}} \qquad (3.1)$$

where $n_1 = 1$, $n_2 = 2$ are the ideality factors, J_{01}, J_{02} are the corresponding saturation current densities and $V_t = \frac{k_b T}{q}$ is the thermal voltage. The first term with $n_1 = 1$ describes the recombination current of charge carriers in the bulk absorber, whereas the second term with $n_2 = 2$ models recombination in the SCR.

Suns-Voc measures the photovoltage V_{OC}^{suns} as a function of illumination. The illumination intensity is measured by a calibrated photodiode in units of one sun. Suns-Voc measurements therefore return the data set V_{OC}^{suns} (suns). To obtain the photocurrent J_{ph}^{suns}, it is assumed that J_{ph}^{suns} is linearly dependent on the illumination, i.e. $J_{ph}^{suns} = -J_{SC}^{suns} = -J_{SC}|_{1\,\mathrm{sun}} \times$ suns. This way the Suns-Voc data can be expressed by $V_{OC}^{suns}\left(J_{ph}^{suns}\right)$. This data set can be fitted by Eq. 3.1, where J_{01}, J_{02} and R_{sh} are the fitting parameters. From the quantities of J_{01} and J_{02} the dominating recombination mechanism can be observed. J_{01} describes the recombination current of charge carriers in the bulk absorber, whereas J_{02} models recombination in the space-charge region. If the short circuit current J_{SC} is unknown, only the normalized quantities J_{01}/J_{SC}, J_{02}/J_{SC} and R_{sh}/J_{SC} are obtained. V_{OC} can be extracted directly from the data and is equal to V_{OC}^{suns} at one sun. In the example, presented in Fig. 3.8, the contributions of $n_1 = 1$ and $n_2 = 2$ are shown in (f). In addition the measured Suns-Voc curve can also be recalculated into a corresponding one-sun pseudo-IV curve and a pseudo fillfactor can be extracted.

Pseudo-IV Curve: The Suns-Voc data can also be transformed into an equivalent pseudo-IV characteristic at one sun. The general IV characteristic without the series resistance R_s exhibits the form

$$J + J_{ph} = J_{01}\left(\exp\left(\frac{V}{n_1 V_t}\right) - 1\right) + J_{02}\left(\exp\left(\frac{V}{n_2 V_t}\right) - 1\right) + \frac{V}{R_{sh}} \qquad (3.2)$$

The Suns-Voc curve (Eq. 3.1) can be transformed into a pseudo-IV curve by defining an equivalent voltage V_{eq} and current density J_{eq} that corresponds to V and J of the light-IV curve at one sun (Eq. 3.2). The left- and right-hand side of Eq. 3.1 and Eq. 3.2 are equal under the constraint

$$V_{eq} = V_{OC}^{suns} \quad \text{and} \quad J_{ph}^{suns} = J_{eq} + J_{ph}|_{1\,\mathrm{sun}} \,. \qquad (3.3)$$

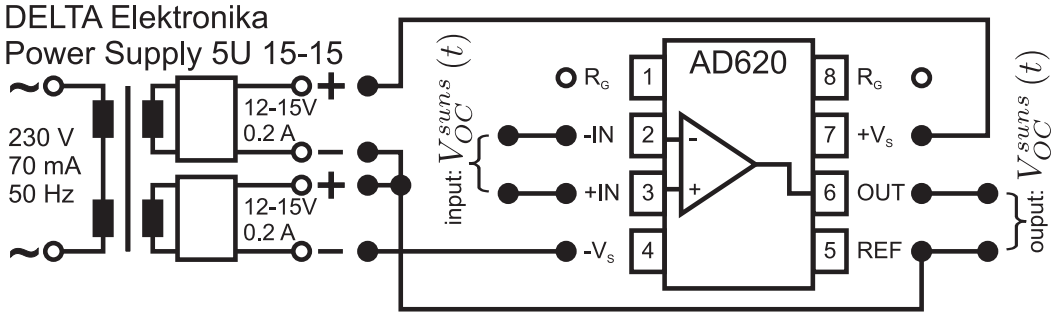

Figure 3.9: Connection circuit of the impedance amplifier, consisting of a symmetric power supply (on the left hand side, +15 V, 0 V, -15 V) and the AD620 amplifier with the gain factor set to one (right hand side).

The equivalent current density then is given by:

$$J_{eq} = J_{ph}^{suns} - J_{ph}|_{1\,\mathrm{sun}} = J_{SC}|_{1\,\mathrm{sun}} \times (1 - \mathrm{suns}) \tag{3.4}$$

The IV characteristics in the two-diode model are identical for the two measurement conditions (i.e. one sun light-IV and Suns-Voc) except for the contribution of the series resistance R_S. In the case of Suns-Voc, the pseudo-IV does not include the series resistance. This is also reflected in a slightly higher pseudo-fillfactor (pFF) compared to the fillfactor of a measured IV curve that includes the series resistance [124].

In every single experiment typically three poly-Si samples were treated simultaneously. Each of those samples has been characterized by Suns-Voc at 6 to 9 different positions, distributed uniformly over the surface of the sample. The characteristic quantities have been extracted directly from the data (V_{OC}, pFF) or by fitting (J_{01}/J_{SC}, J_{02}/J_{SC}). At the end for each quantity an average was formed of all 18 or 27 data points.

Buffer Amplifier: The samples have not been metallized and have been directly contacted by needles. This led to a high contact resistance. To increase the input impedance, a buffer amplifier was inserted between the input of the Sinton setup and the needles, probing the samples. The connection circuit of this buffer amplifier is illustrated in Fig. 3.9 . For this purpose a symmetric power supply (+15 V, 0 V, -15 V) was used together with the amplifier AD620 that offers a high input impedance of 10 GΩ and 2 pF and whose gain factor was set to one (by setting $R_G = \infty$). This way it was possible to measure metallized, as well as non-metallized solar cells.

4 Plasma Process Optimization

First goal of the thesis was to find optimized process parameters for the hydrogen plasma treatment. For this purpose an empirical optimization procedure was performed to realize an efficient defect passivation. Plasma parameters like hydrogen pressure, electrode gap and plasma power could have a significant impact on hydrogen density, ion bombardment and hence on the passivation of poly-Si thin film solar cells. The quality of the passivation process was characterized by open-circuit voltage measurements of the reference samples, as described in Sec. 3.1.1. The detailed discussion regarding defect passivation, material quality and solar cell performance in Chapter 7 validates this approach. In addition the plasma process was characterized by probing the breakdown voltage, needed to ignite the plasma. In parallel plasma modeling was performed in cooperation with E. Amanatides from the group of Prof. Mataras from the Dept. of Chemical Engineering, University of Patras, to discuss and explain the observed results on the basis of plasma conditions.

4.1 Influence of H Plasma Treatment on Device Performance

The aim of H passivation is to enhance the device performance of the poly-Si thin film solar cell. The H treatment mainly improves the open-circuit voltage V_{OC}. Due to better collection efficiency, also the current of the cell is normally enhanced. Therefore an analysis of the current-voltage (IV) characteristic of the cell is presented. Because of the high series resistance of the non-metallized samples, the current cannot be evaluated directly. However, by Suns-Voc measurements, the IV characteristic can be accessed indirectly (in this case normalized to the short-circuit current J_{SC}). According to Section 3.3.3, the Suns-Voc data can be transformed into an equivalent IV curve. This section shows the influence of the H plasma treatment on the IV characteristic, probed by Suns-Voc measurements, before presenting the optimization procedure in the next section.

For this purpose, reference samples from CSG Solar AG have been characterized before and after the hydrogen passivation. The hydrogen treatment was performed with the standard plasma conditions described in Sec 3.1.4 (600°C, 10 min, 1.0 mbar H_2). The Suns-Voc data is shown in Fig. 4.1 a). Without the treatment (dashed line) the samples exhibit a low V_{OC} (at one sun) of 223 mV. After the hydrogen plasma treatment (solid line) the Suns-Voc curve is strongly enhanced (i.e. shifted to the right). The V_{OC} is more than doubled by the hydrogen passivation and amounts to 461 mV.

The measured Suns-Voc curves can be fitted and the saturation current density ratios J_{01}/J_{SC}, J_{02}/J_{SC} for the ideality factors $n_1 = 1$ and $n_2 = 2$ can be extracted. The contributions are plotted in 4.1 a). After the hydrogen treatment the saturation current densities improved from $J_{01}/J_{SC} = 7.8 \cdot 10^{-5}$ and $J_{02}/J_{SC} = 8.3 \cdot 10^{-3}$ to $J_{01}/J_{SC} = 2.0 \cdot 10^{-8}$ and $J_{02}/J_{SC} = 2.3 \cdot 10^{-5}$, respectively.

High saturation current density ratios in the case before HP suggest high recombination rates in the bulk (J_{01}/J_{SC}) and via near-midgap defect states in the SCR (J_{02}/J_{SC}). The solar cell exhibits a low V_{OC} of 223 mV at one sun. At low illumination levels (<1/10 suns) it is dominated by an $n = 2$ behavior (recombination in the SCR).

The saturation current density ratios are strongly reduced by the hydrogen treatment. This can be explained by defect passivation leading to less recombination in the bulk and in the SCR. After HP J_{01}/J_{SC} and J_{02}/J_{SC} are lowered by a factor of around $4 \cdot 10^3$ and $4 \cdot 10^2$, respectively. The open circuit voltage at one sun is improved to 461 mV and at high illumination levels ($\geq$ 1 sun) the device is controlled by an $n = 1$ behavior.

Fig. 4.1 b) shows the equivalent pseudo-IV curves of the samples. The hydrogen treatment helps in lowering the saturation current density ratios, leading to higher V_{OC} values. Simultaneously also the fillfactor pFF of the solar cells is improved. This is due to lower saturation current density ratios (hence higher V_{OC}) and an ideality factor closer to one. In the presented case pFF is enhanced from 56 % to 77 %.

As the actual short-circuit current density J_{SC}, the equivalent current density J_{eq} in 4.1 b) is given in units of J_{SC}. It is expected that the HP also affects positively J_{SC}, as has been evidenced for different types of poly-Si samples [125].

To attribute the observed effect to the plasma treatment, secondary effects caused by thermal annealing or molecular hydrogen incorporation need to be

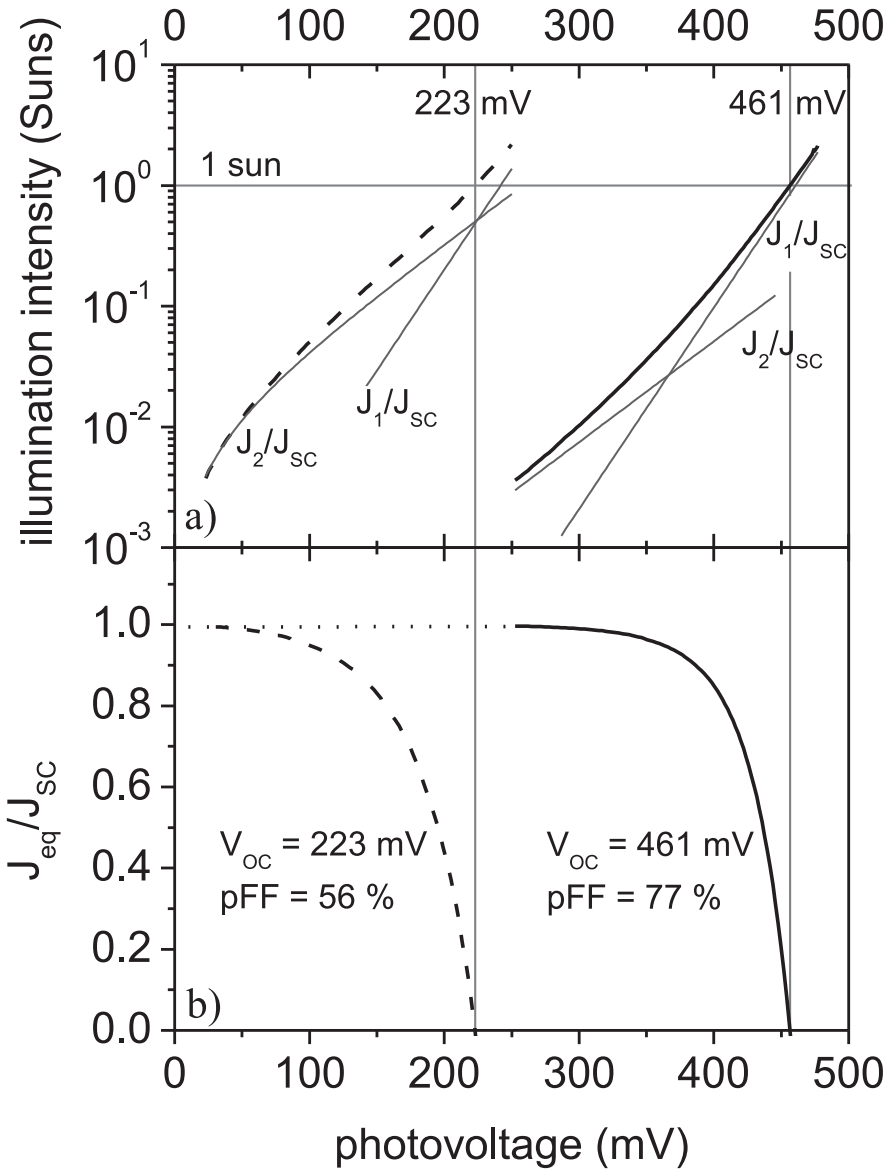

Figure 4.1: a) Photovoltage of poly-Si solar cells with (solid line) and without hydrogen passivation (dashed line) measured as a function of illumination intensity (given in units of one sun). b) Transformed pseudo-IV curve which contains the equivalent current density J_{eq} that corresponds to the current density J of the light-IV curve at one sun (normalized to J_{SC}).

excluded. To check this, the same hydrogen treatment was carried out under the exactly same conditions at 600°C and 1.0 mbar H_2 ambient atmosphere but without igniting the plasma. After this experiment the samples showed no improvement in Suns-Voc and V_{OC} was the same as prior to the experiment. Therefore the annealing at 600°C for 10 min has no noticeable influence and cannot account for the presented results. Clearly only the combination of annealing together with ignited hydrogen plasma causes incorporation of atomic H into the films and achieves an improvement of the IV characteristic.

It was observed that hydrogen passivation improves the complete IV characteristic. Yet in the following work, the quality of the passivation will be mainly characterized by V_{OC}. As will be discussed later in Chapter 7, V_{OC} can be directly linked to the effective diffusion length L_{eff} of the minority carriers. Defects, lowering the minority carrier lifetime and therefore the diffusion length, will directly lead to a deterioration of $V_{OC.}$. The open-circuit voltage therefore represents a very sensitive and valuable quantity to characterize the electronic quality of the absorber.

4.2 Influence of Plasma Conditions

In the following section plasma parameters like hydrogen pressure, electrode gap and plasma power will be investigated with regard to open-circuit improvements. In addition the ignition of the hydrogen plasma is studied for different electrode gaps d of 10 to 170 mm in the pressure range p of 0.1- 1.0 mbar. The aim is to find optimized plasma conditions for passivation and to get a better understanding of the plasma process.

Pressure and Electrode Gap The ignition of the plasma was characterized by plasma voltage measurements at the cathode as described in Sec. 3.2. For each parameter set $p \cdot d$, plasma power was increased steadily until the breakdown (ignition) of the gas. Both breakdown power P_{brk} and the corresponding voltage V_{brk} (peak to peak) needed to ignite the plasma were recorded. The passivation experiments on the other hand were conducted at a constant power of 50 W. The breakdown voltageV_{brk} (ignition conditions) and the cathode voltage V_{pk} (peak to peak) under passivation conditions are given in Table 4.1 for a H_2 plasma at 1 mbar and different electrode gaps. The cathode voltage V_{pk} is roughly constant. V_{brk} however exhibits a clear minimum at an electrode gap of 20 mm.

Table 4.1: Cathode voltage a) V_{brk} for plasma ignition and b) V_{pk} under passivation conditions (constant power, 50 W) for H_2 plasma at 1 mbar and different electrode gaps.

Pressure (mbar)	Gap (mm)	Voltage V_{brk} peak-peak (V)	Voltage V_{pk} peak-peak (V)
1	10	380	268
1	20	284	262
1	30	324	264
1	40	354	262
1	50	380	260
		a) plasma ignition	b) passivation condition

In Fig. 4.2 V_{brk} is plotted for different pressures p = 0.1, 0.2, 0.3, and 1.0 mbar over $p \cdot d$. For each pressure V_{brk} declines with reduced electrode gap d and exhibits a minimum followed by a strong increase. The breakdown of hydrogen plasma for direct-current (dc) discharges is usually governed by Paschen's law, which states that V_{brk} should be a function of the product $p \cdot d$ only [126]. In case of alternating-current rf discharges the relationship is more complicated. For each pressure in Fig. 4.2 the minimum occurs at different values of $p \cdot d$. In a recent publication it was proposed that the similarity law should be of the form $V_{brk} = \Psi\,(p \cdot d,\, d/R,\, f \cdot d)$, where R is the diameter of the cathode and f is the frequency of the rf electric field [127]. In the presented case deviations are also expected due to the hollow cathode. As observed the minimum is shifted for increasing pressures towards higher $p \cdot d$ values.

In the upper part of Fig. 4.3 the breakdown power P_{brk} is given for 0.3 mbar, plotted as a function of the product of pressure and distance. For comparison the breakdown voltage V_{brk} (same as in Fig. 4.2) is plotted again for 0.3 mbar. As can be seen, both of them exhibit very similar characteristics including a clear minimum.

Solar cell test samples (Sec. 3.1.1) were used to study the influence of different electrode gaps and different pressures on the defect passivation. For all passivation runs the same temperature profile with $T_{HP} = 600\,°C$ and $t_{plateau} =$ 10 min was used. The dissipated power was kept constant ($0.1\,W/cm^2 = 50\,W$). For a pressure of 0.3 mbar, experiments were in addition also performed at a plateau temperature of 400°C and 500 °C. Before HP the samples exhibited a V_{OC} of 223 ± 4 mV. The lower part of Fig. 4.3 depicts the V_{OC} after HP at 400 °C, 500 °C and 600 °C. The enhancement in V_{OC} after HP is significant for all cases. Higher plateau temperatures lead to improved V_{OC}. A strong improvement can be observed from 400 °C to 500 °C, however, only a minor

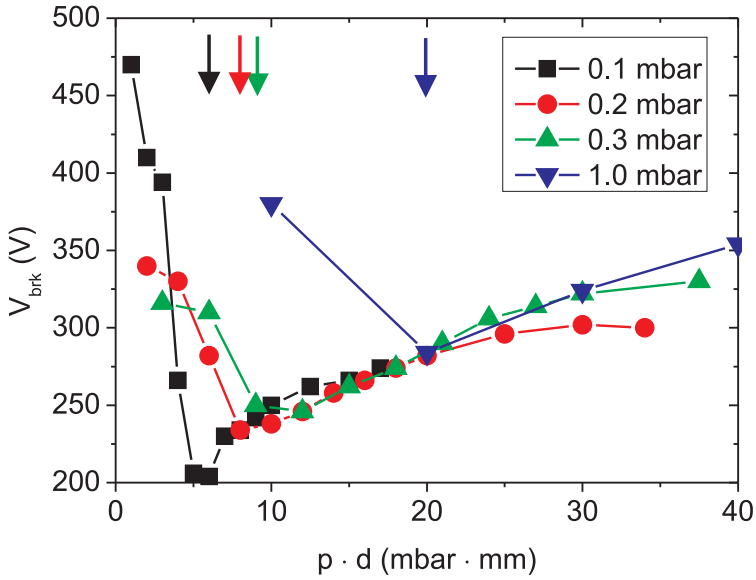

Figure 4.2: Breakdown voltage V_{brk} of the plasma versus the product of pressure p and electrode gap d for $p = 0.1$, 0.2, 0.3 and 1 mbar. The positions of the minima are indicated by arrows.

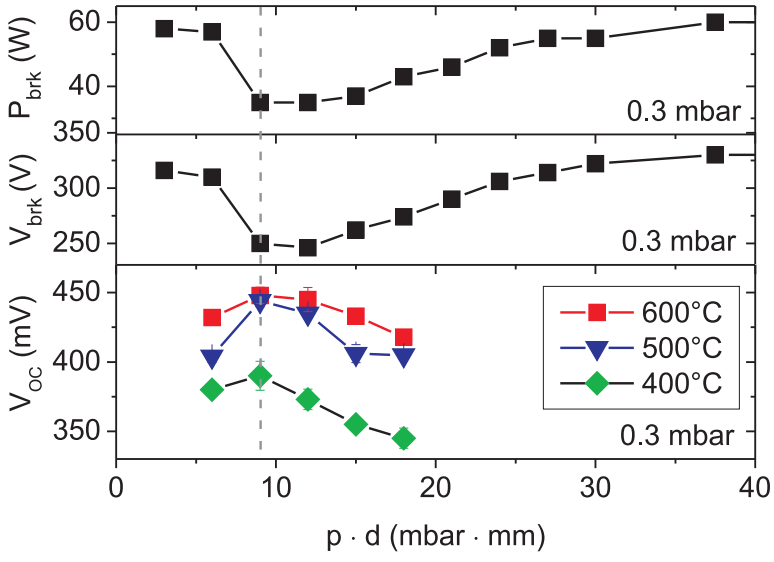

Figure 4.3: Breakdown power P_{brk} and breakdown voltage V_{brk} of the plasma at p = 0.3 mbar versus the product of pressure and electrode gap. The V_{OC} after hydrogen passivation at 400 °C, 500 °C and 600 °C (for 10 min) are given in the lower part. Highest values of V_{OC} are obtained where P_{brk} and V_{brk} are lowest.

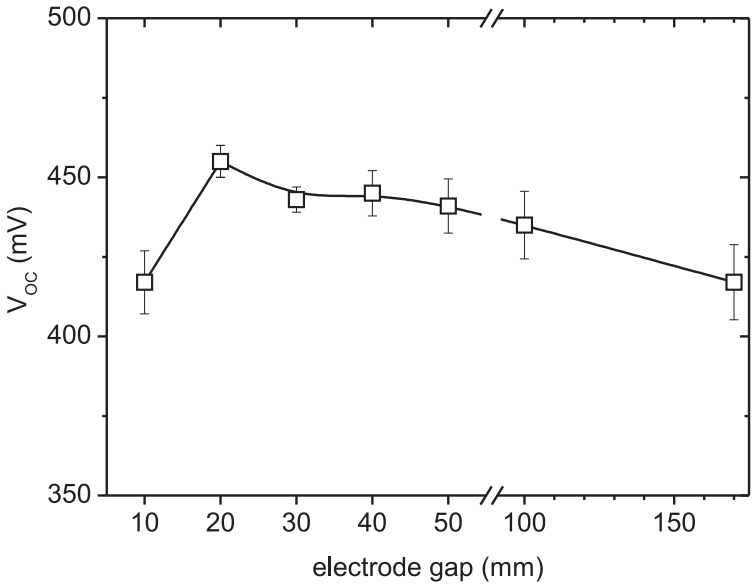

Figure 4.4: Open circuit voltage after HP at 1 mbar, plotted over electrode gap d. The maximum at $d = 20$ mm corresponds to the minimum in breakdown voltage for 1 mbar.

change was observed between 500 °C and 600 °C.

The curves for the investigated temperatures follow the same trend. In all cases the V_{OC} exhibits a maximum at the parameter set $p{\cdot}d = 0.3\,\text{mbar} \cdot 30\,\text{mm}$ that corresponds to the minimum of voltage and power required to ignite the plasma. Fig. 4.4 shows the V_{OC} after HP at 1 mbar, plotted over electrode gap d. The maximum at $d = 20$ mm again corresponds to the minimum in V_{brk}.

A similar behavior was also observed for the investigated H pressures of 0.1 and 0.2 mbar (not shown here). For each pressure the maximum V_{OC} value after HP at 600 °C (for 10 min) is depicted in Fig. 4.5 as a function of $p \cdot d$. The positions of the minima in V_{brk} (from Fig. 4.2) are indicated by arrows in Fig. 4.5, revealing that the maximum V_{OC} values are always obtained at those points where the breakdown voltage has its minimum. In the conducted experiments the minimum of the rf breakdown curves seen in Fig. 4.2 always led to the best V_{OC}. Also note that the V_{OC} values obtained for the different pressures at the corresponding optimum electrode gaps in Fig. 4.5 are equally high (450 mV).

Plasma Power The plasma power was investigated for the optimum passivation conditions with a fixed pressure of 1 mbar and an electrode gap of

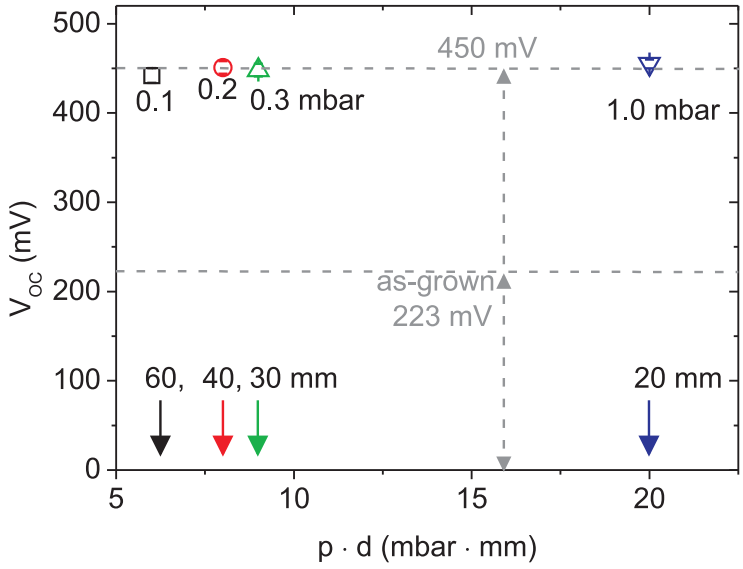

Figure 4.5: Maximum V_{OC} after hydrogen passivation at 600°C (for 10 min) versus $p \cdot d$, for different pressures p at the corresponding optimum electrode gap d. All values are in the same range of 450 mV independent of the pressure. Also given are the positions of the minima of the breakdown voltage V_{brk} in Figure 4.2.

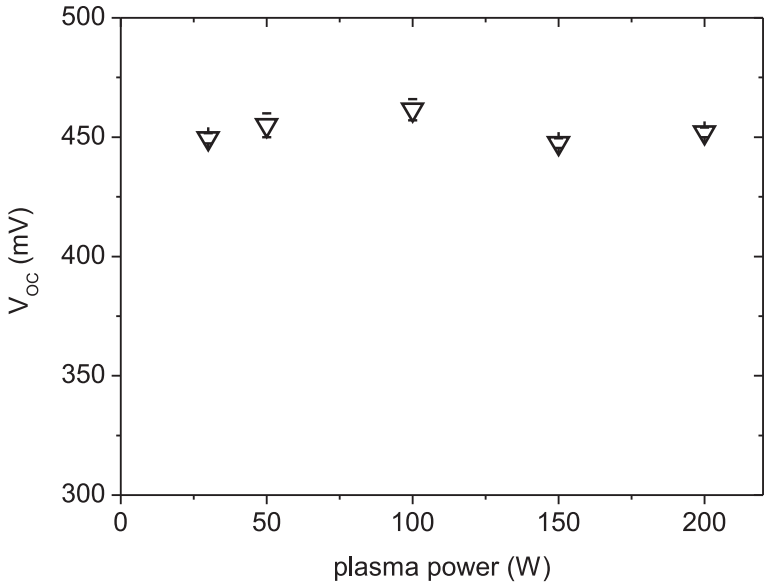

Figure 4.6: Open circuit voltage of poly-Si samples passivated at 1 mbar and 20 mm gap, plotted as a function of applied plasma power.

20 mm. The same temperature profile as before was used, with $T_{HP} = 600\,°C$ and $t_{plateau} = 10$ min. Only the dissipated power was not kept constant (before $0.1\,W/cm^2 = 50$ W). Fig. 4.6 shows the open circuit voltage of passivated poly-Si samples, plotted as a function of applied plasma power. Interestingly the results do not exhibit any clear and strong trend and higher applied powers

do not lead to an improved HP treatment. It is expected that higher plasma power leads to a higher atomic H concentration in the plasma. However, no enhancement in V_{OC} is observed.

4.3 Plasma Simulation

Plasma simulations were performed to get a deeper insight into the physics of the preceding results and to explain why an optimum is observed for electrode gaps, corresponding to minimum breakdown voltages. The simulations of the reactor were carried out in collaboration with E. Amanatides from the group of Prof. Mataras from the Dept. of Chemical Engineering, University of Patras. In the following a brief overview of the model together with the most relevant results will be given. A profound description of the plasma model can be found in Ref. [128, 129].

4.3.1 Plasma Model

The plasma reactor was modeled using the professional program CFD-ACE+™ V2004 from ESI Group that is based on self-consistent computational fluid dynamics (CFD). The simulation of our problem has been done by taking into account the flow, heat, chemistry, plasma (CCP) and electric modules of the specific software. Fluid dynamic models also known as hydrodynamic models are based on solving transport equations that are derived from the general Boltzmann transport equation. The limitations of this model imply the assumption of a Maxwellian electron energy distribution function (EEDF), which can differ from the actual EEDF especially in the high energy range [130]. Furthermore the drift-diffusion approximation limits the model to a certain pressure range and will not be reliable for low pressure regimes ($<$ 1 mbar). For this reason, the simulations were all conducted at a pressure of 1.0 mbar.

The modeling of a hydrogen discharge can be quite complex. This is attributed to the fact that H can occur in the plasma in both electropositive and electronegative states [131]. Some important reactions are summarized in table 4.2. It includes electron-molecule dissociation, dissociative excitations and ionizations together with ion-molecule reactions and ion-electron recombination. The production of negative H^- ions upon electron impact involves intermediate vibrational excited $H_{2,\nu}$ states (Eq. 4.8), while the positive ions produced in electron collisions are primarily H_2^+ (Eq. 4.1) and a minority

$$e^- + H_2 \rightarrow H_2^+ + 2e^- \quad (4.1)$$
$$e^- + H_2 \rightarrow 2H + e^- \quad (4.2)$$
$$e^- + H_2^+ \rightarrow 2H \quad (4.3)$$
$$H_2^+ + H_2 \rightarrow H_3^+ + H \quad (4.4)$$
$$e^- + H_2 \rightarrow e^- + H_{2,\nu} \quad (4.5)$$
$$H_2 + H_{2,\nu} \rightarrow H_2 + 2H \quad (4.6)$$
$$H + H_{2,\nu} \rightarrow 3H \quad (4.7)$$
$$e^- + H_{2,\nu} \rightarrow H + H^- \quad (4.8)$$
$$e^- + H_2 \rightarrow H_2 + e^- \text{ (mom. transfer)} \quad (4.9)$$

Table 4.2: Some chemical reactions implemented into the plasma model.

fraction of H^+. Also very common is the reaction of H_2^+ with H_2 molecules to produce H_3^+ ions and atomic H (Eq. 4.4). This process is very fast and exhibits a high cross section.

The simulations were carried out in a 2D geometry. The upper part of Fig. 4.7 shows a geometric sketch of a 2D cross section plane through the plasma setup used in the experiments. The gas inlets are embedded within the grooves of the hollow cathode. Faced opposite to the cathode is the grounded substrate carrier that acts as a counter electrode. Only the carrier was considered. Samples on isolating glass substrates were neglected. The electrode gap d is measured between the carrier and the nearest part of the hollow cathode not including the grooves (according to the experiment). The complex structure of the cathode and the H inlet requires a fine structured grid. Choosing the smallest possible unit cell reduces computing time. The smallest unit cell suited for the simulation is indicated by the dotted lines, representing the symmetry boundaries. In the lower part of Fig. 4.7 the unit cell is depicted once again, this time rotated by 90°.

The simulation returns a 2D data set (mapping) of the desired quantities. The results are obtained for a complete cycle (which corresponds to ~ 74 ns) that is discretized into 20 time steps. To characterize plasma bulk and surface properties, data was extracted along a 1D line (linescans), as illustrated in Fig. 4.7. In case of the plasma bulk properties, the results are plotted versus the lateral distance from the hollow. With respect to the surface the flux of atomic H towards the surface is of great interest. The flux was observed to be constant over the whole surface.

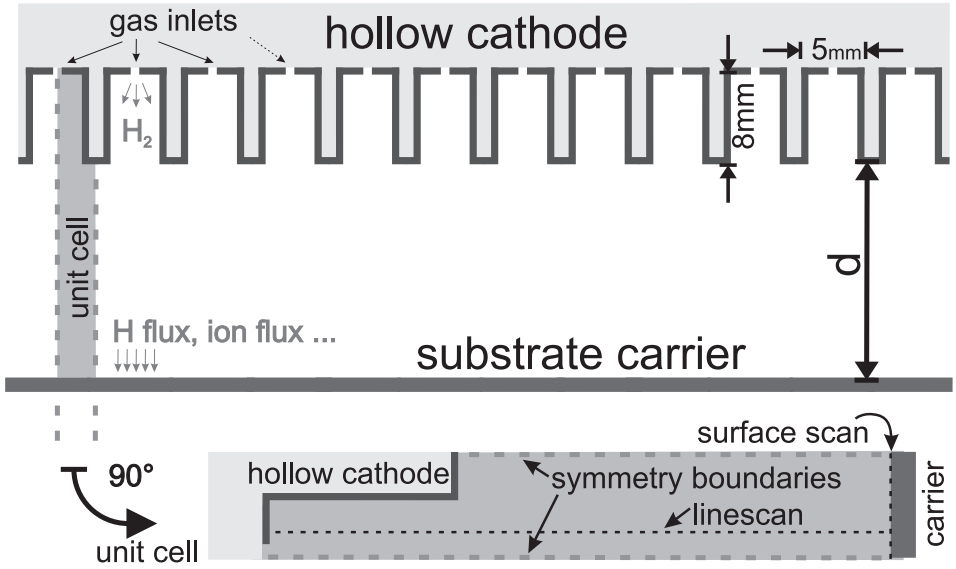

Figure 4.7: Geometric sketch of a two dimensional cross section plane through the plasma setup (upper part). The lower part shows the unit cell, tilted by 90°. For details see text.

4.3.2 Simulation Results

The model was applied to simulate two different states. The first replicates the ignition conditions, i.e. the conditions of minimum voltage, required to ignite H_2 plasmas at 1 mbar for different electrode gaps. Hydrogen passivation on the other hand was performed at a constant power of 50 W (second condition). The cathode voltage (V_{brk} for ignition and V_{pk} for passivation) serves as an input parameter for the simulation (Table 4.1 on page 43). For a gap of 10 mm, a much lower cathode voltage had to be used for the passivation condition than was needed for igniting the plasma. Under this condition the simulation did not return any reasonable solution and therefore cannot be considered.

The aim of the simulation is to obtain a better understanding of the observed correlation between minimum in breakdown voltage and optimum in passivation. Therefore the results of the plasma simulation need to be compared to the experimental V_{OC} data, obtained after HP. An optimum in V_{OC} after HP was observed for electrode gaps, corresponding to minimum breakdown voltages. This is shown in Fig. 4.4 on page 45 for the relevant case of a plasma treatment at 1 mbar. V_{OC} after HP is plotted as a function of electrode gap. The maximum at $d = 20$ mm corresponds to the minimum in breakdown voltage (Table 4.1). The distinct decrease in V_{brk} from 10 mm to 20 mm gap (Table 4.1) is accompanied by a sharp increase in V_{OC}. For larger gaps the V_{OC} falls off slightly again. In the following some plasma properties will be shown

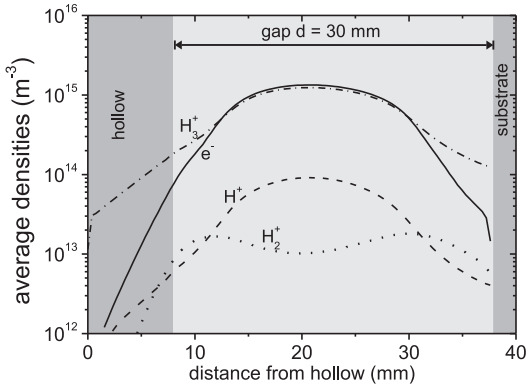

Figure 4.8: Lateral distribution (linescan) of average densities of the most important charge species (e^-, H_3^+, H^+, H_2^+). The gap between cathode and substrate is 30 mm. The inner region of the hollow is illustrated.

to investigate the correlation of breakdown voltage and hydrogen passivation.

Fig. 4.8 depicts the lateral distribution of the average densities of the most important charge species (e^-, H_3^+, H^+, H_2^+) for an electrode gap of $d = 30$ mm. The inner region of the hollow is illustrated. The distribution of negative ions H^- remains 6 orders of magnitude below the density of electrons and is not shown here. The distribution of H_2^+ ions exhibits great similarities to the distribution of power dissipation (not shown here) and consequently of electron heating. This is a typical behavior of highly reactive species in the gas phase, i.e. of species that are consumed spontaneously, very close to the location, where they have been produced. H_2^+ ions react very fast with H_2 molecules towards H_3^+. The dominating ion in the H plasma is therefore H_3^+. It is rather non-reactive in the gas phase. The density is maximized at the center of the plasma, leading to a profile that is determined by diffusion and drift of this species, but also by its consumption at the conductive surfaces of cathode and counter-electrode. Finally, electrons are faster and more mobile compared to either H_2^+ and H_3^+. They are self-adjusted, in order to counterbalance the positive charge, especially in the bulk of the plasma. Thus, their distribution follows the H_3^+ behavior and their density is maximized in the center of the plasma. Due to their high mobility, electrons are consumed more rapidly near the surfaces than the heavier ions. This leads to the formation of the so-called sheaths.

Atomic H density and the amount of atomic H reaching the surface of the sample is expected to be an important quantity for HP. Fig. 4.9 depicts the lateral distribution of atomic H density for different electrode gaps at a H_2

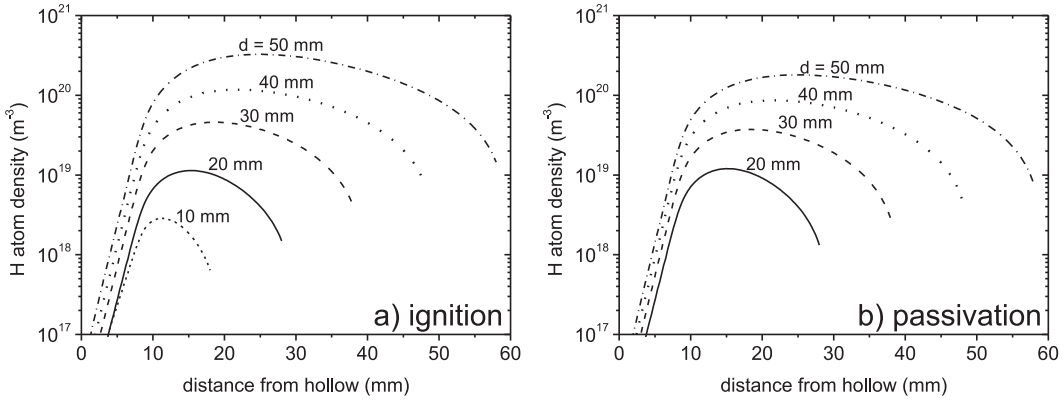

Figure 4.9: Lateral distribution (linescan) of atomic H density for different electrode gaps at a H_2 pressure of 1 mbar, for a) ignition conditions and b) passivation conditions.

pressure of 1 mbar under a) ignition conditions and b) passivation conditions. The increase of electrode gap results in a significant enhancement in atomic H density. The profiles of atomic H density are similar to the distribution of non-reactive ions and electrons. In fact, atomic H has a rather high diffusion coefficient and is consumed in the gas phase only by rather slow reactions. Thus, the profile of this species is mainly determined from its consumption at the electrodes. This can explain the significant increase of H density with electrode gap. The corresponding atomic H flux, reaching the surface is plotted in Fig. 4.10 as a function of electrode gap for both ignition and passivation conditions. In both cases an almost exponential increase in atomic H flux with larger electrode gaps can be observed. H flux directly relates to the atomic H concentration in the plasma. The argument for an enhancement with electrode gap is the same as for atomic H density. The difference between ignition and passivation conditions is based upon the slightly smaller voltages applied for passivation. No correlation can be observed between V_{OC} after HP (Fig. 4.4 on page 45) and the atomic H flux.

Another significant quantity for H passivation could be ions hitting the surface. Under passivation conditions, the averaged ion flux during one cycle (not shown here) remained almost unchanged with changing electrode gap d $\left(\sim 1\,\mathrm{mA/cm^2}\right)$. Before the ions hit the substrate, they are accelerated in the electric field in front of the substrate. The cycle averaged electric field is given in Fig. 4.11 a) as a function of electrode gap. For ignition conditions, a clear minimum is observed at a gap of 20 mm. In both cases the electric field becomes stronger for larger gaps. This means that the ions reaching the substrate

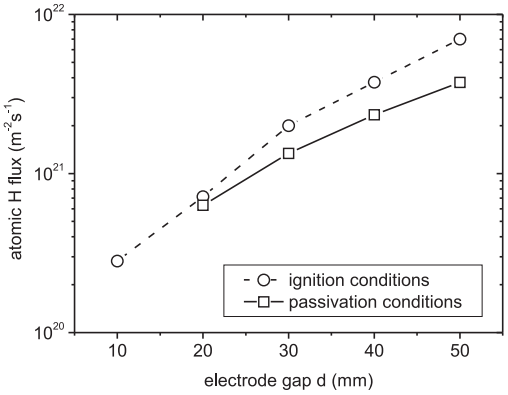

Figure 4.10: Atomic H flux towards the surface, plotted as a function of electrode gap for both ignition and passivation conditions.

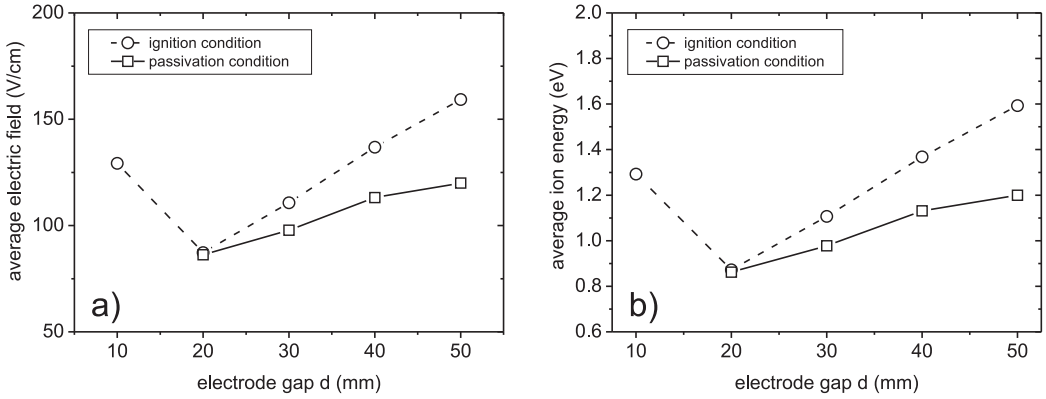

Figure 4.11: a) Cycle averaged electric field, plotted as a function of electrode gap for both ignition and passivation conditions. b) Average ion energy per cycle, calculated with an ion mean free path of 0.1 mm.

gain more energy within the electric field. The dominating ion in the H plasma is H_3^+. The ion mean free path for a 1 mbar H plasma is assumed to be around 0.1 mm [132, 133]. By integrating over the electric field, the ion energy can be estimated. The cycle averaged ion energy, calculated with an ion mean free path of 0.1 mm, is depicted in Fig. 4.11 b). It follows the same trend as the electric field. For ignition and passivation conditions the ions, hitting the substrate, exhibit the lowest energy for an electrode gap of 20 mm. Further increase of electrode gap induces a continuous enhancement of ion energy.

For passivation conditions and an electrode gap of 10 mm the simulation did not return any solution. Most probable this is due to the inefficient sustainment of the plasma in case of the very narrow electrode gap. It is expected that higher electric fields are needed for the narrow electrode gap condition $d =$

10 mm, in order to maintain the plasma ignited. The H flux, on the other hand, is mainly determined from atomic H consumption at the electrodes. With a narrower electrode gap, the consumption of atomic H will increase, leading to less atomic H and a smaller flux. Therefore it is reasonable to assume that under passivation conditions the atomic H flux and the ion energy will follow the same trend as for $d = 10$ mm under ignition conditions.

This would mean that the ion energy exhibits the opposite trend as V_{OC} (in Fig. 4.4) and that the best passivation is obtained for conditions where the ions, hitting the surface, have the lowest energy. However, no correlation can be established between V_{OC} and atomic H flux. Passivation is better for the case of $d = 20$ mm, resulting in a lower H flux than for larger electrode gaps.

4.4 Discussion

The effect of the hydrogen treatment varied strongly with electrode gap d and pressure p. For each pressure (p = 0.1, 0.2, 0.3 and 1.0 mbar), variations of the electrode gap resulted in an optimum electrode gap for passivation treatment, tested by open-circuit voltage measurements. For larger pressures, the optimum gap d shifts to smaller values. At the optimum equal values of V_{OC} were obtained.

To our knowledge, no previous investigations have been published of gap variations for hydrogen passivation of poly-Si solar cells using a capacitively coupled parallel plate plasma setup. Carnel et al. investigated the influence of pressures at a fixed electrode gap [9]. The samples consisted of 5 µm thick, fine-grained polycrystalline silicon solar cell structures, that were deposited on oxidized Si wafers by high-temperature CVD at ~1100°C. The paper reports on hydrogen passivation with an optimum in V_{OC} at a pressure of 2 mbar. At higher and lower pressures the V_{OC} declined [9]. As a first approximation higher pressures are equivalent to smaller electrode gaps, when thinking in terms of $p \cdot d$. Therefore the findings of the paper confirm our results, having used different poly-Si samples and a different CCP setup.

In addition the plasma was characterized measuring the breakdown voltage V_{brk} and the power P_{brk}, needed to ignite the plasma. For each pressure a minimum in breakdown voltage V_{brk} was found at a different gap. As expected [127], the dependence on pressure and electrode gap of the minimum was different to Paschen's law for dc discharges (where V_{brk} depends only on the product $p \cdot d$). In our case, $p \cdot d$, corresponding to the minimum of the Paschen

curve, shifted towards higher values with higher pressures. For each pressure, the best passivation effect in terms of V_{OC} was always accomplished at the point of $p \cdot d$ that corresponded to the minimum in V_{brk}. It is remarkable that the optimum plasma conditions for the passivation of the poly-Si layers can be found by simple and fast measurements of the breakdown voltage V_{brk} at the RF electrode.

Plasma simulations were carried out to obtain some physical understanding of the investigated gap variations. The hollow cathode was simulated with a two-dimensional fluid dynamic code. Fluid dynamic models solve the continuity and transport equations for the various plasma species and the Poisson equation, in order to obtain a self-consistent electric field distribution. In comparison to kinetic models, fluid models require less computational effort and are especially suited for high pressure regimes ($\geq$ 1 mbar), multidimensional problems and for describing detailed plasma chemistry [134, 131]. A recent overview of the major plasma modeling methods can be found in Ref. [134]. Reference [131] demonstrates the complex behavior in rf discharges, using a particle-in-cell/Monte Carlo (PIC/MC) model which also includes negative ions and vibrationally excited molecules.

The average densities and lateral distributions of the most important charge species (e^-, H_3^+, H^+, H_2^+, Fig. 4.8), obtained in this work, are in qualitative agreement with work by other authors, done on simulations of parallel-plate capacitively coupled rf discharges (e.g. [135, 136]). Our modeling of the hollow cathode leads as expected to a slight asymmetry of the lateral distributions (Fig. 4.8). The gap variation studies predict that the electron and atomic H density in the plasma will increase with larger electrode gaps d. This is in agreement with PIC-MC simulations done by Radouane et al. [137], discussing the influence of different electrode gaps.

It might have been speculated that the optimum plasma conditions coincide with an improved generation of atomic H. However, plasma simulations indicate that the best results obtained in the minimum of V_{brk} do not correlate with the conditions of maximum atomic H flux towards the surface. Possibly there is always enough atomic hydrogen available to passivate the samples. This implies that the limiting step for passivation is not the rate of arrival of atomic H to the surface. Consistently, no enhancements can be observed for variations of plasma power. Higher applied power did not lead to an improved HP treatment (Fig. 4.6 on page 46) although it is expected to lead to a higher concentration of atomic H in the plasma. The mechanism in this case could

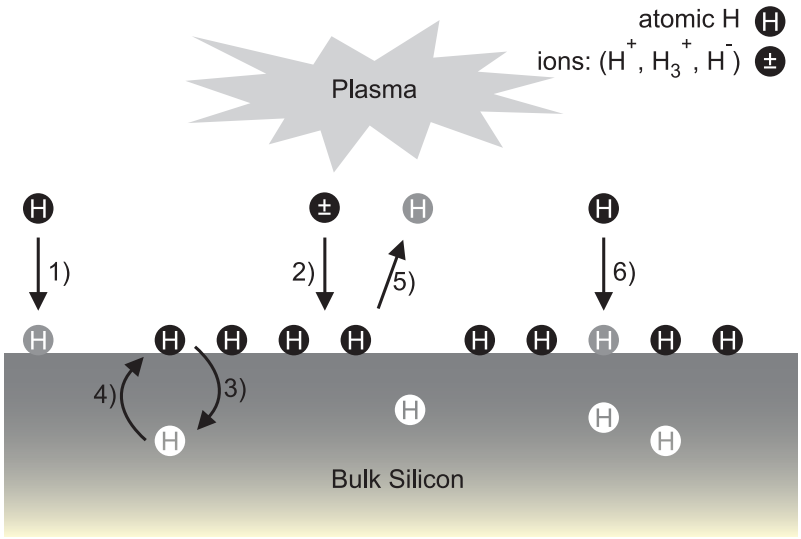

Figure 4.12: Suggested model of hydrogen passivation: 1) H atoms adsorb to the surface, 2) plasma ions hit the surface, 3) H atoms diffuse into the bulk of the material, 4) the rate of H desorption is determined by the ion bombardment and surface temperature, 5) H atoms that diffuse or desorb are immediately replaced by H atoms from the gas phase

be described as illustrated in Fig. 4.12:

1. H atoms from the gas phase (H_g) arrive and adsorb to the surface (H_s): $H_g \rightarrow H_s$
2. In addition plasma ions (mainly H_3^+) are accelerated in the plasma sheath and hit the sample.
3. H atoms diffuse into the bulk of the material and can passivate defects like dangling bonds: $H_s \rightarrow H_{bulk}$
4. H can diffuse back to the surface: $H_{bulk} \rightarrow H_s$
5. H desorbs from the surface. Desorption can include multiple processes:
   a) thermal desorption: $H_s + H_s \rightarrow H_{2,g}$
   b) direct abstraction: $H_g + H_s \rightarrow H_{2,g}$
   c) indirect abstraction: $H_g + H_s + H_s \rightarrow (H_s + H_s + H_s)^* \rightarrow H_s + H_{2,g}$
6. H surface atoms that diffuse into the bulk material or desorb are replaced by H atoms from the gas phase
7. The surface can be etched by H (not relevant at higher substrate temperatures above 350°C): $H_g + SiH_{3,s} \rightarrow SiH_{4,g}$

The sticking probability of H to a Si surface is close to unity [138, 139]. The rate of hydrogen adsorption (1) therefore depends on the H flux. Step (3) and (4) are governed by Fick's law (Eq. 2.1). The net diffusion rate depends on the concentration profile of H and the diffusion coefficient. The diffusion is thermally activated and is enhanced exponentially with temperature. H desorption reduces the H coverage of the surface and includes multiple processes [139]. Thermal desorption is a spontaneous and thermally activated process (5a). Thermal desorption of H, bonded in dihydride and monohydride complexes, will become relevant at temperatures above 400°C and 550°C, respectively [140]. Steps (5b) and (5c) are stimulated desorption processes, which require a high H surface coverage and which are triggered by incoming H atoms or ions. H atoms that diffuse into the bulk material or desorb are replaced by H atoms from the gas phase (6). Etching of the Si surface becomes relevant only at substrate temperatures below 300°C, as it involves trihydride complexes (7) [117, 140]. H in form of trihydride will desorb above 200°C [140].

For passivation the in-diffusion of H (3) must be larger than the out-diffusion (4). Therefore the H surface coverage should be large, which can be achieved by a high atomic H flux (1) from the plasma and a low desorption rate (5). A higher atomic hydrogen flux did not improve V_{OC}. This would indicate that the atomic H flux towards the surface is large, compared to desorption and in-diffusion of H. Otherwise a higher flow of atomic H would be beneficial for the passivation. Passivation for a fixed duration of 10 min is also enhanced by higher substrate temperatures (Fig. 4.3) which causes a faster diffusion of H. Therefore the dynamic of the passivation could be limited by the diffusion (slower rate) rather than the adsorption of H from the plasma to the surface (faster rate). H surface atoms that diffuse into the bulk material or desorb are immediately replaced by H atoms from the gas phase.

Thermal desorption of H from monohydride complexes should become significant at substrate temperatures around 550°C. Going to higher temperatures will increase the desorption rate exponentially. At some point thermal desorption will start to counterbalance H adsorption and the amount of H that can indiffuse into the Si will drop with raising temperature.

The presented model can explain why the hydrogen passivation does not benefit from a higher atomic H flux. If the atomic H flux is not the limiting mechanism and does not affect significantly V_{OC}, it is possible that the passivation process is limited by desorption and in-diffusion of H. It was observed that best passivation conditions correspond to a minimum in electric field and

ion energy. Both quantities vary significantly with electrode gap. The samples are directly exposed to the plasma. Therefore plasma can potentially cause damage to the samples. Ion energy and UV-irradiation from the plasma could potentially lead to defect generation within the poly-Si samples and cause a degradation of the V_{OC}. Yet we do not have any indication so far that the surface of the samples gets visibly damaged (as tested with reflectance measurements in the ultraviolet and visible spectrum). Therefore the origin for the discussed correlation between V_{OC} and ion energy cannot be answered conclusively and clearly more results and investigations are needed to get a better understanding.

To summarize, it can be stated that:

- The variations of plasma process parameters have led to optimized plasma conditions. The passivation effect depends strongly on the interplay of electrode gap d and pressure p. However, no clear trend was observed for the plasma power. The best plasma conditions for the passivation of the poly-Si layers correspond to the minimum in breakdown voltage V_{brk} and can be found by simple and fast voltage measurements at the electrode.

- Optimized plasma conditions do not correlate with the highest hydrogen flux towards the surface, as learned from the plasma simulations. The proposed model could explain why the hydrogen passivation does not benefit from a higher atomic H flux. This observation is confirmed by the plasma power experiments, which showed no effect on V_{OC}. The question whether the optimized plasma conditions can be related to a minimum in electric field and ion energy cannot be answered conclusively. Careful measurements of the plasma would be requiered.

5 Dynamic of the Hydrogen Passivation

In the last chapter plasma conditions like pressure, geometry and pressure have been studied and optimized. This provides the basis for a solid hydrogen treatment on which further investigations can be build upon. In this chapter important process quantities will be researched. The dynamic of H indiffusion and H passivation will be studied closely by means of the two parameters plateau temperature T_{HP} of the hydrogen treatment and the plateau length $t_{plateau}$. As motivated in Sec. 2.3, results about an optimum process temperature T_{HP} during hydrogen plasma treatments diverge and yet no common opinion has been established on how the best H plasma treatment can be achieved. Therefore the temperature T_{HP} will be looked at more closely. A focus will be on the moment, at which the plasma is ignited and at possible degradation due to prolonged hydrogen passivation. Finally, the end temperature, at which the plasma is switched off, will be investigated indirectly by annealing experiments that are designed to investigate the degradation of open-circuit voltage caused by outdiffusion of H.

5.1 Time and Temperature Dependence of Hydrogen Passivation

Hydrogen diffusion in Si shows a thermally activated behavior (Eq. 2.4). This means that the diffusion is very fast for high temperatures and rather slow for low temperatures. The diffusion length $l_{dif} = 2\sqrt{Dt}$ (in Eq. 2.3) is a function of both temperature and time. Therefore time and temperature dependence need to be investigated simultaneously.

CVD-grown solar cell test structures were hydrogen passivated under plasma conditions of 1 mbar and an electrode gap of $d = 20$ mm at different temperatures T_{HP} and time periods $t_{plateau}$. The same solar cell samples as in the previous chapter 4 were used.

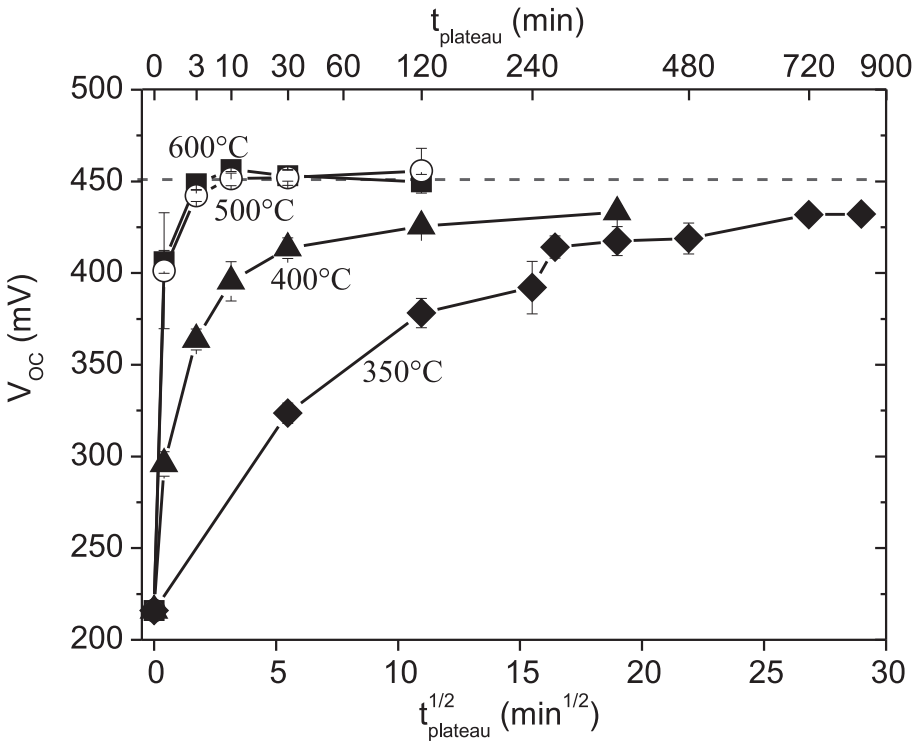

Figure 5.1: Open circuit voltages of poly-Si solar cells passivated at different temperatures of T_{HP} = 350°C, 400°C, 500°C and 600°C plotted versus the square root of $t_{plateau}$. For T_{HP} = 500°C and 600°C the maximum V_{OC} values are obtained very rapidly already after a duration of 10 min.

Fig. 5.1 shows the open circuit voltages of the passivated samples for different passivation temperatures (T_{HP} = 350°C, 400°C, 500°C and 600°C). The V_{OC} is plotted over the square root of the plateau time $t_{plateau}$ (in units of $\sqrt{\text{min}}$, lower x-axis) and accounts for the square root dependence of the diffusion length $l_{dif} = 2\sqrt{Dt}$. In the upper x-axis the time is given in units of min. As a rough estimation the number of defects, passivated with time will directly depend on the diffusion length. The correlation between defect density and V_{OC} on the other hand is expected to be more complex. A more detailed discussion can be found in Chapter 7. In an idealized case of only bulk recombination via midgap states and an ideality factor of $n_1 = 1$, V_{OC} would be proportional to $V_{OC} \propto \ln(\tau)$ [141]. Here τ is the minority carrier lifetime which relates to the defect density n_d via $\tau \propto 1/n_d$. Therefore as expected, no square root dependence of V_{OC} on the duration time of passivation is observed. For T_{HP} = 500°C and 600°C it is observed that the V_{OC} is improved very rapidly by the hydrogen treatment and V_{OC} values above 400 mV are already reached after 10 sec plus cooling down phase. In both cases the

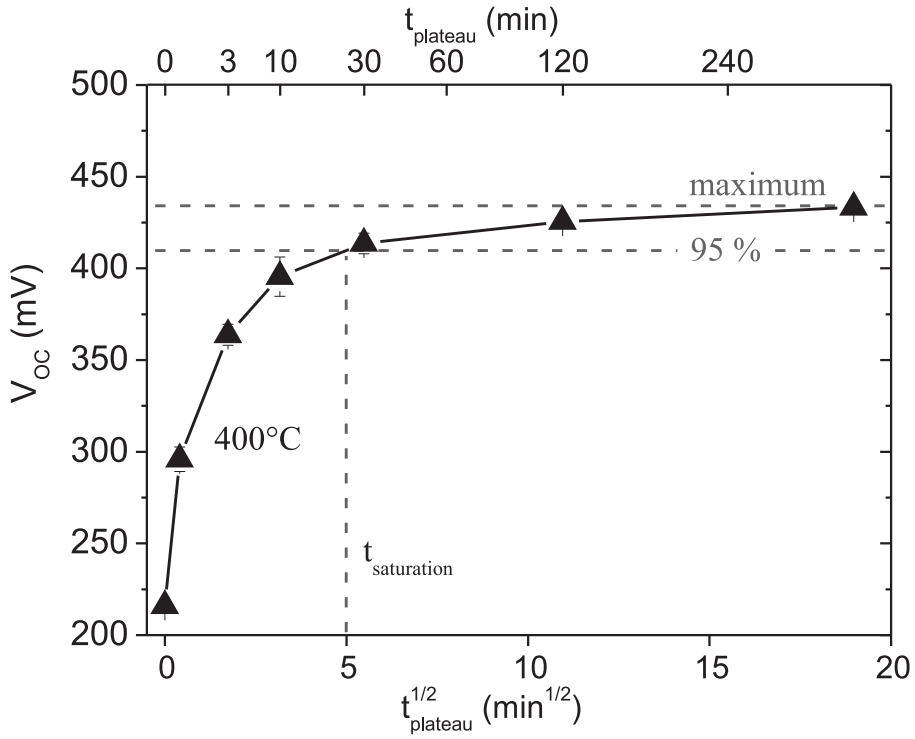

Figure 5.2: Illustration how the saturation time $t_{saturation}$ of the hydrogen treatment is defined for the time dependence of the HP at 400°C. The time when 95 % of the maximum V_{OC} is reached is determined to be $t_{saturation}$.

maximum values are obtained already for a duration of 10 min and the values saturate. After this no significant further improvement can be observed.

For the lower temperature range of $T_{HP} = 350$°C and 400°C the dynamic of the hydrogen treatment is much slower and it takes longer to reach high V_{OC}. The results suggest that the V_{OC} is still not completely saturated. On the other hand it seems that high values of 450 mV are unlikely to be reached. The longest treatments at $T_{HP} = 500$°C and 600°C where performed for 2 hours while at $T_{HP} = 400$°C and $T_{HP} = 350$°C passivation was applied for 6 and 14 hours, respectively. This suggests that the dynamic of hydrogen passivation is limited by slow diffusion of H for temperatures below $T_{HP} \leq 400$°C. At low temperatures it takes the hydrogen several hours to diffuse completely through the 1.4 µm thick Si film.

The time needed to passivate the structure can be evaluated further. For each temperature of the hydrogen treatment a saturation time $t_{saturation}$ will be defined as the time, when 95% of the maximum V_{OC} is reached (as illustrated in Fig 5.2). The point $t_{saturation}$ was determined by numerically interpolating between the individual data points.

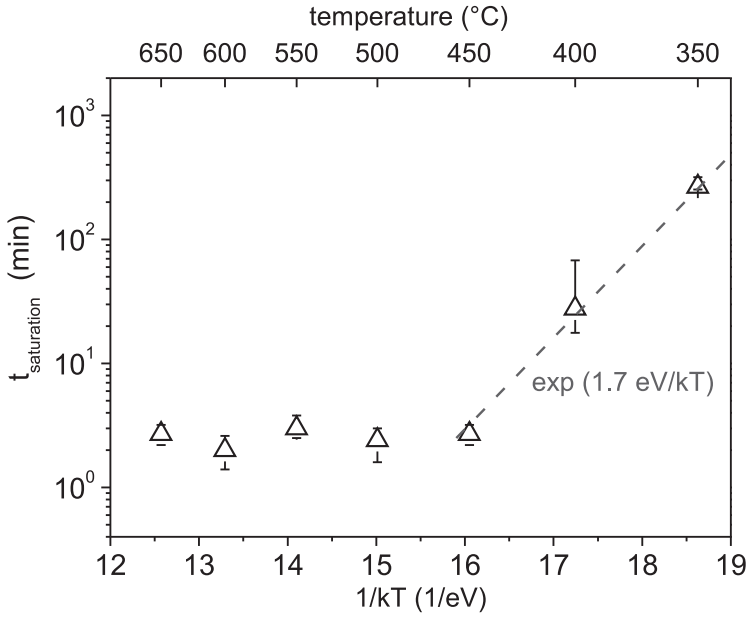

Figure 5.3: Saturation time $t_{saturation}$ plotted logarithmically versus the inverse hydrogen treatment temperature T_{HP} (in units of 1/eV). The upper x-axis displays the equivalent temperatures. Higher temperatures lead to shorter process times, that are reduced over two orders of magnitude by going from 350°C to 450°C.

In Fig. 5.3 the saturation time $t_{saturation}$ is plotted logarithmically versus the inverse plateau temperature T_{HP} (in units of 1/eV, lower x-axis) of the hydrogen treatment in an Arrhenius plot. The equivalent temperatures are displayed in the upper x-axis. Higher temperatures lead to lower $t_{saturation}$. In the temperature range of 350°C to 450°C, $t_{saturation}$ is reduced over two orders of magnitude from almost 300 min at 350°C to less than 3 min for temperatures $\geq$ 450°C. For temperatures above 450°C it was not possible to observe significant changes in $t_{saturation}$, which could be due to extremely short process times. For temperatures $\leq$ 450°C a thermally activated behavior can be observed and $t_{saturation}$ can be fitted with an Arrhenius function $t_{saturation} = t_0 \exp\left(\frac{E_a}{kT}\right)$. The inclination observed in Fig. 5.3 corresponds to an energy of $E_a = 1.7 \pm 0.2$ eV (with $t_0 = 4.5 \times 10^{-12}$ min).

The so far investigated samples all feature an identical structure and the same layer thickness. The emitter of the solar cell structure is located at the glass side of the Si stack. The open circuit voltage of the device will be in particularly sensitive to the defect density near the emitter. Therefore we assume that H has to diffuse completely through the Si layer in order to fully improve the V_{OC} of the solar cell device structure. As a first approximation it is estimated that the saturation time corresponds to the H diffusion time.

The constant layer thickness d_{Si} is then equated to the H diffusion length

$$d_{Si} \simeq l_{dif} = 2\sqrt{D\, t_{saturation}} \tag{5.1}$$

It follows that $t_{saturation}$ is inversely proportional to the diffusion coefficient of H

$$D \simeq \frac{d_{Si}^2}{4} \cdot t_{saturation}^{-1} \tag{5.2}$$

If the assumptions are correct, the determined activation energy $E_a = 1.7 \pm 0.2$ eV can be identified as the activation energy for H diffusion. The diffusion prefactor can also be estimated via the relation:

$$D = D_0 \exp\left(-\frac{E_a}{kT}\right) \tag{5.3}$$

From the data points that show an activated behavior in Fig. 5.3, the diffusion prefactor is estimated to be $D_0 \simeq 18 \pm 3$ cm^2/s. Determined activation energy and diffusion prefactor are in agreement with results found in the literature (see Fig. 5.9 on page 70). This demonstrates that within the temperature range $T_{HP} \leq 450$°C the passivation process is governed by an activated H diffusion. Higher temperatures lead to a faster H diffusion and a faster passivation. For $T_{HP} \geq 450$°C, it is observed that the V_{OC} is improved very rapidly by the hydrogen treatment and V_{OC} values above 400 mV are already reached after 10 sec plus cooling down phase. In the next section a closer look will be taken at the temperature in terms of optimum treatment and degradation effects of V_{OC}.

5.2 Optimum Temperature

In the previous section the time behavior of the hydrogen treatment was investigated for different temperatures. At temperatures $T_{HP} \leq 400$°C it takes several hours of passivation to reach high V_{OC} values. The data in Fig. 5.1 further suggests that the samples passivated at lower temperatures might saturate below the maximum V_{OC} of the samples passivated at higher temperatures. Even if not the case, fast processes are desired from an industrial point of view to reach high throughput in production. To gain better insight into the influence of the temperature, passivation experiments were repeated in smaller temperature intervals of 50 K for three different plateau time periods of $t_{plateau} = 3$, 10 and 30 min in the temperature range of 400 to 650°C.

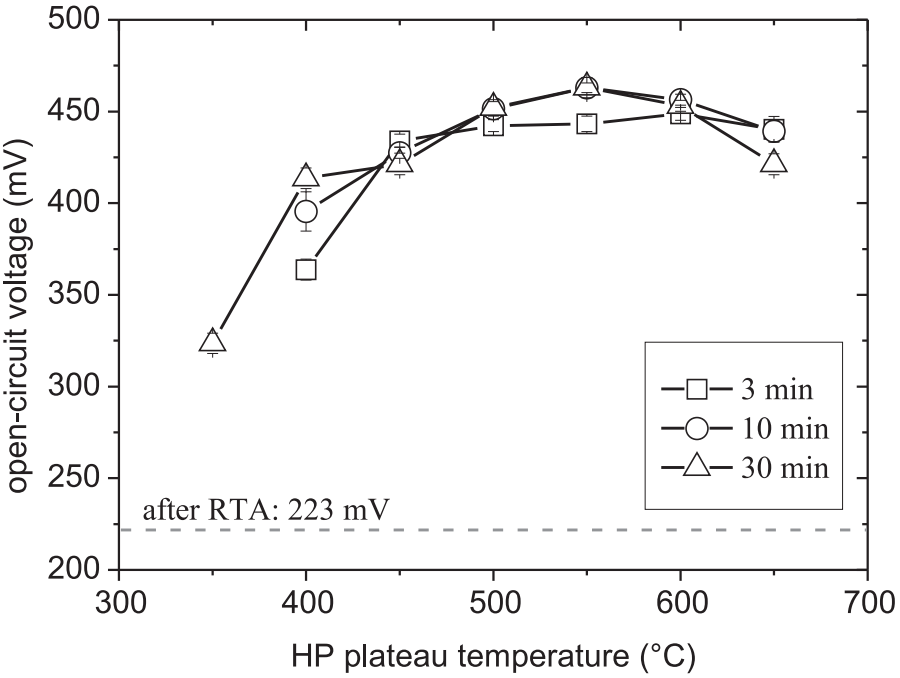

Figure 5.4: Open circuit voltages of poly-Si solar cells, passivated for different plateau time periods ($t_{plateau}$ =3, 10 and 30 min) and plotted as a function of passivation temperature T_{HP}.

The measured V_{OC} after hydrogen passivation is shown in Fig. 5.4 for three different plateau times of $t_{plateau}$ = 3, 10 and 30 min. In addition the value of $T_{HP} = 350°C$ after 30 min is given. A significant improvement in V_{OC} is observed in the whole temperature range. Except for the samples passivated at $T_{HP} = 350$°C for 30 min and $T_{HP} = 400$°C for 3 and 10 min, where the dynamic is still limited by slow H diffusion, V_{OC} is improved after HP from $\sim$ 223 mV to a value ranging between 400 and 465 mV. For temperatures $T_{HP} \geq 450$°C a treatment time of $t_{plateau} = 10$ min results in an equal or higher V_{OC} than after 30 min. Therefore a treatment time of $t_{plateau} = 10$ min seems to be sufficient. An optimum is observed for treatments at $T_{HP} = 550$ °C ($t_{plateau}$ = 10 and 30 min) leading to the best average $V_{OC} = 463 \pm 5$ mV of this series. The best value of 470 mV, measured at a specific position of the sample, was also obtained at a passivation temperature of 550°C. The best average V_{OC} values measured for 500 and 600°C were 452 ± 4 and 455 ± 3 mV, respectively.

It is interesting to note that for $T_{HP} = 450$°C V_{OC} decreases slightly for prolonged hydrogenation. The V_{OC} after passivation is already maximized after roughly 3 min. This indicates that the observed maximum in Fig. 5.4 is not due to enhanced H diffusion at higher temperatures. Moreover V_{OC}

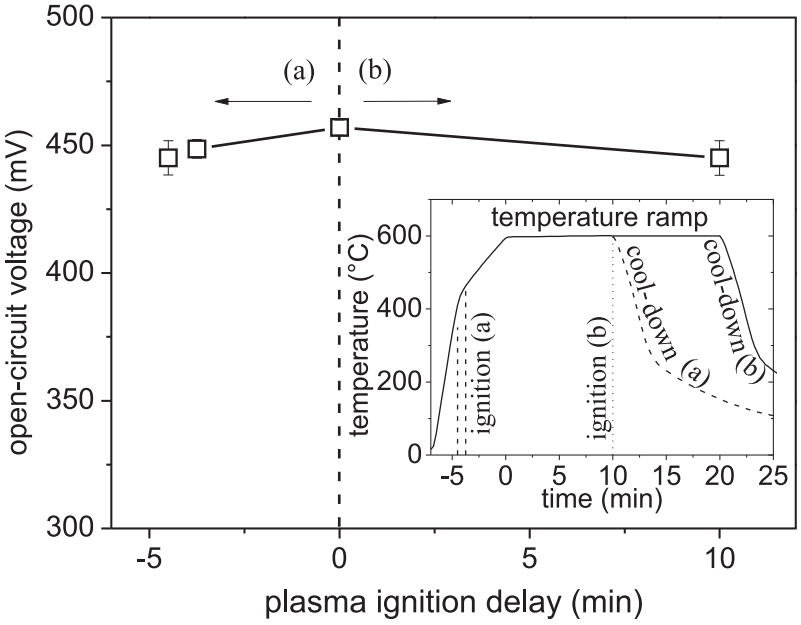

Figure 5.5: Open circuit voltages of poly-Si solar cells, passivated at $T_{HP} = 600°C$ for $t_{plateau} = 10$. The ignition time was varied, as illustrated in the inset, showing the temperature profile of the samples. In case (a) the plasma was ignited before reaching the plateau temperature of 600°C. In case (b), the samples were annealed at 600°C for an additional 10 min, before igniting the plasma for another 10 min at 600°C.

decreases also for $T_{HP} = 650°C$ with longer hydrogenation time.

Experiments were conducted to investigate whether an ignition at lower temperatures before reaching the high plateau set-temperature could be beneficial. As described before, the native oxide of the samples was removed by an HF dip before loading the samples into the plasma chamber. This leaves the Si surface H-terminated, which also serves as a protection against impurities to be adsorbed at the surface. H-termination of Si surfaces is known to be temperature stable only to intermediate temperatures and the H desorbs at temperatures of around 450°C to 550°C [140]. Early ignition of the plasma could prevent H desorption.

Fig. 5.5 shows the open circuit voltages of poly-Si solar cells as a function of ignition time. The samples were passivated at $T_{HP} = 600°C$ for $t_{plateau} =$ 10 min. The ignition time was varied, as illustrated in the inset of Fig. 5.5. In case (a) the plasma was ignited during the ramp-up phase, before reaching the plateau temperature of 600°C (at -4.5 min and -3.75 min, corresponding to a substrate temperature of 350°C and 460°C, respectively). The plateau time was 10 min. In case (b), an additional anneal was performed at 600°C

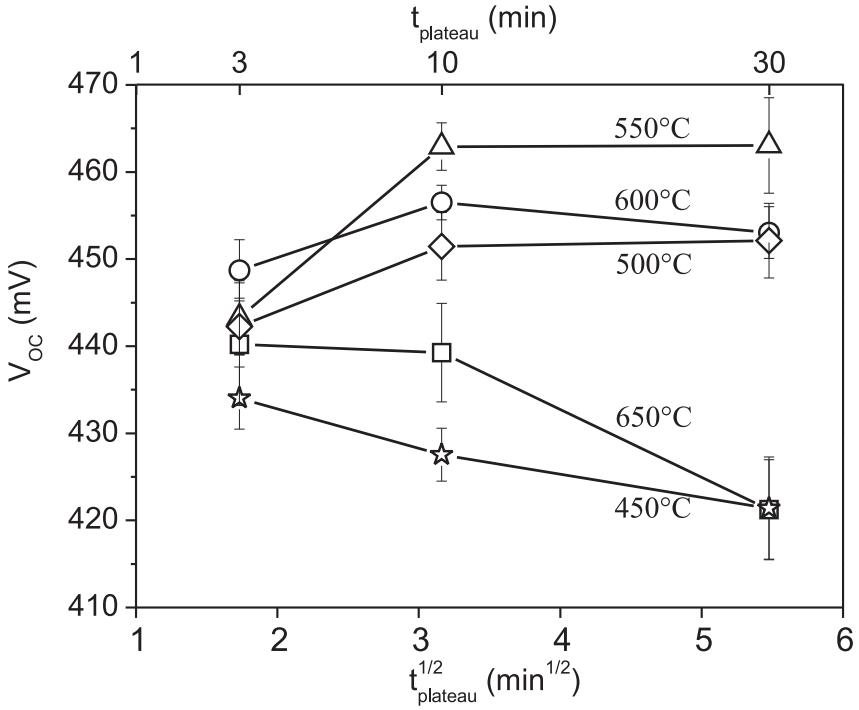

Figure 5.6: Open circuit voltages of poly-Si solar cells, passivated at different temperatures T_{HP} and plotted as a function of passivation plateau time.

for 10 min, before igniting the plasma for another 10 min at 600°C. The total plateau time in this case is 20 min, with the plasma burning for 10 min plus cooling down phase.

Ignition at lower temperatures of 350°C and 460°C leads to lower V_{OC} values, compared to samples where the plasma was ignited directly after reaching the plateau temperature of 600°C. From the results in Fig. 5.5 it can be concluded that an early ignition at lower temperatures during the ramping-up phase is not beneficial, but even leads to lower V_{OC} values. This could indicate that the surface termination by H during ramp-up does not play a very important role. On the other hand a delay of 10 min at 600°C also leads to lower V_{OC} values. The fact that lower V_{OC} values are reached in combination with an early plasma ignition, supports the observed optimum in Fig. 5.4 at a passivation temperature of 550°C. It indicates that the temperature, at which the plasma is ignited might have a significant influence on the result of the hydrogen passivation.

It was already mentioned that with prolonged hydrogenation in some cases (e.g. Fig. 5.1 and 5.4) the V_{OC} first reaches a maximum value after 3 to 10 min and then slightly declines again. This is illustrated more closely in Fig. 5.6 with the open circuit voltages of samples from Fig. 5.4, plotted as a

function of passivation plateau time. The different temperatures T_{HP} are given as parameters. Except for $T_{HP} \leq 450$°C, the maximum V_{OC} values are reached after 10 min of passivation. In the case of $T_{HP} = 500$°C and 550°C, no decline in V_{OC} is observed for durations longer than 10 min. For all other treatments at lower ($T_{HP} = 450$°C) and higher temperatures ($T_{HP} = 600$°C and 650°C) a degradation of V_{OC} can be observed. This effect is most pronounced for $T_{HP} = 450$°C and 650°C.

5.3 H Out-Diffusion

The cooling-down phase is an important part of the hydrogen passivation treatment. As was shown, the applied plasma treatment is most effective in terms of V_{OC}, when carried out at rather high temperatures in the range of 500°C to 600°C. One challenge is to cool down the samples afterwards without loosing considerable amounts of H due to out-diffusion.

H out-diffusion is avoided by keeping the plasma ignited during cooling-down the samples. To protect the glass-substrates from damage, a controlled slow cooling rate is favored. On the other hand, faster cooling rate will prevent H out-diffusion. The cooling-down ramp is illustrated in Fig. 3.7 (page 33). The plasma remains ignited until samples reach the plasma end temperature of 350°C. In case of 600°C it takes 3 min to reach 350°C at a rate of 83 K/min. After that the plasma is switched off and the samples are cooled down further.

In order to investigate the effect of cooling-down on the out-diffusion of H and degradation of V_{OC}, hydrogenated poly-Si solar cells were annealed in H_2 ambient (1 mbar) at different temperatures without the plasma ignited. Prior, all samples received a hydrogen treatment at 1 mbar and 600°C for 10 min. Then the V_{OC} was measured and the samples were subsequently annealed for a certain time. Afterwards the V_{OC} was measured again. The normalized $V_{OC} = V_{OC}^{(after\,anneal)}/V_{OC}^{(before\,anneal)}$ is shown in Fig. 5.7 as a function of annealing temperature with annealing time (1 - 30 min) given as a parameter.

The anneal in H_2 ambient at temperatures above 450°C leads to a significant and rapid loss in V_{OC}. For short annealing durations of 1 min, the decline is larger than 10 %. For lower annealing temperatures the deterioration of V_{OC} is less severe. This is illustrated in Fig. 5.8 showing the normalized V_{OC} for the temperatures of 300 - 400°C as a function of annealing time. Within the error range of ∼1% no change can be evidenced after an annealing for 3 min at 300°C. The V_{OC} declines to 99 % and 97 % of the initial value after 10 min and

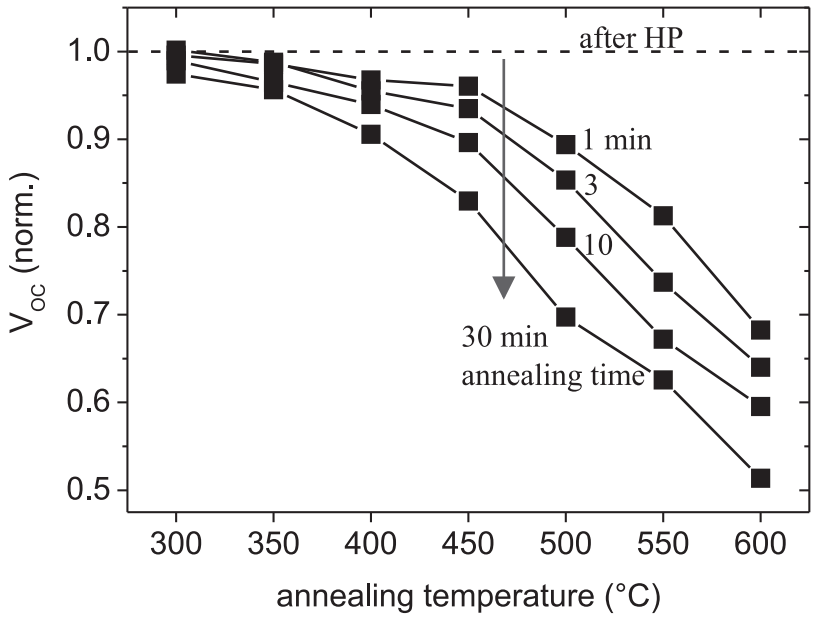

Figure 5.7: Normalized V_{OC} of hydrogenated poly-Si solar cells after annealing as a function of annealing temperature with the annealing time (1 - 30 min) given as parameter.

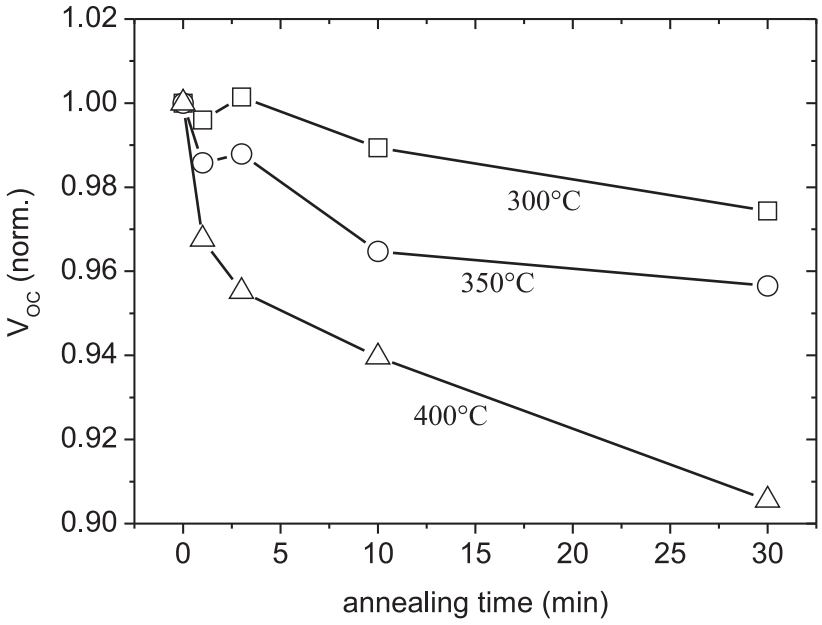

Figure 5.8: Normalized V_{OC} of hydrogenated poly-Si solar cells after annealing as a function of annealing time with the annealing temperature (300 - 400 °C) given as parameter (carried out in H_2 ambient).

30 min annealing, respectively. Also for a temperature of 350°C, the deviation is less than 2 % within the first 3 minutes.

After switching off the plasma, the samples will cool down from 350°C to 300°C in less than one minute. Therefore it can be concluded, that a plasma end-temperature of 350°C will be sufficient to prevent any significant degradation of V_{OC} due to out-diffusion of H. A higher end-temperature of 400°C, on the other hand, could already lead to a noticeable loss in V_{OC} ($\sim 4\%$).

The end-temperature of 350°C was chosen intentionally to counterbalance two effects: i) H out-diffusion, as described above, which requires low end-temperatures and ii) the etching of the Si surface by atomic H, which starts to become relevant at temperatures below 350°C [117]. At temperatures below 200°C, the Si surface will be mostly terminated by H [140]. The H will form mono-, di- and trihydride complexes with the Si [142]. In this case, a Si adatom is bonded only weakly and can be removed easily in form of SiH_4 and etching can be observed. H in form of trihydride, dihydrides and monohydride complexes will desorb above 200°C, 400°C and 550°C, respectively [140].

Indeed, AFM measurements of monocrystalline silicon surfaces, exposed to an RF remote H plasma at temperatures of 450°C to 700°C did not reveal any observable changes in the surface roughness, potentially caused by plasma etching [117]. However, for temperatures below 300°C a significant roughening of the surface was evidenced [117].

5.4 Discussion

Diffusion It was observed that for $T_{HP} \leq 450$°C the passivation process is governed by an activated behavior. If a maximization of V_{OC} can be attributed to the complete H penetration of the Si films, the behavior can be attributed to H diffusion. Higher temperatures lead to a faster H diffusion and a faster passivation. The activation energy and diffusion prefactor were experimentally determined from the data in Fig. 5.3 to be $E_A = 1.7 \pm 0.2$ eV and $D_0 \simeq 18$ cm^2/s, respectively. The activation energy is much larger than 0.5 eV, as is observed for high temperature hydrogen diffusion in c-Si via Si BC sites [17]. Similar high activation energies of 1.69 eV are reported in the literature for H diffusion from a solid source in SPC based poly-Si [55]. Also the diffusion prefactor differs significantly from $9.67 \cdot 10^{-3}$ cm^2/s, determined by Van Wieringen and Warmoltz [17]. In Fig. 5.9 the diffusion prefactor D_0 is plotted versus experimentally measured activation energies E_A for different

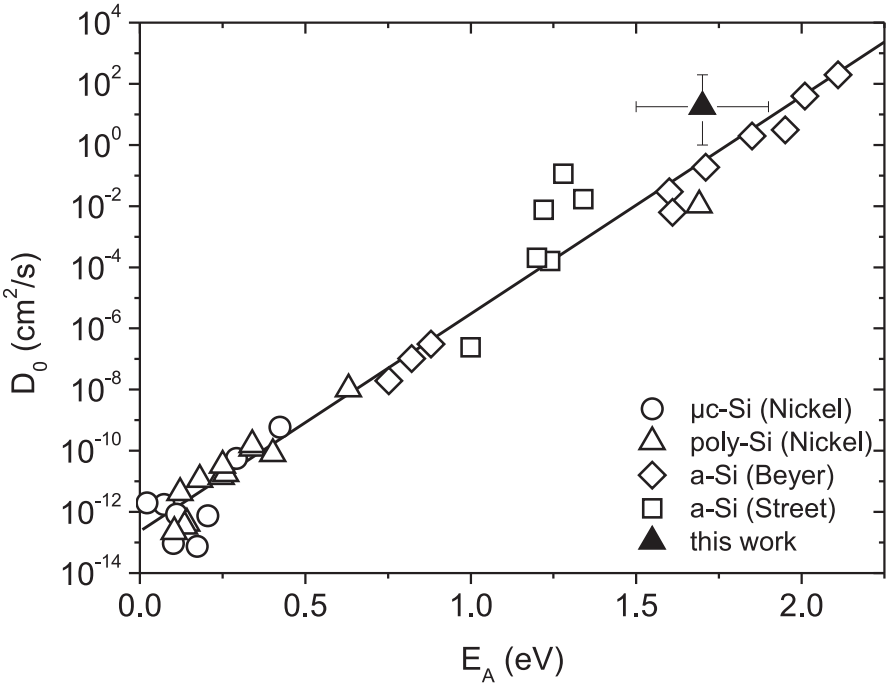

Figure 5.9: Diffusion prefactor D_0 plotted versus activation energy E_A after Ref. [40]. Poly-Si and µc-Si (Nickel) are taken from Ref. [40], the data from Beyer [143] and Street [144] were obtained from H diffusion in a-Si.

Si materials (after Ref. [40]). The data for poly-Si and µc-Si (Nickel) are taken from Ref. [40], the data from Beyer [143] and Street [144] were obtained from H diffusion in a-Si. It can be observed that there is a strong dependence of the prefactor on the activation energy, showing a so-called Mayer-Neldel behavior [145]. The same behavior was also observed for H diffusion in a-Si [146]. Noticeable this correlation is the same for a-Si, µc-Si and poly-Si and consequently independent of the degree of macroscopic disorder.

D_0 changes over more than 15 orders of magnitude. In theory, the diffusion prefactor should be independent of experimental parameters or activation energy and equal to the microscopic prefactor $D_0^{micro} = \frac{1}{6} a_D^2 \omega_0$, which is given by the traps attempt-to-escape frequency ω_0 and the distance a_D between sites. It is independent of other parameters like Fermi energy, defect densities or hydrogen concentration. A Mayer-Neldel behavior can be observed, when the physically relevant activation energy $\bar{E_A}$ depends linearly on the temperature [146]. The leads to a different, measured activation energy E_A, which can be corrected taking into account the microscopic diffusion prefactor D_0^{micro}

(estimated to $D_0^{micro} \approx 10^{-3}\mathrm{cm}^2/\mathrm{s}$) [55]

$$\bar{E_A}(T) = E_A - kT \ln\left(\frac{D_0}{D_0^{micro}}\right) \tag{5.4}$$

Two different models have been proposed to describe the hydrogen migration in non-monocrystalline Si (see also Fig. 2.2), the *equilibrium model* and the *trapping model*. Both models consider deep trap states that are separated in energy from the transport states. The energy gap to the transport states is large and the energy level of deep traps $E_t^{(H)}$ resides 1.5 to 1.7 eV below E_M (Fig. 2.2 on page 16). H transport occurs through migration of charged interstitial H states (BC and T_d sites for H^+ and H^-, respectively) by surmounting the energy barrier E_M.

The *equilibrium model* is based on the assumption that the occupied and unoccupied H density-of-states are in thermal equilibrium [147]. The H concentration in the transport states is controlled by the H chemical potential μ_H. H has to overcome the energy barrier $E_M - \mu_H$ to migrate. The energy difference corresponds to the (physically relevant) activation energy $\bar{E_A}$.

The *trapping model* considers that H within deep traps is not equilibrated due to trapping and de-trapping processes occurring on longer time scales than H migration within shallow transport states. If μ_H resides below the energy level of $E_t^{(H)}$ the activation energy is given by $\bar{E_A} = E_M - E_t^{(H)}$ [148, 149]. Otherwise the activation energy is the same as in equilibrium (i.e. $\bar{E_A} = E_M - \mu_H$).

In this case $\bar{E_A} = E_M - \mu_H$ can be taken to determine the position of the hydrogen chemical potential μ_H [55, 143]. For the data points that show an activated behavior in Fig. 5.3 ($T_{HP} \leq 450°C$) the corrected activation energy $\bar{E_A}$ is calculated to be between 1.2 and 1.0 eV after Eq. 5.4. It is clearly above the reported energy level $E_t^{(H)}$ for H deep trap states (1.5 - 1.7 eV) [39]. For temperatures $T_{HP} > 450°C$ the saturation time $t_{saturation}$ remains constant within the error range and no activated behavior can be observed. In average V_{OC} is maximized after 10 min and 95 % is reached after $t_{saturation} = 3 \pm 0.4$ min.

Optimum Temperature The presented results indicate, that a hydrogen treatment at rather high temperatures seems to be well suited for defect passivation of poly-Si solar cell structures. In terms of V_{OC} an optimum treatment temperature around 550°C is identified (Fig. 5.4). In addition, a plasma treatment at lower temperatures ($\leq$ 400°C) takes several hours to improve signifi-

cantly V_{OC} and hence is irrelevant for industrial processes, which require high throughput. Hydrogen treatments of the same sample structure but in two different remote inductively-coupled plasma setups have led to similar conclusions, stating a broad optimum range at high temperatures of around 610°C [8]. Kunz et al. recently published a poly-Si solar cell with 5 % efficiency, based on a defect passivation treatment, carried out at temperatures of 650°C with an inductively coupled remote plasma source [28]. This indicates that hydrogen passivation at high temperatures is beneficial and feasible.

The reason for the observed optimum at high temperatures is not yet very clear. One possible explanation could be the following. With increasing treatment time, hydrogen diffuses into the sample and passivates Si dangling bonds. The diffusion $D = D_0 \cdot \exp\left(-\frac{E_A}{kT}\right)$ is thermally activated. In parallel also new defects are generated, e.g. the breaking of Si-H bonds and hydrogen breaking weak Si-Si bonds.

At the beginning, the initial defect concentration is high and the rate at which H passivates these defects is higher than the rate at which new defects are generated. After a certain time H has diffused completely through the sample and the majority of the defects has been passivated. This is characterized by a balance between the defect passivation rate that has reached a minimum and the generation rate of defects due to Si-H and Si-Si bond breaking. At this point in principle thermodynamic equilibrium should be reached, where the defect generation rate is exactly compensated by the rate of defect passivation and in average no additional defects are created or annihilated.

In principle this should lead to a saturation of passivated dangling bonds and therefore also a saturation of V_{OC}. However, in most cases a saturation was not observed. Prolonged hydrogenation led to a degradation in V_{OC} after initially reaching a maximum value. This suggests that the dynamic of the hydrogen passivation treatment in terms of V_{OC} is not only governed by thermodynamic equilibration of pre-existing dangling bonds.

The passivation of dangling bonds is a microscopic effect that occurs during passivation. V_{OC} on the other hand is a macroscopic electronic quantity that depends on the splitting of the quasi-Fermi levels for electrons and holes. It is very sensitive to the lifetime of the charge carriers (in case of a one-sided junction to the lifetime of the minority charge carriers). Any kind of electrically active defects that enhance the recombination and lower the lifetime will lead to a decline in V_{OC}.

As seen in Fig. 5.6, prolonged hydrogenation ($\geq$ 30 min) leads to a degra-

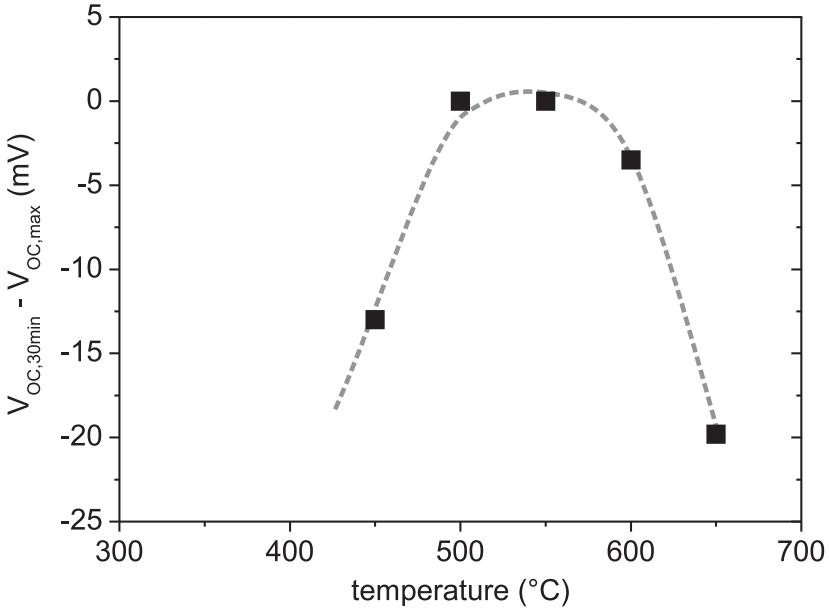

Figure 5.10: Loss in open circuit voltage after 30 min hydrogenation, plotted as a function of temperature and calculated from data in Fig. 5.6 (difference between maximum V_{OC} and V_{OC} reached after 30 min).

dation of V_{OC} after initially reaching a maximum value after 3 to 10 min. The degree of degradation is summarized in Fig. 5.10. The loss in V_{OC} after 30 min compared to the maximum V_{OC} (e.g. $V_{OC}^{30min} - V_{OC}^{max}$) is calculated and plotted versus T_{HP}. The analysis suggests a temperature dependent deterioration of V_{OC}, which is only weakly pronounced around 550°C and strongly pronounced for $T_{HP} = 450$°C and 650°C. Also a passivation at $T_{HP} = 600$°C, but with an earlier plasma ignition at lower temperatures, resulted in a loss in V_{OC} (Fig. 5.5). The temperature dependent degradation suggests that simultaneously with defect passivation, new defects are generated. The V_{OC} does not saturate with time but first reaches a maximum and subsequently starts to degrade with prolonged HP. The degree of degradation is minimized and nearly zero around $T_{HP} = 550$°C and coincides with the observed optimum passivation temperature.

The nature of the type of defect generation cannot be concluded from the conducted experiments but can only be speculated. In addition to passivation of pre-existing dangling bonds it is possible that also secondary defect creation mechanisms influence the lifetime of the charge carriers and therefore the device performance in terms of V_{OC}.

Hydrogen mediated defect generation includes the breaking of weak Si-Si

bonds either by a single H atom, leaving behind a non-passivated Si dangling bond or by two H atoms. The double occupied state (later process) is energetically favored and exhibits a negative correlation energy [150]. Breaking of weak Si bonds will alter the H density of states, revealing the complexity of H passivation. The occupation of the single and double occupied states will depend on the energetic levels with respect to the chemical potential μ_H and also on the temperature. Possible diatomic H complexes include H_2^*, where one H atom is placed at the bond-center site and the second H atom at the interstital antibonding site (T_d) [151] and the formation of H platelets [83, 84]. Platelets are thought to consist of H_2^* accumulated complexes [152] and are favored in the lower temperature range [153]. Open circuit voltage will also be affected by doping passivation. Passivation of B in p-type Si was observed at low temperatures [69, 70, 71]. This would lead to additional defects that not necessarily affect the Si dangling bond concentration, but will deteriorate the performance of the device by either reducing the lifetime and diffusion length of the charge carriers or by affecting the doping profile. In addition, comparison of plasma parameter variation and simulation in Chapter 4 hint that the electric field in the plasma and hence the ion energy could play a role. This could explain why other groups using different sample structures and plasma setups might find different optimum temperature regimes. Using for example an RF-ECR hydrogen plasma source for HP of poly-Si solar cells (deposited directly via CVD at 1080°C) Fosca et al. found a favorable passivation regime at around 450°C [30].

To summarize:

- A plasma treatment in the lower temperature range ($\leq$ 400°C) is slow and takes several hours to significantly improve V_{OC}. Furthermore the results were inferior to treatments at higher temperatures within the investigated plateau time of up to 14 h. Such long durations are too time-consuming to be implemented into an industrial process. Therefore this regime is irrelevant for an industrial application.

- For $T_{HP} \leq$ 450°C the passivation process is governed by an activated behavior. Higher temperatures lead to a faster H diffusion and a faster passivation. The activation energy and diffusion prefactor were experimentally determined to be $E_A = 1.7 \pm 0.2$ eV and $D_0 \simeq 18$ cm^2/s, respectively. This is in agreement with values from the literature (Fig. 5.9). The corrected and physically relevant activation energy $\bar{E_A}$ is calculated to be between 1.2 and 1.0 eV. For temperatures $T_{HP} >$ 450°C the

saturation time $t_{saturation}$ remains constant within the error range and no activated behavior can be observed. V_{OC} is maximized after 10 min.

- Prolonged hydrogenation leads to a degradation in V_{OC}. This suggests that the dynamic of the hydrogen treatment is not only governed by thermodynamic equilibration. The loss in V_{OC} with prolonged hydrogenation is more severe for temperatures below 500°C and above 600°C. Best results in terms of V_{OC} were achieved for $T_{HP} = 500 - 600$°C with a weakly pronounced optimum at $T_{HP} = 550$°C leading to the best average $V_{OC} = 463 \pm 5$ mV of this series. Within this temperature range the observed decrease in V_{OC} for long passivation times is minimal.

6 Interaction of Passivation with Material Properties

In the previous chapters one specific poly-Si material has been investigated. Nevertheless, the material properties of the samples could have an important impact on the final result after hydrogen passivation. Therefore the interplay of material quality and hydrogen passivation will be studied in this chapter. The material properties are modified and tuned in two different ways.

In the first section of the chapter, the material properties are modified by different RTA treatments. HP is performed on RTA and non-RTA treated samples and the influence of RTA on the dynamics of HP is studied. In a further step the RTA treatment is varied and the conditions of HP are kept constant.

In the second part of the chapter, investigations are extended towards poly-Si samples with varying structural properties (i.e. different grain sizes). Poly-Si absorbers are deposited by electron beam evaporation (EBE). In comparison to CVD, neither hydrogen nor toxic gases are involved. EBE features high deposition rates of around 1 µm/min and offers a high cost reduction potential. The material properties of these layers can be varied easily by tuning the substrate temperature during Si deposition and will be investigated. The interplay between material properties and hydrogen passivation will be investigated in terms of defect concentration of Si dangling bonds and V_{OC}. On solar cell level, the interaction on RTA will be tested, as well. The aim is to develop high quality EBE-grown poly-Si absorber layers that can compete with or even outperform conventionally grown (CVD) absorber layers.

6.1 Influence of Defect Annealing on Hydrogen Passivation

In this section, the material properties are modified by different RTA treatments. In the first part, hydrogen passivation of non-RTA treated samples is

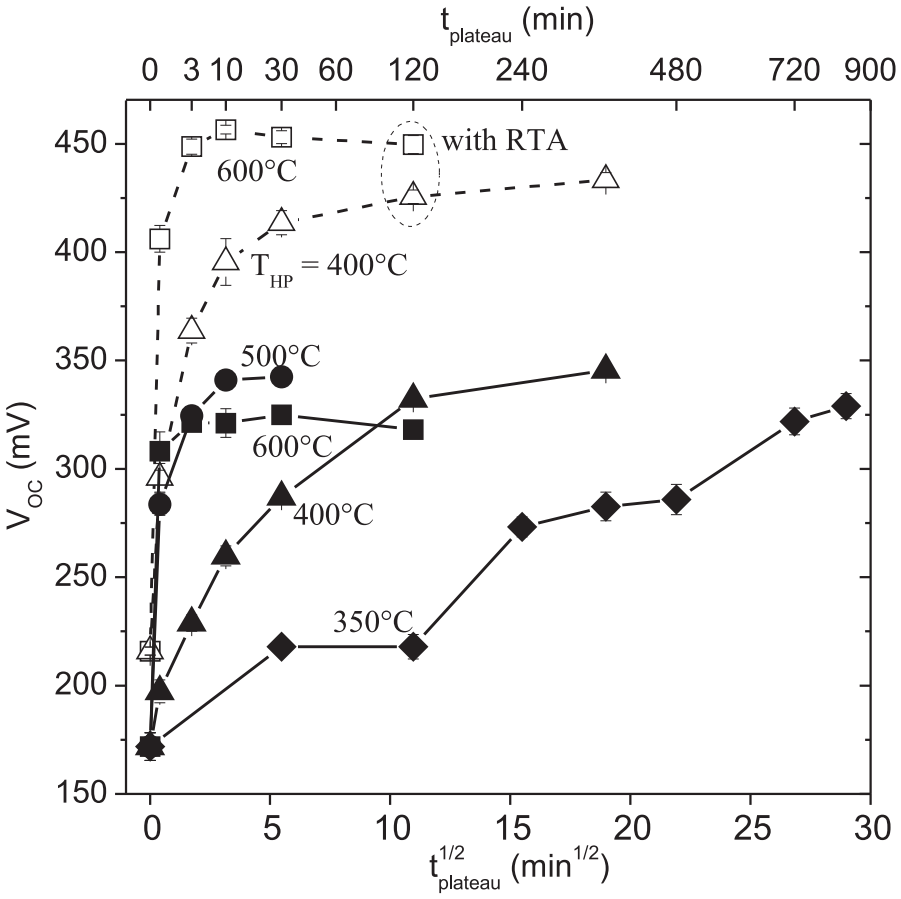

Figure 6.1: Open circuit voltages of poly-Si solar cells passivated at different temperatures of T_{HP} = 350°C, 400°C, 500°C and 600°C plotted versus the square root of the passivation plateau time $t_{plateau}$. The samples did not receive any RTA treatment (solid symbols). For comparison two samples from Fig. 5.1 are shown again, that received RTA (open symbols).

compared to RTA treated samples and the influence of RTA on the dynamics of HP is studied. In the second part, the RTA treatment is varied to see the effect on solar cell performance (V_{OC}) before and after a subsequent hydrogen treatment. If not stated otherwise, hydrogen passivation was performed at T_{HP} = 600°C for $t_{plateau}$ = 10 min.

6.1.1 Influence of Defect Annealing on the Dynamics of HP

The time and temperature dynamic of the hydrogen treatment has already been investigated for solar cell structures that received an RTA treatment by CSG Solar AG (chapter 5). In addition the same experiments were conducted with samples that had not received any RTA treatment. Fig. 6.1 shows the open circuit voltage of poly-Si solar cells passivated at different temperatures

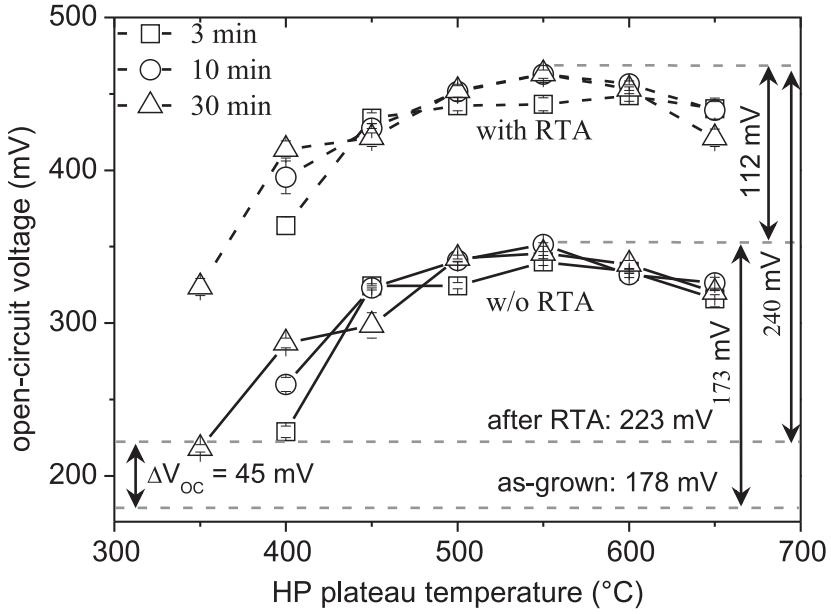

Figure 6.2: Open circuit voltages of poly-Si solar cells, passivated for different plateau time periods ($t_{plateau}$ =3, 10 and 30 min) and plotted over the passivation temperature T_{HP}. In addition also the initial values of V_{OC} before (178 mV) and after RTA (223 mV) are given.

of T_{HP} = 350°C, 400°C, 500°C and 600°C, plotted versus the square root of the passivation plateau time $t_{plateau}$. The samples did not receive any RTA treatment. For comparison two samples from Fig. 5.1 (Chapter 5) are shown again, that did receive an RTA treatment. The samples without RTA treatment (solid symbols, Fig. 6.1) show a similar time and temperature dependence than the samples that received an RTA treatment (open symbols in Fig. 6.1). Lower substrate temperatures T_{HP} result in a slower improvement and saturation of V_{OC}. This is expected due to a slower H diffusion with decreasing temperature.

However, the highest values of V_{OC} that are reached after HP without RTA are evidently lower than in case of an additional RTA treatment. The gap in V_{OC} also cannot be compensated by a longer hydrogen treatment (as evidenced in Fig. 6.1). Fig. 6.2 compares the open circuit voltages of RTA and non-RTA treated samples after HP as a function of passivation temperature T_{HP} for different plateau time periods ($t_{plateau}$ =3, 10 and 30 min). The dashed line represents samples that received a standard RTA treatment (already shown in Fig. 5.4 on page 64), whereas the other samples (solid line) did not receive any RTA treatment. In addition also the initial values of V_{OC} before (178 mV) and after RTA (but without HP) (V_{OC} = 223 mV) are given.

The samples without RTA treatment exhibit a similar temperature depen-

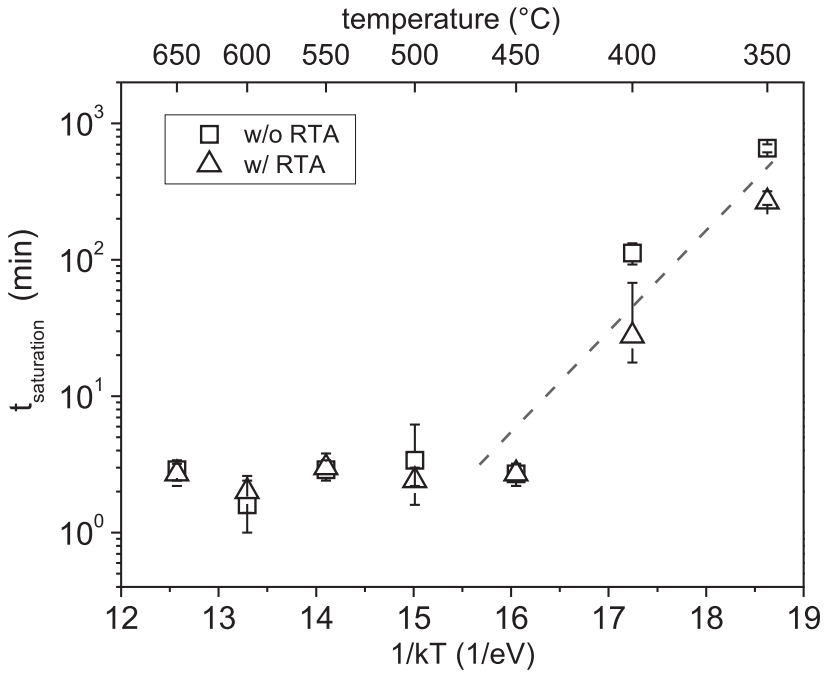

Figure 6.3: Saturation time, plotted logarithmical versus the inverse hydrogen treatment temperature (in units of 1/eV), shown for RTA treated samples (triangles, from Fig. 5.3) and for samples without RTA treatment (squares). The upper x-axis displays the equivalent temperature T_{HP}. The dashed line is guide to the eye.

dence. It shows the same shape and also features an optimum in terms of V_{OC} at the same temperature $T_{HP} = 550$°C, compared to RTA treated samples. Without RTA a best V_{OC} of 351 ± 1 mV is reached after HP at 550°C, compared to 463 ± 3 mV with an additional RTA treatment. In all cases the difference in V_{OC} between RTA and non-RTA treated samples is roughly ≥ 100 mV after HP, whereas initially only a difference of ~45 mV was observed.

The time dependence can be analyzed analogously as previously (chapter 5) by evaluating the time required to reach 95 % of the maximum V_{OC} for each temperature series (as illustrated in Fig 5.2). The saturation time $t_{saturation}$ is plotted logarithmically in an Arrhenius plot versus the inverse plateau temperature T_{HP} (in units of 1/eV) of the hydrogen treatment in Fig. 6.3. The equivalent temperatures are displayed in the upper x-axis. The saturation time $t_{saturation}$ is given for RTA treated samples (triangles, taken from Fig. 5.3) and for the samples without any RTA treatment (squares). It can be observed that both types of samples show a similar passivation dynamic, i.e. they show a similar saturation behavior, which relates to the hydrogen diffusion. Higher temperatures lead to shorter process times, which are reduced by two orders of magnitude, going from 350°C to 450°C. It appears that an RTA treatment does

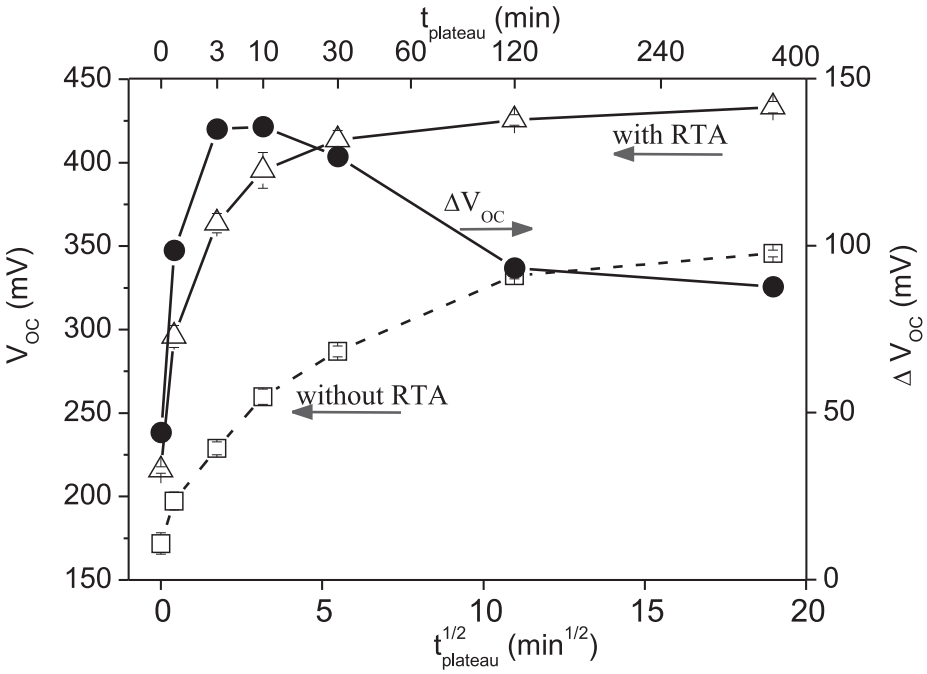

Figure 6.4: Comparison of V_{OC} for RTA (triangles) and non-RTA treated solar cells (squares), passivated at $T_{HP} = 400$°C and plotted versus the square root of the passivation plateau time $t_{plateau}$. The difference in V_{OC} is given on the right hand scale ($\triangle V_{OC}$, circles).

not noticeably show any influence on the temperature dependence of HP and H diffusion. However, RTA enhances the final effect of HP by about ≥ 100 mV, which seemingly is independent on T_{HP}.

Fig. 6.4 shows a comparison of the V_{OC} for RTA (triangles) and non-RTA treated solar cells (squares) that were passivated at $T_{HP} = 400$°C for different passivation plateau times $t_{plateau}$. At this low temperature the effect of HP occurs at a slow pace and improvement of V_{OC} can be observed closely. The difference in V_{OC} between both samples is given on the right hand side ($\triangle V_{OC}$, circles). Especially during the first 10 minutes of passivation $\triangle V_{OC}$ enlarges between RTA and non-RTA treated samples. Already after a passivation time of 1 min, the difference in V_{OC} is about 100 mV. Considering the diffusion coefficients determined in Fig. 6.3, after 1 min H will have diffused into the layer only at a depth of around 300 nm at 400°C. So the gap between RTA and non-RTA treated samples already opens up when H starts to diffuse through the highly doped p^+ layer (~50 nm) and reaches the absorber layer. After the saturation of the H treatment usually a difference of more than 100 mV was observed (see Fig. 6.2).

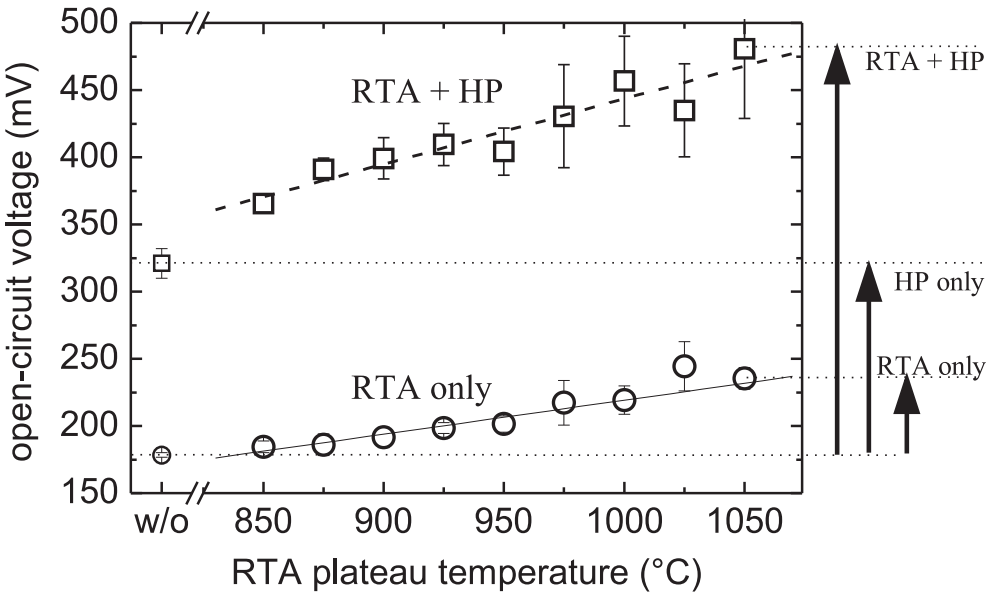

Figure 6.5: Open circuit voltage of RTA treated samples before (circles) and after HP (squares), plotted as a function of RTA plateau temperature (with fixed $t_{RTA} =$ 200 s). For comparison V_{OC} values for the samples without an RTA treatment are also given (w/o). The arrows to the right refer to the maximum change observed for each treatment.

The comparison of the results for RTA and non-RTA treated samples leads to the conclusion that RTA does not affect the dynamics of the HP treatment noticeably. Yet for the investigated samples the standard RTA, done at CSG Solar has a beneficial effect on the V_{OC}. The enhancement in V_{OC} due to RTA is less pronounced directly after RTA ($\Delta V_{OC} \approx 50$ mV) and more distinct after an additional HP ($\Delta V_{OC} \geq 100$ mV).

6.1.2 Variation of Defect Annealing

So far samples have been investigated that either received a standard RTA treatment or no RTA prior to HP. It was observed that RTA can strongly influence the final device performance. Therefore RTA treatments at different temperatures were performed and the effect of an RTA variation was studied before and after HP.

Fig. 6.5 shows the open circuit voltage of RTA treated samples before (circles) and after HP (squares), plotted as a function of RTA plateau temperature. RTA was conducted as described in Sec. 3.1.3 with a treatment plateau time of $t_{RTA} = 200$ s. Plasma hydrogenation was performed at 600°C for 10 min (Sec. 3.1.4). For comparison the V_{OC} of the samples without an RTA treatment is

also given (w/o). The arrows on the right hand side refer to the maximum change observed for each treatment. As-crystallized, the samples exhibit a V_{OC} of 178 ± 2 mV, which is improved to 321 ± 11 mV by HP (in both cases without RTA). As a trend V_{OC} improves continuously with higher applied RTA temperatures. The same trend can be observed after an additional HP step. The gradient of the linear fit amounts to 30 ± 3 mV/100K after RTA and 49 ± 7 mV/100K after HP. The improvement by higher RTA temperatures thus is enhanced after HP.

One interesting aspect can be elucidated for an RTA treatment of 850°C. Almost no effect can be observed directly after RTA ($V_{OC} = 184 \pm 6$ mV). Nevertheless, a strong increase can be evidenced after an additional HP (365 mV). Compared to a non-RTA treated sample (321 mV), an enhancement of 44 mV can be observed. For higher RTA temperatures this effect is augmented. This is indicated by the arrows in Fig. 6.5 in case of the best V_{OC}, achieved at $T_{RTA} = 1050$°C. By RTA, V_{OC} increases by 57 mV to $V_{OC} = 235 \pm 8$ mV. HP after RTA results in $V_{OC} = 481 \pm 52$ mV, which represents an improvement by 246 mV compared to no HP treatment.

This illustrates that when studying RTA as a treatment for defect annealing, the effects need to be always investigated along with HP. If adapted well, the effect of HP can be enhanced by an adequate RTA treatment and vice versa. On the other hand a further improvement by RTA does not necessarily implicate the same tendency after HP. This effect was observed for interval RTA experiments, where in some cases after HP a different trend was found than directly after RTA [154]. Hence it is required not to solely investigate RTA but always in combination with HP, in order to optimize the process and maximize device performance. In addition RTA at very high temperatures or long durations can lead to softening and bending of the substrate. This means that the RTA plateau temperature cannot be raised arbitrarily high, as bending will lead to inhomogeneities and problems during further device processing.

6.2 Passivation of Poly-Si Films with Different Structural Properties

In this section, new samples with varying structural properties will be processed by electron beam evaporation (EBE). The material properties of these layers can be varied by tuning the substrate temperature during Si deposition

(T_{dep}) in the temperature range of $T_{dep} = 200 - 700$°C. The influence of the deposition temperature T_{dep} on material properties will be characterized in the first part of this section by Raman measurements and scanning electron microscopy (SEM). In the second part, the interplay between material properties and hydrogen passivation will be investigated in terms of defect passivation of Si dangling bonds. In the last two parts of this section, solar cell structures will be fabricated and the influence of material properties on V_{OC} of the solar cell structures is tested before and after hydrogen passivation and RTA, respectively.

Different substrates have been used. Bare Corning 1737 and Borofloatt®33 glasses are suited substrates that can withstand the high temperature annealing steps, applied for example in case of an RTA treatment. Nevertheless, in some cases in-diffusion of contaminants from the glass into the poly-Si film was observed after RTA at high temperatures. In order to prevent contaminations during a high temperature step, the glass substrates can be coated with a SiN film, where the coating serves as anti-reflection layer and as a diffusion barrier for contaminants originating from the glass. In addition, Si wafers (here Si(100)) covered with a 150 nm thick thermal Si oxide were used as ideal reference substrates (SiO_x), impeding contamination originating from the substrate. The oxide on top gives an amorphous structure similar to the glass and prevents epitaxial growth (which is in this case undesired).

6.2.1 Structural Properties After Electron Beam Evaporation and Crystallization

This subsection investigates the influence of the deposition temperature T_{dep} on material properties by Raman measurements and scanning electron microscopy (SEM). Absorber layers were deposited by EBE in the temperature range of $T_{dep} = 200 - 600$°C onto plain Corning 1737 substrates and within $T_{dep} = 200 - 700$°C onto Si(100) wafers covered with a 150 nm thick Si oxide (SiO_x), respectively. After deposition all films subsequently underwent a thermal annealing step at 600°C. If not stated otherwise, Si films on Corning substrates were annealed for 8 h. Si films, deposited on the other substrates were annealed for 12 h. A temperature step of 12 h is sufficient for all samples to completely crystallize via solid phase crystallization (SPC). We will refer to this step as SPC, even if some of the films are crystalline already before the annealing step.

Figure 6.6 shows the Raman spectra of 1 µm thick Si films, deposited be-

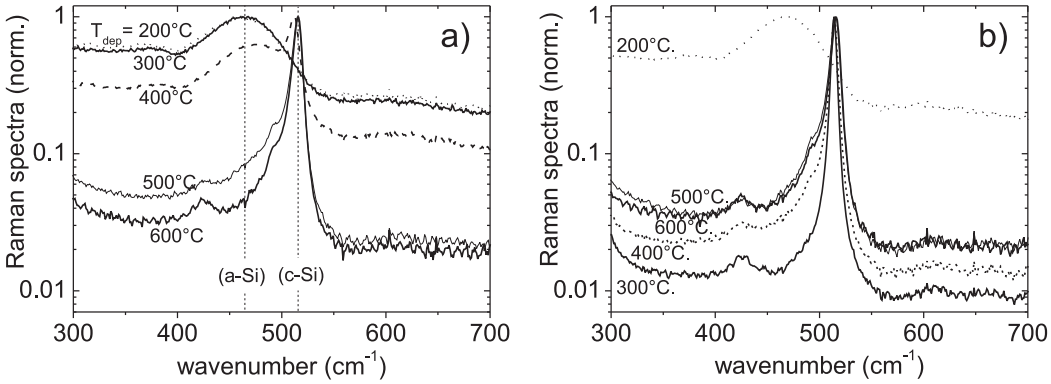

Figure 6.6: Raman spectra for samples, deposited between 200°C - 600°C onto Corning glass substrates, shown before (a) and after (b) annealing (SPC at 600°C for 8 h).

tween 200°C - 600°C onto Corning glass substrates. The spectra were measured before (a) and after the SPC step (b). Here SPC was only carried out for 8 h. In the as-grown case (a), samples deposited at $T_{dep} \leq 400$°C exhibit a broad peak at 480 cm^{-1}, which is characteristic for amorphous Si. Samples, deposited at $T_{dep} \geq 500$°C on the other hand exhibit an intense peak at 515 cm^{-1}. This peak is characteristic for the TO-LO phonon mode of crystalline Si. No amorphous contributions are observed, indicating a direct crystalline growth. In addition, the spectra exhibits an inhomogeneous broadening, which can be described with a smaller second peak, located at around 495 - 500 cm^{-1}. This inhomogeneous broadening is typically observed in small-grained microcrystalline material [119, 120].

The peak position at 515 cm^{-1} is slightly redshifted towards lower wavenumbers compared to the peak position of the TO-LO phonon mode at 520 cm^{-1}, measured for a reference Si(100) wafer. A redshift (negative $\triangle\omega$) of the Raman frequency indicates tensile strain, while a blueshift indicates compressive strain [118]. The tensile strain probably originates from the different thermal expansion coefficients of the glass and the thin Si films. It shall be noted that 2 µm thick films did not exhibit a strong redshift.

For the as-deposited samples the transition between amorphous to crystalline growth occurs around 400°C. At $T_{dep} = 400$°C both, amorphous and crystalline Raman contributions at 480 and 515 cm^{-1} were observed, whereas for $T_{dep} \leq 350$°C only amorphous and for $T_{dep} \geq 500$°C only crystalline contributions were evidenced.

After SPC (b), Raman spectra of samples, deposited at 300°C and 400°C

have altered significantly. No Raman contributions of a-Si at 480 cm^{-1} are detected. The samples show an intense peak at 515 cm^{-1} indicating complete solid phase crystallization. The spectra of the sample, deposited at 200°C remains unchanged. The Si film is still amorphous. Repetition of the experiment with a duration of 12h SPC resulted in complete crystallization. Therefore for the following experiments on SiO_x and SiN substrates a duration of 12h was chosen.

The Raman spectrum of the sample deposited at 600°C remains unchanged after annealing (b). This is expected because the films have been deposited directly crystalline. The crystalline structure is not affected by the thermal treatment. In the following, $T_{dep} \geq 500$°C will be referred to as the direct growth regime in contrast to the SPC regime, defined by $T_{dep} < 400$°C and the transition regime around $T_{dep} \approx 400$°C.

In Fig. 6.6 b) it can be seen that the crystalline peak is narrower for the sample, deposited at 300°C than for $T_{dep} = 600$°C. The crystalline peak width was evaluated further. In a first step a baseline was subtracted from the spectra. Next the full-width at half-maximum (FWHM) of the main peak (at ~515-520 cm^{-1}) was extracted by fitting the spectra with a Lorentzian profile. Due to the inhomogeneous broadening a second Lorentzian at ~ 495 cm^{-1} has been added in those cases.

Figure 6.7 shows the extracted FWHM of the crystalline Raman peak (after SPC), as a function of deposition temperature for the different samples on Corning substrates. Two more samples (with $T_{dep} = 250$°C, 350°C and SPC for 12 h) have been added. In addition the FWHM of 2 µm thick poly-Si films, deposited onto Si(100) wafers covered with a 150 nm thick Si oxide, is given after the SPC step. The fraction of the Raman signal, originating from the substrate can be neglected. The film thickness of 2 µm is close to the penetration depth of the laser (~3 µm). In addition the remaining intensity of the laser beam will partially also be reflected at the poly-Si/Si-oxide interface. The signal of the Si wafer will thus only have a minor influence, which would lead to a slight underestimation of the FWHM.

As can be seen, the dependence on T_{dep} is very similar for both substrates. The width increases strongly for samples with $T_{dep} \geq 400$°C. The largest width can be evidenced at $T_{dep} = 500$°C. For 600°C and even more pronounced for 700°C it decreases again. Smaller FWHM values are observed for deposition temperatures below 400°C. Note that this temperature regime is characterized by the deposition of initially amorphous films and subsequent SPC. The lowest

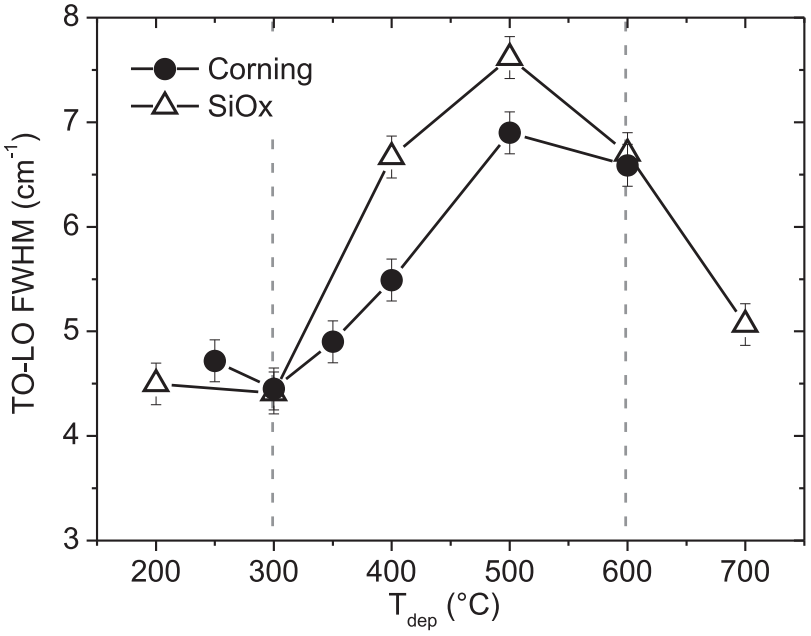

Figure 6.7: Raman FWHM of the crystalline TO-LO Si phonon mode (after SPC), plotted over the deposition temperature T_{dep}. Circles represent Si films deposited onto Corning substrates and triangles Si(100) wafer substrates, covered with a 150 nm thick Si oxide

values are obtained at $T_{dep} = 300$°C. For both substrates the crystallized films exhibit FWHM of 4.4 ± 0.2 cm^{-1}. The FWHM of a reference Si(100) wafer was determined to be 3.1 ± 0.2 cm^{-1}. In case of SiO_x substrates the FWHM remains almost unchanged for $T_{dep} = 300$°C and $T_{dep} = 200$°C. In case of Corning the minimum is more pronounced. The broadening of the FWHM can be related to structural defects that destroy the lattice translational symmetry and relaxes the momentum conservation rule during phonon-photon scattering [120]. A narrower width can be taken as an indication for larger grains and less structural defects.

This was verified by scanning electron microscopy (SEM) and electron beam scattering diffraction (EBSD). Large grains were observed for the films deposited at $T_{dep} \leq 350$°C (SPC regime). Fig. 6.8 shows the SEM images of the samples after SPC, deposited at different temperatures onto Corning substrates. The insets for $T_{dep} = 500$°C and 600°C are magnifications to make the grain structure more visible. The regime for $T_{dep} \leq 350$°C is characterized by the deposition of a-Si and a subsequent SPC resulting in large grains with sizes of 1 - 3 µm. For $T_{dep} \geq 500$°C the films are deposited completely crystalline (direct growth regime) and the grains grow in a columnar structure with a

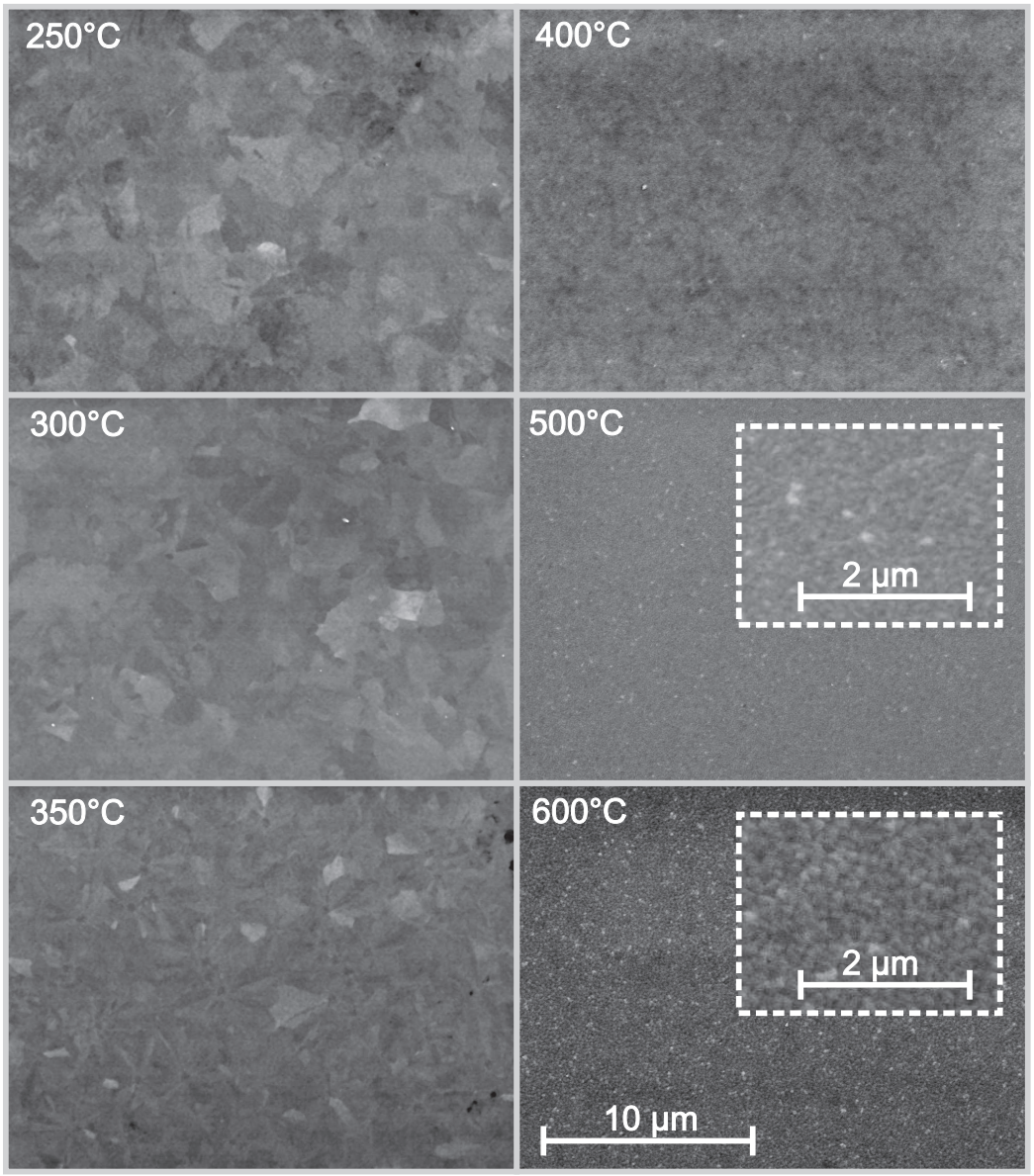

Figure 6.8: Scanning electron microscopy (SEM) of Si films after SPC, deposited at different temperatures onto Corning substrates. The insets for T_{dep} = 500 and 600°C are magnifications with the given scale.

much smaller grain size in the order of 100 nm. At $T_{dep} \sim 400$°C a transition from amorphous to crystalline growth takes place. After SPC the films grown at 400°C and 500°C seem to feature the smallest grains. Within the direct growth regime, higher deposition temperatures will lead to an enhancement of the Si adatom mobility during growth and result in larger grains and less structural defects. This can explain the sharp decline of FWHM, observed for $T_{dep} \geq 600$°C. A grain size of 100 nm is to small to be visible in our EBSD setup and was therefore only roughly estimated from SEM images.

6.2.2 Hydrogen Passivation of Defects (Si dangling bonds)

In the preceding, the influence of deposition temperature T_{dep} on crystalline properties was investigated. Raman and SEM measurements indicate that a deposition temperature of $T_{dep} = 300$°C should be favorable for structural high quality material. In a next step a connection is established between the structural properties of the films, the defect concentration and the passivation of those defects. Hydrogen passivation was performed at $T_{HP} = 600$°C for $t_{plateau} = 10$ min.

The most prominent defects in poly-Si are Si dangling bonds originating from under-coordinated Si atoms. This results in an unpaired electron of the Si dangling bond whose energy level moves into the band gap. Si dangling bonds are paramagnetic and can be detected by ESR measurements.

The typical ESR absorption spectrum of intentionally undoped Si samples, is shown in the inset of Fig. 6.9. The measurements are carried out under modulation of the magnetic field and the spectrum thus represents the derivative of the absorption. The shape of the plotted absorption spectrum is typical for Si dangling bonds with a g-value of 2.0055 ($\pm$ 0.0005).

The choice of substrate is important for ESR measurements. Bare Corning 1737 substrates did not show any ESR signal that would distort the measurement. Hence, Corning 1737 glass substrates are suited for ESR measurements. On the other hand, to investigate the influence of RTA requires a SiN coating, used as a diffusion barrier to prevent indiffusion of contaminants from the glass. Unfortunately SiN coated glass substrates are unsuited for ESR measurements. This is because plasma-deposited amorphous SiN:H exhibits a similar absorption spectrum with the same g-value of 2.0055 than the Si dangling bond in amorphous Si [155] (also observed in our case). Therefore only bare Corning 1737 substrates were used and RTA was not investigated by ESR.

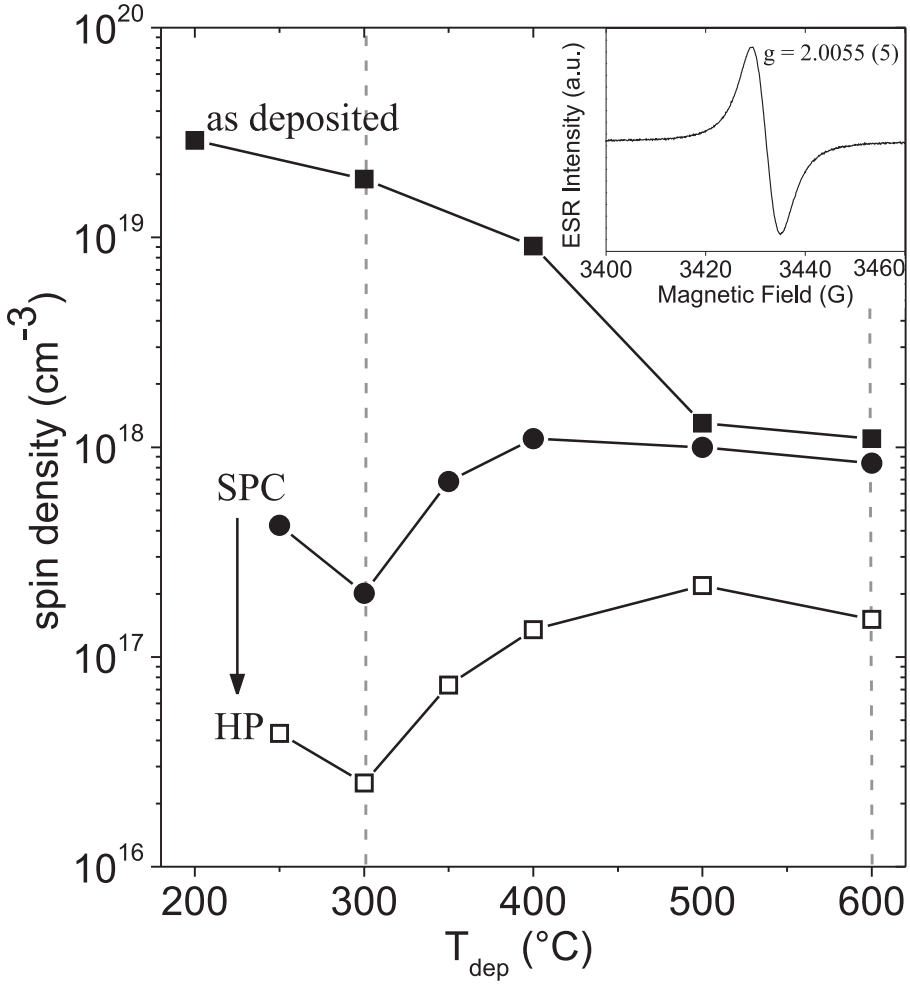

Figure 6.9: Si dangling bond concentration (measured by ESR) as a function of deposition temperature T_{dep}, directly after deposition, after SPC and after hydrogen passivation (HP). The Si films were deposited onto Corning substrates. The inset shows the ESR spectrum of one of the samples.

From the intensity of the measured ESR absorption, the Si dangling bond concentration [db] can be extracted and is plotted in Fig. 6.9 versus T_{dep}. For low deposition temperatures $T_{dep} \leq 400$°C, the as-deposited samples (solid squares) are still amorphous and exhibit a high number of dangling bonds in the order of 10^{19} cm^{-3}, typical for non-hydrogenated a-Si. Near the transition from a-Si to direct-grown c-Si at around 400 °C the [db] decreases and goes down to roughly $1 \cdot 10^{18}$ cm^{-3} for the samples, deposited at $T_{dep} \geq 500$°C (direct growth regime).

After the SPC annealing step (solid circles), the [db] of the samples with $T_{dep} = 500$°C and 600°C remains almost unaffected by the thermal treatment. This is expected because those samples have been already crystalline before the

annealing step and no structural change occurred. Thus also the [db] remains unaffected. On the other hand for $T_{dep} \leq 400$°C, the [db] is affected strongly by the SPC annealing step. The [db] is lower for the SPC regime than for the direct-growth regime. This is in agreement with observations made by Raman and SEM. The temperature dependence of [db] shows a very similar trend as the FWHM in Fig. 6.7 with a minimum at $T_{dep} = 300$°C for the large-grained material.

After the annealing step (SPC), the samples received a hydrogen treatment. The standard hydrogen treatment at $T_{HP} = 600$°C was applied for 10 min, as described in Sec. 3.1.4. The results of the [db] after HP (open squares) can be seen in Fig. 6.9. The hydrogen treatment strongly reduces the [db] in all cases. In the investigated range, the [db] is decreased independently of the deposition temperature for all the samples by about one order of magnitude. The overall trend of the [db] vs. deposition temperature thus remains the same. The dangling bond density, observed after HP, depends strongly on the initial concentration. The minimum in [db] before and after HP is observed for the same deposition temperature of $T_{dep} = 300$°C. After HP, the [db] is lowered from $2.0 \cdot 10^{17}$ cm^{-3} to $2.5 \cdot 10^{16}$ cm^{-3} for $T_{dep} = 300$°C.

Except for the films, deposited at $T_{dep} = 250$°C and 350°C, the thickness of the samples in Fig. 6.9 is 1 µm. To resolve the minimum, the experiments were repeated for $T_{dep} = 250$°C, 300 °C and 350°C, this time with a film thickness of 2 µm to give better ESR spectra. The value of the dangling bond concentration for $T_{dep} = 300$°C was reproduced and no dependence of film thickness was observed. Note that for a 1 µm thick film, a dangling bond concentration of $2.5 \cdot 10^{16}$ cm^{-3} corresponds to an absolute number of $1 \cdot 10^{12}$ spins (sample size = 0.4 cm^2). This is already very close to the detection limit of the ESR setup ($1 \cdot 10^{11} - 5 \cdot 10^{11}$ spins). If converted to an areal density (i.e. $2.5 \cdot 10^{12}$ cm^{-2}), it is in the same range as a typical surface density of states of $1 \cdot 10^{12}$ cm^{-2}. This means that dangling bonds from the surface might play a role under those conditions and cannot be distinguished from bulk dangling bonds.

6.2.3 Hydrogen Passivation of Solar Cells with Different Structural Properties

After characterizing the passivation of Si dangling bond defects, this section will focus on the passivation of complete solar cell structures and the influence of material properties. Complete solar cell structures were fabricated as

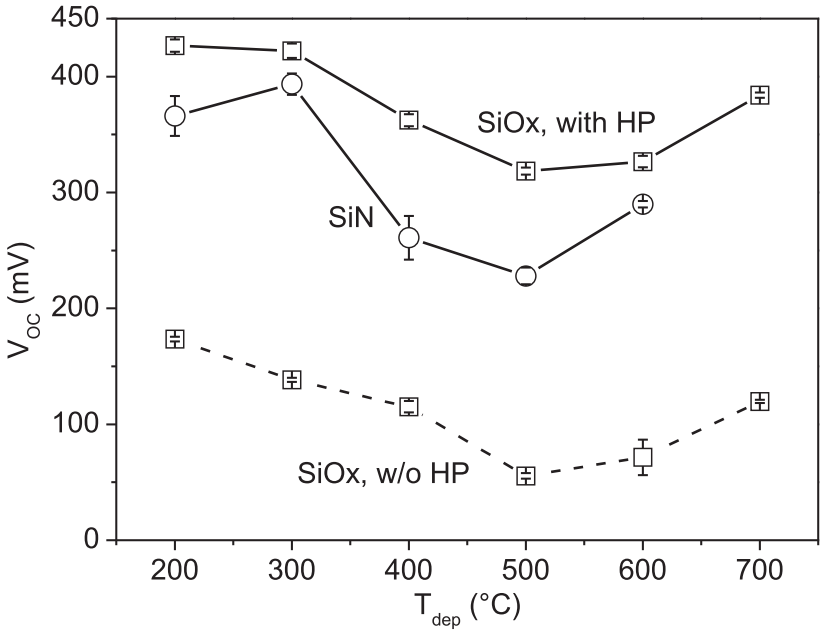

Figure 6.10: Open circuit voltage V_{OC} of RTA treated solar cell structures with the absorber and BSF being deposited by electron beam evaporation. The different substrates (SiN coated Borofloat and Si(100) wafer with SiO_x layer) are indicated. The V_{OC} is plotted as a function of the absorber and BSF deposition temperature T_{dep} and given before (for SiO_x) and after HP (for SiN, SiO_x).

described in Sec. 3.1.2. For the solar cells presented in this chapter an RTA treatment at 1000°C for 60 s was carried out. Plain glass substrates such as Corning or Borofloat are not suited for such a high temperature annealing step. They contain numerous elements that can diffuse into the Si layer during the RTA step and are a potential source of contamination. Therefore a SiN coating was used (Sec. 3.1.2) that can serve as a diffusion barrier. In addition, thermally oxidized Si wafers (SiO_x) have been used as reference substrates.

First, the emitter was deposited by PE-CVD onto the substrate (for details see section 3.1.2). The absorber and BSF were deposited in the same run by EBE. RTA and HP were carried out after the SPC step. Hydrogen passivation was performed at $T_{HP} = 600$°C for $t_{plateau} = 10$ min. The deposition of absorber and BSF was done through a shadow mask. This way the emitter could be easily contacted to measure the photovoltage under open circuit conditions (V_{OC}) after each post-deposition treatment by Suns-Voc.

Fig. 6.10 shows the 1-sun V_{OC} of RTA treated solar cell structures plotted as a function of absorber and BSF deposition temperature T_{dep}. The used substrates (circles: SiN coated Borofloat, squares: thermally oxidized Si wafers (SiO_x)) are indicated. In case of the SiO_x substrates the V_{OC} is shown before

(dashed line) and after HP (solid line). In case of SiN coating, only the V_{OC} after HP was measured.

Before HP, highest V_{OC} values are obtained within the temperature range of $T_{dep} = 200 - 300$°C where the films exhibit the largest grains. Yet V_{OC} is limited to below 200 mV. With higher deposition temperatures V_{OC} diminishes and shows a minimum at $T_{dep} = 500$°C. Above 500°C, V_{OC} improves again. HP results in a large improvement in V_{OC} of more than 250 mV. After passivation the shape of the curve is maintained, i.e. highest values are found for samples with $T_{dep} = 200 - 300$°C and a minimum for $T_{dep} = 500$°C. The best V_{OC} is achieved within the SPC regime at 200°C with 427 ± 5 mV (422 ± 6 mV for 300°C). $T_{dep} = 500$°C results in $V_{OC} = 318 \pm 3$ mV, which is a difference of more than 100 mV. The temperature dependence of V_{OC} for the poly-Si films deposited onto the two different substrates (SiN and SiO_x) is similar. However, in case of SiN the open circuit voltages are slightly lower with the highest value of 394 ± 9 mV for $T_{dep} = 300$°C.

6.2.4 Interplay of Defect Annealing with Passivation and Structural Properties

In the following, the impact of RTA and its interplay with material properties and HP will be studied, together with hydrogen passivation. Therefore, poly-Si solar cell structures were fabricated onto thermally oxidized Si wafers (SiO_x). The RTA treatment was carried out at 1000°C for 60s. Hydrogen passivation was performed at $T_{HP} = 600$°C for $t_{plateau} = 10$ min. As demonstrated in the previous section, depending on the deposition temperature the poly-Si films exhibit different material properties. Within the SPC regime ($T_{dep} < 400$°C) the poly-Si films feature large grains with an average grain size of ~ 3 µm. For the direct growth regime ($T_{dep} > 400$°C), small grains in the order of 100 nm are observed.

Fig. 6.11 a) and b) shows the V_{OC} and pseudo fillfactor of the solar cell structures, respectively - plotted over the deposition temperature T_{dep} for four different cases (post-deposition treatments). In all cases (a-d) a thermal annealing at 600°C (SPC for the a-Si samples) was applied (described in Sec. 3.1.1). The samples that did not receive any further post-deposition treatments are labeled with (a). The other samples in Fig. 6.11 received either only RTA (b) or only HP (c) or they received the combination of RTA and HP (d).

After SPC (case (a)) all samples independently of the deposition temper-

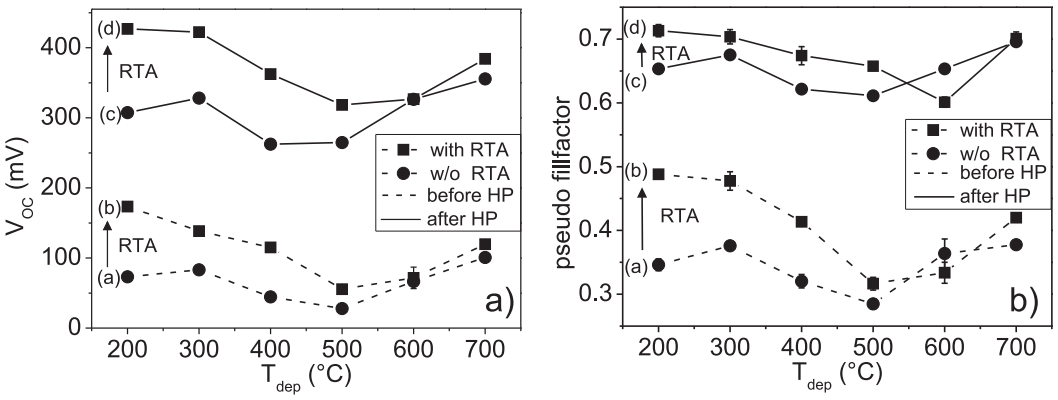

Figure 6.11: Open circuit voltage and pseudo fillfactor of solar cell structures, with the absorber and BSF deposited by electron beam evaporation, as a function of the deposition temperature T_{dep} and shown after different post-deposition treatments: in all case a thermal annealing at 600°C (SPC) was applied (a-d), a) without any additional treatment, b) after RTA, c) after HP and d) after the combination of RTA and HP

ature T_{dep} exhibit a very poor V_{OC} with the best V_{OC} of 100 mV for T_{dep} = 700°C. Without the RTA treatment (case a & c), the V_{OC} in the direct growth regime (T_{dep} = 600°C and 700°C) is equal or higher than in the SPC regime.

The opposite trend is revealed with an additional RTA treatment (case b & c). An RTA treatment improves the V_{OC} in the SPC regime but has no major influence on the V_{OC} of the samples from the direct growth regime. After RTA the best V_{OC}'s are observed for the samples deposited at 200°C and 300°C. In all cases (a-d) a minimum in V_{OC} can be observed within the temperature range of 400°C to 500°C which corresponds to the transition regime between SPC and direct growth.

Without HP the open circuit voltage is limited to below 200 mV. HP results in a large improvement in V_{OC} by about 250 mV (solid lines). This holds true for all samples, independent of deposition temperature T_{dep} and an additional RTA treatment. Also the shape of the curve is preserved.

For completeness the corresponding pseudo-fillfactors pFF, extracted from Suns-Voc measurements, are shown in Fig. 6.11 b). In all cases pFF shows a similar behavior as V_{OC}. An improvement in pFF by RTA (case (b) and (d)) is again only established for samples of lower deposition temperatures $\leq$ 400°C. For the direct growth regime, RTA shows no clear influence.

6.3 Discussion

Passivation of Defects in Poly-Si Films with Different Structural Properties

In Sec. 6.2 it was shown that the substrate temperature T_{dep} during the deposition of Si by EBE has a significant influence on the structure of the films. For $T_{dep} \leq 400$°C (SPC regime) the as-deposited films still exhibit an amorphous phase and for $T_{dep} < 400$°C large crystalline grains can be obtained by SPC. The grain size is equal or larger than the film thickness (1-2 µm). For $T_{dep} \geq 500$°C (direct-growth regime) the films grow crystalline in a small grained, columnar structure. Towards 700°C grain size increases again with increasing temperature due to more mobile Si adatoms during growth/deposition.

The grain size can be roughly estimated from SEM images of the samples (Fig. 6.8 on page 88). The average grain size was estimated to be 3 ± 1 µm and 0.2 ± 0.1 µm for films deposited at $T_{dep} = 300$°C and 600°C, respectively. The average grain size differs by more than one order of magnitude for those two samples. With the assumption that the Si dangling bond density at the grain boundary (areal, cm^{-2}) is constant and no intragrain defects are present, the [db] per volume should be proportional to $1/g$ for columnar grains with a grain size g. The [db] concentration after SPC for the large grained sample is only by a factor of 4.2 smaller (Fig. 6.9 on page 90). Normalized to the grain size, the defect concentration [db]/g is roughly by a factor of 2 larger for films with larger grains. This suggests that the defect density at the grain boundary is either not constant for the different samples but depends on the growth regime or that intragrain defects cannot be neglected. Although the sample at 300 °C exhibits larger grains, either the grain boundaries in this sample could be more disordered compared to the small grained material ($T_{dep} = 600$°C) or the large grained samples could exhibit more intragrain defects that add up to the total dangling bond concentration.

Intragrain defects of the poly-Si samples were studied by applying a defect etch (Secco [156]) to the films after SPC. Fig. 6.12 shows exemplarily SEM images of two etched samples, deposited at 300°C and 600°C, respectively. For the sample deposited at $T_{dep} = 300$°C, the surface of the grains is affected strongly by the etch process and a high number of holes can be observed. These holes can be related to intragrain defects in the form of dislocations. The grain size is larger than 1 µm. For the sample with $T_{dep} = 600$°C the

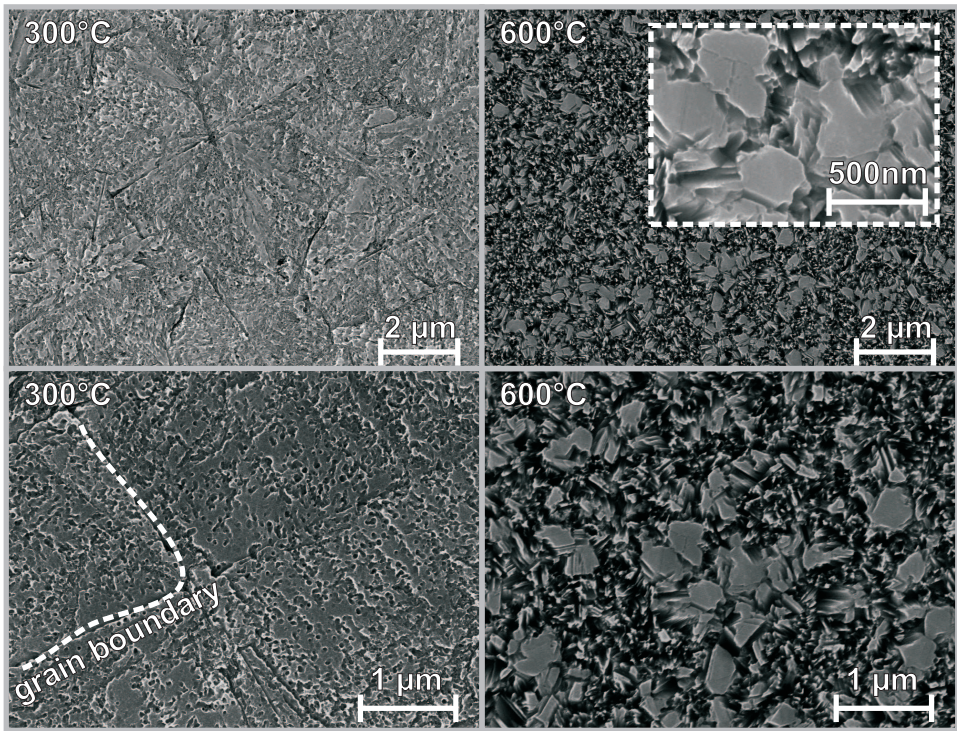

Figure 6.12: SEM images of two samples deposited at 300°C and 600°C, respectively. After SPC a defect etch was applied (Secco [156]). For the sample deposited at $T_{dep} = 300$°C a high number of intragrain defects in the form of dislocations can be observed. The grain size is larger than 1 µm. For $T_{dep} = 600$°C the smaller grains are strongly etched. No intragrain defects can be observed in the remaining grains.

smaller grains are etched strongly. Surprisingly the surface of the larger grains remains smooth and unaffected by the defect etch. No intragrain defects can be observed. This observation is characteristic for all the samples: intragrain defects have been observed for all samples deposited at $T_{dep} < 400$°C whereas for $T_{dep} > 400$°C no intragrain defects could be evidenced. The findings on intragrain defects for $T_{dep} < 400$°C and no intragrain defects in form of dislocations for $T_{dep} > 400$°C support the above argument that the large grained samples exhibit more intragrain defects that add up to the total dangling bond concentration.

The [db] can be strongly reduced by HP (as seen in Fig. 6.9 on page 90). In the investigated range, the [db] is decreased for all the samples by about one order of magnitude. The overall trend of the [db] vs. deposition temperature thus remains the same. The minimum in [db] before and after HP is observed for $T_{dep} = 300$°C which corresponds well to the minimum in FWHM of the crystalline TO-LO Si phonon peak, observed by Raman and coincides with the regime of largest grains. After HP, the [db] is lowered from $2.0 \cdot 10^{17}$ cm^{-3}

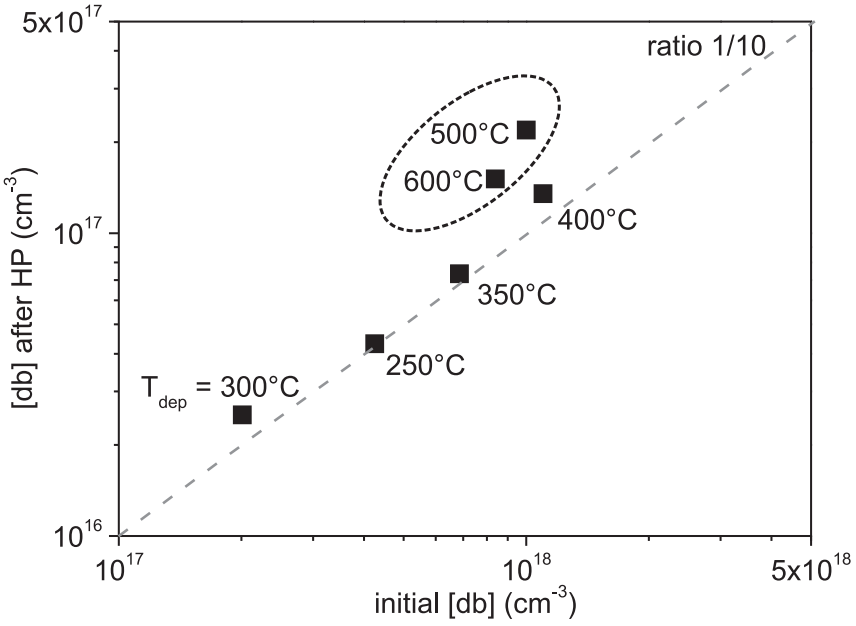

Figure 6.13: Si dangling bond concentration after HP as a function of initial dangling bond concentration (prior to HP). The dashed line represents a ratio of unpassivated dangling bonds of 1/10.

to $2.5 \cdot 10^{16}$ cm^{-3} for $T_{dep} = 300$°C.

The ratio of passivated dangling bonds is analyzed in Fig. 6.13. Here, the Si dangling bond concentration after HP is plotted as a function of initial dangling bond concentration (prior to HP). All the samples, deposited at $T_{dep} \leq 400$°C show a non-passivated to initial dangling bond ratio close to 1/10, which is represented by the dashed line. The dangling bond density, observed after HP, therefore depends strongly on the initial concentration. Defect passivation is slightly less efficient for the direct growth regime. Samples deposited at $T_{dep} =$ 500°C and 600°C (direct growth regime) show a lower ratio of $\sim$ 2/10. The difference by a factor of 2 could be related to the difference in the normalized defect concentration [db]/g.

Passivation of Poly-Si Solar Cells: Interplay with Defect Annealing and Structural Properties

This different behavior between SPC and direct growth regime is also reflected in the solar cell results (e.g. Fig. 6.11 on page 94). Without RTA the direct-growth regime with small grains gives equally high or even higher V_{OC} 's than the large grained material from the SPC regime. In principle the reverse effect would be expected, resulting in lower V_{OC}'s for the small grained material.

This was only evidenced after an additional RTA treatment, where the highest V_{OC} 's are obtained for the films with the largest grains, e.g. in the SPC regime.

Another observation made in Fig. 6.11 is the dependence of the RTA induced improvement on the deposition temperature T_{dep}. The improvements are depicted in Fig. 6.14 a) for the poly-Si solar cells, deposited by electron beam evaporation as a function of deposition temperature T_{dep}. The effect on $\triangle V_{OC}$ by RTA (circles) and HP (squares) is analyzed individually for improvements resulting from RTA directly after SPC (i.e. before HP, open circles)

$$\triangle V_{OC}^{RTA,SPC} = V_{OC}^{RTA} - V_{OC}^{SPC}$$

after HP (full circles)

$$\triangle V_{OC}^{RTA,HP} = V_{OC}^{RTA+HP} - V_{OC}^{HP}$$

and improvements achieved by HP excluding RTA (i.e. directly after SPC, open squares)

$$\triangle V_{OC}^{HP,SPC} = V_{OC}^{HP} - V_{OC}^{SPC}$$

and including RTA (full squares)

$$\triangle V_{OC}^{HP,RTA} = V_{OC}^{RTA+HP} - V_{OC}^{RTA}$$

respectively.

A larger effect of the RTA treatment in Fig. 6.14 a) can only be evidenced for deposition temperatures $T_{dep} \leq 400$°C. For the direct growth regime ($T_{dep} \geq 500$°C) the effect of RTA results is less than 30 mV in all but one case.

The improvement after hydrogen passivation is always large and does not show a strong dependence on the structural properties. Therefore poly-Si films with higher V_{OC} values before HP will also exhibit higher values after HP. $\triangle V_{OC}$ after HP can however be enhanced by an additional RTA treatment. Improvements by RTA and enhancement of the hydrogen treatment depend on the structural properties and are most significant within the SPC regime ($T_{dep} \leq 400$°C). The effect of passivation is slightly lower without RTA ($\triangle V_{OC} = 234 \pm 4$ mV) than with RTA ($\triangle V_{OC} = 262 \pm 6$ mV). The average change in V_{OC} of all samples after passivation amounts to $\triangle V_{OC} = 251 \pm 6$ mV.

In Fig. 6.14 a) RTA was performed at 1000°C for 60 s. Fig. 6.14 b) compares the results to improvements of PE-CVD grown poly-Si solar cells, achieved by

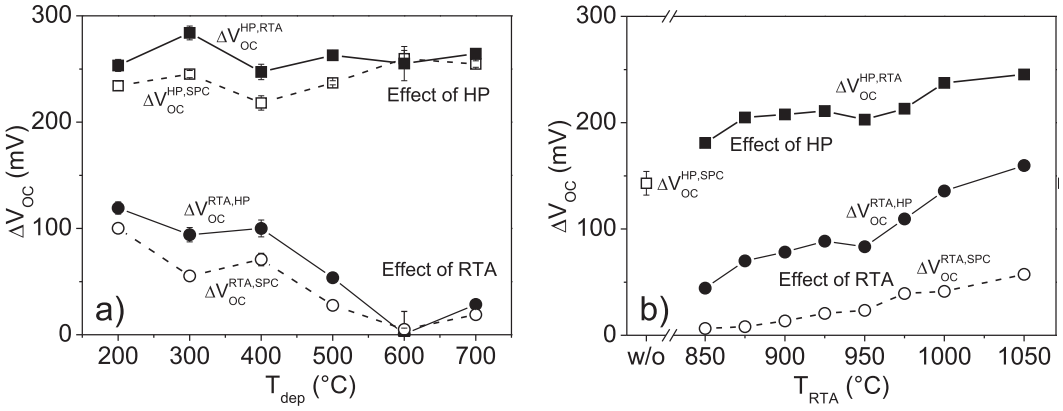

Figure 6.14: Effect of RTA and HP on $\triangle V_{OC}$ for poly-Si solar cells, deposited by a) electron beam evaporation, as a funtion of T_{dep} and b) PE-CVD, as a function of RTA plateau temperature T_{RTA} . The improvements are analyzed individually for improvements resulting from RTA directly after SPC (open circles: $\triangle V_{OC}^{RTA,SPC}$), after HP (full circles: $\triangle V_{OC}^{RTA,HP}$) and improvements achieved by HP directly after SPC (open squares: $\triangle V_{OC}^{HP,SPC}$) and after RTA (full squares: $\triangle V_{OC}^{HP,RTA}$), respectively.

RTA and HP as a function of RTA plateau temperature T_{RTA}. The RTA plateau time $t_{plateau}$ was 200 s. Improvements by RTA (circles) profit from high treatment temperatures T_{RTA}. Large improvements are observed only in conjunction with a subsequent hydrogen treatment. The multiplication of RTA and HP treatment is more pronounced for CVD than for EBE grown samples.

Variations in RTA have a major influence on V_{OC}. Higher annealing temperatures have resulted in higher V_{OC} directly after RTA. Together with HP this effect can be amplified. If adapted well, the effect of HP can be enhanced by an adequate RTA treatment and vice versa. An improvement by RTA does not necessarily implicate an improvement after HP, which was observed in recent experiments concerning RTA interval treatments [154]. Higher RTA treatment temperatures can for example lead to secondary effects like in-diffusion of contaminants and generation or reduction of stress. Those secondary effects could temporarily improve the device performance prior to an H treatment but lead to a deteriorated device after HP. When the V_{OC} was boosted by RTA, simultaneously also an enhanced scattering of V_{OC} was observed especially after HP (see Fig. 6.5 on page 82). This could be an indication for inhomogeneities that are caused by RTA but become visible only after an additional HP step. Therefore RTA always should be investigated together with HP.

The comparison of RTA and non-RTA treated poly-Si samples, grown by

CVD, has shown that both samples exhibit the same dynamics regarding hydrogen passivation. The calculated diffusion coefficients are of the same order of magnitude and feature the same temperature dependence (Fig. 6.3 on page 80). Hence RTA does not significantly affect the diffusion of hydrogen. Nevertheless, without RTA treatments V_{OC} is more than 100 mV lower (Fig. 6.2 on page 79). The best V_{OC} after HP is 351 mV compared to 463mV with an additional RTA treatment prior to HP.

This enhancement by RTA can be already observed at the beginning of the hydrogen treatment (Fig. 6.4) when H passes the BSF layer but most likely has not diffused completely through the absorber layer. This indicates that the effect is independent of bulk passivation but might be attributed to the highly boron doped BSF layer.

The objective of the RTA treatment is dopant activation. For poly-Si films, obtained by SPC of CVD grown a-Si, dopant activation is usually lower than unity. RTA can cause a better rearrangement and an activation of the dopants within the crystal lattice. Hydrogen passivation on the other hand is known to passivate shallow acceptors like boron, which was observed for p-type Si [69, 70, 71]. It could be speculated that RTA might result in a weaker passivation efficiency of the dopants by H and hence lead to higher open circuit voltages due to a better BSF. Yet this has not been tested so far. Experiments concerning dopant activation and dopant passivation could be carried out and investigated for example by Hall measurements.

As shown in the preceding, improvements by RTA of EBE deposited films depend on the structural properties. A significant improvement in V_{OC} can be observed for the SPC regime, whereas no significant change is seen for the direct growth regime. There are at least two reasons to consider: intragrain defects and dopant activation.

Dopant activation has been discussed before. It was shown by Dogan et al. that for poly-Si films, deposited epitaxially at 600°C by electron beam evaporation, complete doping activation could be achieved [14, 157]. Similar high activation can therefore be expected for the direct-growth regime. On the other hand, CVD grown a-Si show a dopant activation lower than unity after SPC. It is not clear so far, if a lower dopant activation is also given for poly-Si films of the SPC regime, deposited by EBE. If the poly-Si samples of the SPC regime exhibit lower dopant activation than samples of the direct growth regime, this would explain the observed RTA behavior for different regimes.

The other difference between the two regimes is the presence of intragrain

defects in large-grained poly-Si films of the SPC regime, whereas no intragrain defects were observed in films of the direct growth regime. It was shown that intragrain defects in poly-Si, fabricated by high-temperature epitaxy on poly-Si seed layers (obtained by aluminum induced crystallization) are highly electrically active and act as recombination centers [158]. To explain the RTA behavior, it would implement that the H treatment does not preferentially passivate dislocations within the grain compared to grain boundaries [159] unless RTA is applied. This however is in contradiction to the results on defect passivation of Si dangling bonds (without RTA, Fig. 6.9 and 6.13), stating that defect passivation is slightly less efficient for the direct growth regime and not for the SPC regime.

To summarize:

- By changing the deposition temperature it is possible to tune the material properties of the poly-Si films using electron beam evaporation: A minimum in Si dangling bond concentration is observed for $T_{dep} = 300°C$, which corresponds to the minimum in FWHM of the crystalline TO-LO Si phonon peak, observed by Raman and coincides with the regime of largest grains and highest V_{OC} values after RTA and HP.

- The Si dangling bond concentration can be strongly reduced by HP. Samples of the SPC regime show a non-passivated to initial dangling bond ratio close to 1/10. The dangling bond density, observed after HP, therefore depends strongly on the initial concentration. For $T_{dep} = 300°C$, the dangling bond concentration is lowered from $2.0 \cdot 10^{17}$ cm^{-3} to $2.5 \cdot 10^{16}$ cm^{-3} by HP.

- High open circuit voltages rely on good material properties, which are not necessarily manifested solely in grain size: Without an RTA treatment, the direct-growth regime with small grains gives equally high or even higher V_{OC} values than the large grained material from the SPC regime. RTA affects primarily samples of the SPC regime. Possible reasons include a larger amount of intragrain defects, observed in SPC material or a suggested lower dopant activation.

- After RTA and HP, open circuit voltages of 427 ± 5 mV have been obtained. Note that the fabrication of those samples has yet not been optimized in terms of thickness, doping and contacting. In addition no light trapping has been applied. Therefore further improvements can be

expected. The results have provided valuable insights into processing and post-deposition treatments of high quality poly-Si.

7 Discussion of Electronic Solar Cell Performance

Poly-Si exhibits a large number of defects, mainly located at grain boundaries. The presence of defects leads to recombination and affects the device performance. The aim of the hydrogen plasma treatment is to passivate those defects. Because HP is investigated in terms of its effect on the solar cell device performance (open-circuit voltage V_{OC}), a link will be established between defect recombination and minority carrier diffusion length L_{eff} on the one hand and device performance (i.e. V_{OC}) on the other hand. CVD grown poly-Si solar cells, investigated in this thesis, will be described within a two-diode model. A correlation between L_{eff} and V_{OC} can be given, following the model of Taretto et al. [160]. Without loss of generality a p-type absorber will be considered with holes as majority and electrons as minority carriers.

Modeling of Poly-Si Solar Cells by a Two Diode Model and an Effective Diffusion Length To further analyze the Suns-Voc data, obtained in this thesis, we want to apply the two-diode model, as described by Taretto et al. [160]. It will be applied to CVD-grown solar cells, investigated in this thesis. They exhibit approximately an identical structure and the same material properties because they were all obtained from the same production cycle. Nevertheless, the electronic properties are different because the hydrogen treatment was performed with different parameters (e.g. different durations and temperatures).

The structure of the samples is described in Sec. 3.1.1 and consists of a highly n-type doped emitter and a p-type doped absorber. The current-voltage characteristic of a one-sided abrupt junction under illumination in the two-diode model is given by [141]:

$$J = J_{01}\left(\exp\left(\frac{V}{n_1 V_t}\right) - 1\right) + J_{02}\left(\exp\left(\frac{V}{n_2 V_t}\right) - 1\right) + J_{SC} \qquad (7.1)$$

where J_{01}, J_{02} are the saturation current densities, $n_1 = 1$, $n_2 = 2$ the so called ideality factors, $V_t = \frac{kT}{q}$ the thermal voltage (with Boltzmann constant

k and elementary charge q). The photocurrent density under illumination J_{ph} is given by $J_{ph} = -J_{SC}$. Shunt and series resistance are neglected (justification will be given later).

The current contributions $J_1 = J_{01}\left(\exp\left(\frac{V}{n_1 V_t}\right) - 1\right)$, $J_2 = J_{02}\left(\exp\left(\frac{V}{n_2 V_t}\right) - 1\right)$ model defect recombination in the bulk and space-charge region (SCR), respectively. The saturation current densities J_{01}, J_{02} can be expressed in terms of diffusion length and other material related parameters [141, 160]:

$$J_{01} = \frac{qD_n n_i^2}{N_A}\frac{1}{L_n} \tag{7.2}$$

$$J_{02} = \frac{q\pi D_n n_i V_t}{\sqrt{2qN_A V_{bi}/\varepsilon}}\frac{1}{L_n^2} \tag{7.3}$$

Here q is the elementary charge, n_i the intrinsic carrier concentration, D_n the bulk diffusion constant of electrons, N_A the doping concentration in the absorber, V_{bi} the build-in voltage, ε the dielectric constant of the semiconductor and L_n the bulk diffusion length of the electrons. With Eq. 7.2 and 7.3, the ideal current-voltage characteristic (Eq. 7.1) depends only on D_n, N_A, V_{bi}, J_{SC} and L_n. To derive the equations of the two diode model, the following assumptions have been made:

1. abrupt depletion-layer approximation: the SCR is confined within abrupt boundaries
2. the Boltzmann relationships are valid (which is the case for non-degenerate semiconductors)
3. low-level injection: the concentration of minority carriers injected in the quasi-neutral region is low compared to the majority carrier concentration
4. current flow in the quasi-neutral regions is due to diffusion (no electric field, and therefore, no drift contribution is assumed in the absorber)
5. the quasi-neutral regions of the diode are considered infinitely long
6. solution only in one dimension: recombination at extended defects (like grain-boundaries) is not considered

Assumptions (5) and (6) are definitely not fulfilled in poly-Si thin film solar cells. Therefore, to account for limited absorber thickness and grain-boundary recombination, the bulk diffusion length L_n must be substituted by an effective

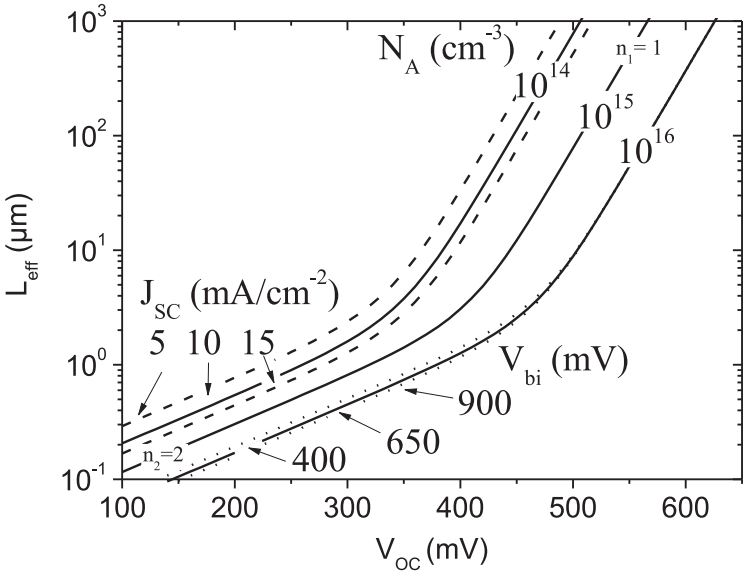

Figure 7.1: Effective diffusion length L_{eff}, computed as a function of open-circuit voltage V_{OC} for different doping levels N_A (solid lines, $J_{SC} = 10\,\mathrm{mA/cm^2}$, $V_{bi} = 650\,\mathrm{mV}$), different J_{SC} (dashed line) and different V_{bi} (dotted line).

diffusion length L_{eff}. The effective diffusion length must model the following types of recombination mechanism: recombination of carriers in the quasi-neutral regions, recombination at the grain-boundary and in the SCR and recombination at the front and rear side. The individual contributions to L_{eff} have been assessed for example in Ref. [3, 160]. If grain-boundary recombination is the limiting mechanism, the diffusion length L_{eff} can be approximated by [161]:

$$L_{grb} = \sqrt{\frac{D_n g}{2S^*_{grb}}} \tag{7.4}$$

which includes the grain size g and the grain boundary recombination velocity S^*_{grb} (in units of cm/s).

Under open circuit conditions (e.g. $J = 0$, $V = V_{OC} \gg V_t$) Eq. 7.1 becomes:

$$-J_{SC} \approx J_{01} \exp\left(\frac{V_{OC}}{V_t}\right) + J_{02} \exp\left(\frac{V_{OC}}{2V_t}\right) \tag{7.5}$$

Substituting J_{01}, J_{02} with Eq. 7.2 and 7.3 and L_n with L_{eff}, the equation can be solved for either V_{OC} or L_{eff} (see Ref. [160]) and gives a unique relationship between both quantities if D_n, N_A, V_{bi}, J_{SC} are specified. This relationship is displayed in Fig. 7.1. Here the effective diffusion length L_{eff} is computed as a function of V_{OC} for different doping levels N_A (solid lines, with

$J_{SC} = 10\,\mathrm{mA/cm^2}$, $V_{bi} = 650\,\mathrm{mV}$), different J_{SC} (dashed line) and different V_{bi} (dotted line). The bulk diffusion constant of electrons has been set to $D_n = 20\,\mathrm{cm^2 s^{-1}}$, which is a reasonable assumption for defect concentrations up to $10^{17}\mathrm{cm^{-3}}$ [162]. If the diffusion constant is lower, this would result in an overestimation of L_{eff} (not shown in Fig. 7.1).

Fig. 7.1 also visualizes the impact of the parameters N_A, J_{SC} and V_{bi} on the effective diffusion length $L_{eff}\,(V_{OC})$. The largest effect on $L_{eff}\,(V_{OC})$ is seen for different doping levels N_A. The influence of the short circuit current J_{SC} is not that pronounced, while the effect of different built-in voltages V_{bi} can be neglected. In the following V_{bi} is fixed to 650 mV. A change by $\pm$200 mV will not affect the results.

The two different slopes of L_{eff} in Fig. 7.1 are controlled by the dominating current contributions of either J_2 (lower V_{OC}) and J_1 (higher V_{OC}), as indicated by the corresponding ideality factors $n_2 = 2$ and $n_1 = 1$, respectively. Higher L_{eff} result in higher V_{OC} values and vice versa. Therefore V_{OC} represents an assessment to the electronic quality of the solar cell structure. Defects, lowering the minority carrier lifetime and therefore the diffusion length, will directly lead to a deterioration of $V_{OC.}$. This makes V_{OC} a very sensitive and valuable quantity for characterization.

Application of the Model As motivated in the beginning, the investigated samples exhibit approximately identical structure and material properties. Nevertheless, the electronic properties will be different because the hydrogen treatment was performed with different parameters (as presented in Chap. 5). Therefore defect concentration will vary and so will also V_{OC} and the effective diffusion length L_{eff}.

Suns-Voc measurements provide not only open circuit voltages but also pseudo-IV curves. From there, different device parameters like the pseudo-fillfactor (pFF) and the saturation current density ratios J_{01}/J_{SC} and J_{02}/J_{SC} can be obtained either directly from the pseudo-IV curve (in case of pFF) or by fitting the data (in case of $J_{01,02}$). Another convenient feature of Suns-Voc is that the measurement is conducted under open circuit conditions and the measurement reproduces the IV curve without the influence of the series resistance. Therefore the series resistance can be neglected.

In Fig. 7.2 , we analyze the obtained fillfactors pFF as a function of V_{OC}. The solid symbols correspond to samples after different hydrogen treatments. The samples were treated for different temperatures T_{HP} and durations $t_{plateau}$

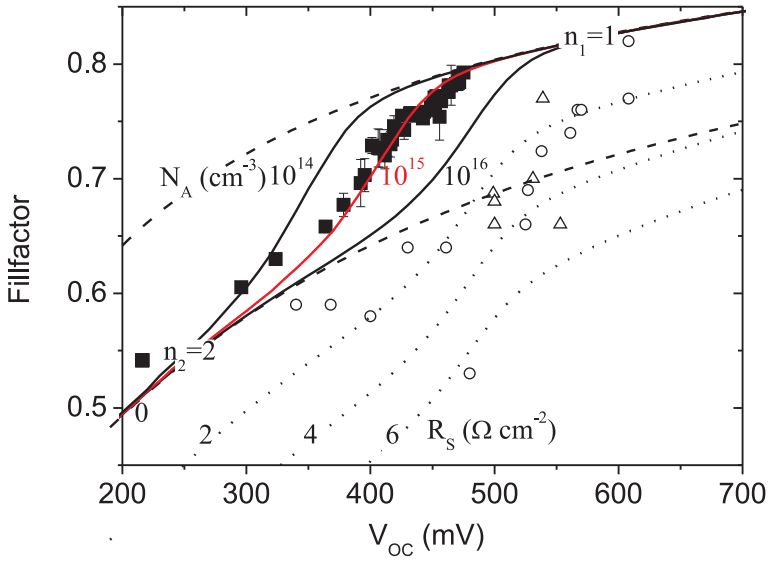

Figure 7.2: Fillfactor as a function of V_{OC}. Open data points are taken from Ref. [160], solid data point are taken from Suns-Voc measurements of PE-CVD-grown solar cell structures (this work). The solid lines model the fillfactor for different doping concentrations N_A via $L_{eff}(V_{OC})$ (with $J_{SC} = 10\,\mathrm{mA/cm^2}$, $V_{bi} = 650\,\mathrm{mV}$). For $N_A = 10^{16}$ cm^{-3} besides $R_S = 0\,\Omega\mathrm{cm}^{-2}$ also a series resistance of $R_S = 2$, 4 and $6\,\Omega\mathrm{cm}^{-2}$ is considered (dotted lines). The dashed lines are calculated, considering only either J_{01} or J_{02} (with an ideality factor of $n_1 = 1$ or $n_2 = 2$, respectively).

and thus exhibit different V_{OC} values and IV characteristics (here pFF). The fillfactors are obtained from pseudo-IV curves of the Suns-Voc data. The solid lines respond to simulations, where the fillfactor is obtained as follows. In a first step L_{eff} is calculated as a function of V_{OC} with given parameters N_A, $J_{SC} = 10\,\mathrm{mA/cm^2}$ (relationship of Fig. 7.1). In a next step the corresponding saturation current densities J_{01} and J_{02} are calculated from L_{eff} via Eq. 7.2 and 7.3, respectively. Finally the fillfactor is evaluated numerically from the simulated IV curves (Eq. 7.1).

The solid lines in Fig. 7.2 are computed for three different doping concentrations of $N_A = 10^{14}$, 10^{15} and 10^{16} cm^{-3}. For the doping concentration of $N_A = 10^{16}$ cm^{-3} besides $R_S = 0\,\Omega\mathrm{cm}^{-2}$ also a series resistance of $R_S = 2$, 4 and $6\,\Omega\mathrm{cm}^{-2}$ is considered (dotted lines).

The dashed lines are calculated, considering only either J_{01} or J_{02} (with an ideality factor of $n_1 = 1$ or $n_2 = 2$, respectively). As seen, the dashed lines confine the solid data points and represent upper ($n_1 = 1$) and lower limit ($n_2 = 2$). The open data point in Fig. 7.2 are taken from Ref. [160] for comparison and consist of poly-Si samples (circles) and µc-Si (triangles). Here the fillfactors were extracted from measured one-sun IV curves, which

essentially include the series resistance. Due to series resistance, the fillfactors are reduced, as also illustrated by the simulated dotted curves. The data points scatter significantly and are not confined between the dashed lines.

For V_{OC} values after HP higher than 380 mV, the solid data points of the passivated samples lie all very close along the simulated curve for $R_S = 0\,\Omega\text{cm}^{-2}$ and $N_A = 10^{15}$ cm^{-3}. This means that the samples can be modeled with the presented model, using at least very similar material parameters (i.e. D_n, N_A) for differently treated samples. A hydrogen treatment mainly improves the effective diffusion length L_{eff} in the samples. The dependence of L_{eff} on V_{OC} for $N_A = 10^{15}$ cm^{-3} was given in Fig. 7.1. The effective doping level of the samples (10^{15} cm^{-3}) is lower than the intended doping level ($\sim 10^{16}$ cm^{-3}). This could be due to either low doping activation or partially depleted grains which are caused by SCR, formed at grain boundaries [163].

Samples with $V_{OC} < 400\,\text{mV}$ are limited by SRH recombination in the SCR and are dominated by a non-ideal $n = 2$ behavior. Essentially in this range the solar cells need to be described with the two diode model and strong deviations from an ideal $n = 1$ behavior are observed. For $V_{OC} > 420\,\text{mV}$ the electronic properties are enhanced and the samples can be increasingly modeled by an ideality factor of $n = 1$.

The IV characteristics are best described by $N_A = 10^{15}$ cm^{-3} and an improvement of L_{eff} by passivation. For high V_{OC} values of ≥ 450 mV and a doping level of $N_A \geq 10^{15}$ cm^{-3} the model requires high effective diffusion lengths (Fig. 7.1) that are larger than the film thickness (1.5 µm). This implicates that the diffusion length will not only be limited by grain-boundary diffusion (Eq. 7.4) but possibly will also be controlled by recombination at the front and back surface. If recombination at the interfaces is high, the effective diffusion length cannot become larger than the film thickness. On the other hand, if recombination at the interfaces is low, the effective diffusion length can even become larger than it would be in the bulk. This effect can for example be observed in poor cells, where V_{OC} increases as the film thickness is reduced. The treatment of this effect can be studied for example in Ref. [164, 160]. To achieve high open circuit voltages, high bulk diffusion lengths are required together with low recombination velocities at the front and back surface.

The curve was modeled with a constant short-circuit current J_{SC}. Yet the hydrogen plasma treatment is expected to also improve the short-circuit current by improving the effective diffusion length L_{eff} and hence the charge carrier collection efficiency [8]. For low V_{OC} values J_{SC} should be lower than

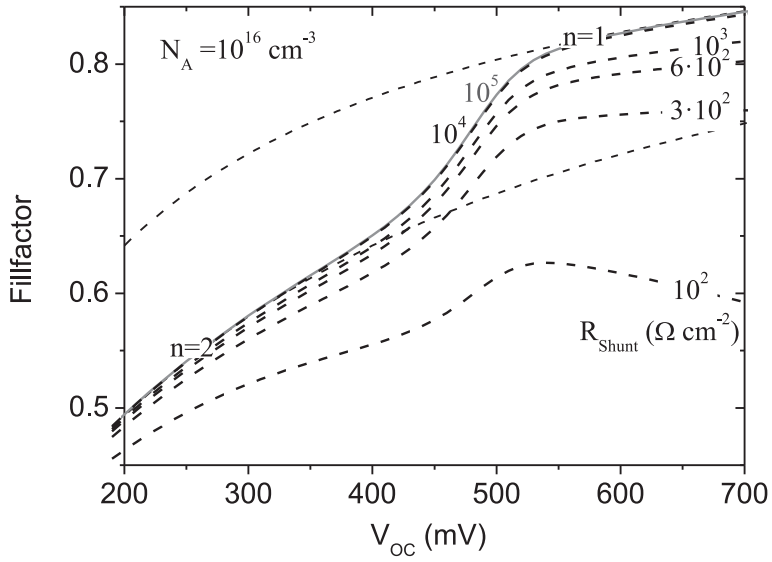

Figure 7.3: Fillfactor as a function of V_{OC} for different shunt resistances R_{Shunt} at a doping concentration $N_A = 10^{16}$ cm.

for higher V_{OC} values. The simulated L_{eff}-V_{OC} curves in Fig. 7.1 show that if J_{SC} is overestimated (in case of lower V_{OC}), it results in slightly underestimated diffusion lengths L_{eff}. Hence for lower voltages the simulated curves for the fillfactor in Fig. 7.2 would shift slightly to the left.

Until now, the shunt resistance R_{Shunt} was neglected. Fig. 7.3 shows the simulated fillfactor as a function of V_{OC} for different shunt resistances R_{Shunt} at a doping concentration $N_A = 10^{16}$ cm^{-3}. Small shunts (with large $R_{Shunt} \geq 10^4\,\Omega\text{cm}^{-2}$) do not lead to any degradation of the I-V characteristic and the fillfactor and can be neglected. Only shunts with $R_{Shunt} \leq 10^3\,\Omega\text{cm}^{-2}$ can lower the fillfactor significantly. As can be observed also from the solid data points in Fig. 7.2, the investigated samples did not exhibit any significant shunts.

It can be concluded that the measured IV characteristics of the samples can be described within a two diode model and an effective diffusion length L_{eff}. Within the model, other parameters than L_{eff} are not substantially modified by a hydrogen treatment. If the hydrogen treatment improves the V_{OC}, it is by means of increasing the effective diffusion length L_{eff}. L_{eff} is again directly linked to the lifetime τ_{eff} and to the effective recombination rate which depends on the defect concentration of the solar cell device. To achieve open circuit values larger than 450 mV, the effective diffusion length L_{eff} needs to become larger than the film thickness (1.5 µm). Low recombination at the

interfaces becomes more and more important.

To summarize:

- A two-diode model was applied, which establishes a link between the open-circuit voltage V_{OC} and an effective diffusion length L_{eff}. The I-V characteristic of samples that have received different hydrogen treatments can be modeled with similar material parameters, where L_{eff} is the only variable. A hydrogen treatment improves the V_{OC} by means of the effective diffusion length L_{eff} of the samples.

- V_{OC} represents an assessment to the electronic quality of the solar cell structure. Defects, lowering the minority carrier lifetime and therefore the diffusion length, will directly lead to a deterioration of V_{OC}.

- To achieve open circuit values larger than 450 mV, the effective diffusion length L_{eff} needs to become larger than the film thickness (1.5 µm). The modeling shows that low recombination at the interfaces becomes more and more important. Better material properties are needed.

8 Discussion

The experimental chapters have emphasized different topics of hydrogen passivation of poly-Si thin film solar cells:

- Chapter 4 has laid a focus on the role of plasma parameters like hydrogen pressure, electrode gap and plasma power. Simulations of the plasma reactor were carried out to establish a better understanding of the impact of these parameters on physically relevant quantities like H flux and density in the plasma and ion bombardment energy.

- Chapter 5 addressed the dynamics of the hydrogen treatment, i.e. the time and temperature dependence of the passivation process within the temperature range of 350 - 650°C.

- Chapter 6 investigated the interaction of passivation and material properties. Solar cells based on poly-Si absorbers, deposited by electron beam evaporation (EBE) are fabricated. The material properties of PE-CVD and EBE grown films were varied by different RTA treatments or by tuning the deposition temperature, respectively.

- The quality of the passivation process was characterized by open-circuit voltage measurements. A detailed discussion in Chapter 7 regarding defect passivation, material quality (L_{eff}) and solar cell performance (V_{OC}) validates this approach. V_{OC} represents an assessment to the electronic quality of the solar cell structure. Defects, lowering the minority carrier lifetime and therefore the diffusion length L_{eff}, will directly lead to a deterioration of $V_{OC.}$.

In the following, the presented results shall be briefly discussed in a mutual context.

Plasma Variations Plasma parameter variations of hydrogen pressure and electrode gap have led to optimized process conditions. Simulations of the plasma revealed that the optimum conditions do not correspond to a higher

but rather to a lower atomic H flux together with a minimum in the ion bombardment energy. The hydrogen passivation does not benefit from a higher atomic H flux. This is also supported by experiments with higher plasma powers which should lead to a higher H density in the plasma but which did not lead to any noticeable improvements in V_{OC}. A kinetic model was proposed that explains how passivation can be dominated by H diffusion rather than by the atomic H flux towards the surface. However, the equilibrium state of H diffusion will be controlled by thermodynamic equilibrium and the H concentration in the films will depend on the H chemical potential μ_H. The H chemical potential μ_H is in analogy to the Fermi level for electrons and controls the occupation of the density of states for H in the Si films. In thermodynamic equilibrium the H chemical potential μ_H will approach the value of the chemical potential $\mu_{H,plasma}$ in the plasma, which is given by [55]

$$\mu_{H,plasma} = kT \ln (c_H V_Q) \ . \tag{8.1}$$

Here c_H is the density of atomic H in the plasma and V_Q the quantum volume of H ($V_Q \approx 10^{-24}\,\mathrm{cm}^3$ at room temperature).

Higher concentrations c_H of H in the plasma should lead to a higher chemical potential μ_H and a higher density of H in the films. Higher concentrations c_H have not led to better V_{OC} results. It can be stated that V_{OC} after hydrogen passivation remains unaffected by a higher chemical potential μ_H.

This is also supported by the plasma power experiments and the temperature dependence of the V_{OC} after passivation. Since the product $c_H V_Q$ in Eq. 8.1 is smaller than unity, the chemical potential $\mu_{H,plasma}$ should increase for lower temperatures. However, higher temperatures have led to better passivation results.

Passivation Dynamic Investigations concerning the dynamics revealed that for $T_{HP} \leq 450°\mathrm{C}$ the passivation process is governed by an activated behavior. If a maximization of V_{OC} can be attributed to the complete H penetration of the Si films, the behavior can be attributed to H diffusion. Higher temperatures lead to a faster H diffusion and a faster passivation. The activation energy and diffusion prefactor were experimentally determined to be $E_A = 1.7 \pm 0.2$ eV and $D_0 \simeq 18\ \mathrm{cm}^2/\mathrm{s}$, respectively. This is in agreement with values for H diffusion from the literature (Fig. 5.9 on page 70) which exhibit a Meyer-Neldel behavior. The corrected activation energy $\bar{E_A}$ for H diffusion $D = D_{micro} \cdot \exp\left(-\frac{\bar{E_A}}{kT}\right)$ is calculated to be between 1.2 and 1.0 eV (for $T_{HP} = 350 - 450°\mathrm{C}$). In the

equilibrium model and also in the trapping model, $\bar{E_A}$ would correspond to the energy gap $\bar{E_A} = E_M - \mu_H$ between the migration barrier E_M for H and the chemical potential μ_H.

For temperatures $T_{HP} > 450$°C the saturation time $t_{saturation}$ remains constant within the error range. V_{OC} is usually maximized after 10 min and no activated behavior can be observed. If the diffusion coefficient D remains constant, in the diffusion models this would mean that the energy gap between E_M and μ_H must become larger and that the position of the chemical potential is decreased for $T_{HP} > 450$°C with increasing temperature. This would be in agreement with the discussion of Eq. 8.1 and has also been witnessed and discussed in the literature [55].

Passivation Temperature In terms of V_{OC}, an optimum treatment temperature around 550°C was identified for the poly-Si samples, grown by PE-CVD (Fig. 5.4). The hydrogen treatment at rather high temperatures is well suited for passivation of poly-Si solar cell structures.

The passivation of the main defects in poly-Si, namely dangling bonds, can be described by the reaction

$$\mathrm{H} + \mathrm{Si_{DB}} \rightleftharpoons \mathrm{SiH} \tag{8.2}$$

where mobile H is transferred to a Si dangling bond site ($\mathrm{Si_{DB}}$) and passivates the dangling bond (SiH). In parallel also new defects are generated, e.g. hydrogen breaking weak Si-Si bonds and Si-H bonds. The breaking of Si-H bonds is described by the reverse reaction of Eq. 8.2.

As already argued, the passivation of pre-existing dangling bonds should saturate with time and thermodynamic equilibrium should be reached. The defect passivation rate is exactly compensated by the rate of defect generation and in average no additional defects are created or annihilated.

Thermodynamic equilibrium is described by a minimum of the Gibbs free energy. The equilibrium state for reaction 8.2 is described by the law of mass action

$$N_{\mathrm{DB,1}}/N_{\mathrm{DB,0}} = \exp\left(-\left(E_{\mathrm{DB}} - \mu_{\mathrm{H}}\right)/kT\right) \tag{8.3}$$

where E_{DB} is the hydrogen binding energy of a dangling bond and $N_{\mathrm{DB,0}}$ and $N_{\mathrm{DB,1}}$ denote the density of unpassivated and passivated dangling bonds, respectively. The total density of pre-existing dangling bonds $N_{\mathrm{DB}} = N_{\mathrm{DB,0}} + N_{\mathrm{DB,1}}$ is preserved. The ratio of passivated to non-passivated pre-existing

dangling bonds should increase for lower temperatures and larger H concentrations (higher H chemical potential μ_{H}). The results on V_{OC} do however not reproduce this dependency. This suggests that the dynamic of the hydrogen passivation treatment in terms of V_{OC} is not only governed by thermodynamic equilibration of pre-existing dangling bonds. As discussed in Chapter 7, V_{OC} can be related to the lifetime and diffusion length of the charge carriers. It therefore represents a macroscopic electronic quantity that is sensitive to electrically active defects.

It was also observed that prolonged hydrogenation ($\geq$ 30 min) can lead to a degradation of V_{OC} after initially reaching a maximum value after 3 to 10 min. This behavior is only weakly pronounced within the temperature range of 500°C to 600°C, but more strongly pronounced for T_{HP} = 450°C and 650°C (Fig. 5.10). The analysis suggests a temperature dependent secondary defect generation.

Possible hydrogen mediated defect generation includes the breaking of weak Si-Si bonds, the formation of diatomic H_2^* complexes [151], the formation of H platelets [83, 84] and the passivation of dopants [69, 70, 71]. The breaking of weak Si-Si bonds includes the following reactions:

$$\mathrm{H} + (\mathrm{SiSi})_{\mathrm{weak}} \rightleftharpoons (\mathrm{SiH} + \mathrm{Si_{DB}})_{\mathrm{weak}} \tag{8.4}$$

$$\mathrm{H} + (\mathrm{SiH{+}Si_{DB}})_{\mathrm{weak}} \rightleftharpoons (\mathrm{SiH} + \mathrm{SiH})_{\mathrm{weak}} \tag{8.5}$$

The correlation energy between the single occupied $(\mathrm{SiH} + \mathrm{Si_{DB}})_{\mathrm{weak}}$ and the double occupied state $(\mathrm{SiH} + \mathrm{SiH})_{\mathrm{weak}}$ is negative [150]. Therefore the equilibrium of reaction 8.5 will be shifted to the right hand side $(\mathrm{SiH} + \mathrm{SiH})_{\mathrm{weak}}$ and the majority of the broken weak Si bonds will not contribute to the generation of dangling bonds [150]. The occupation of the single and double occupied states depend on the energetic levels with respect to the chemical potential μ_H, the correlation energy of the defect and the temperature [150]. Breaking of weak Si bonds and formation of H_2^* complexes and platelets will alter the H density of states, revealing the complexity of H passivation [165].

Also the passivation of dopants or plasma related defect generation could lead to a temperature dependant degradation of V_{OC}. The simulations of the plasma suggest that optimum plasma conditions could correspond to electrode gaps where the electric field and therefore the ion bombardment energy has a minimum. However, it is not yet fully understood what the degradation mechanism would be in this case. Investigations concerning temperature and

time dependence support a detrimental influence of the H treatment.

It can be concluded that V_{OC} does not depend significantly on the position of μ_H. The passivation process is not only controlled by thermodynamic equilibrium but temperature dependant defect generation and degradation of V_{OC} should play a role. The results on V_{OC} do not reveal the microscopic mechanism. Best results in terms of V_{OC} were achieved for $T_{HP} = 550-600$°C with a weakly pronounced optimum at $T_{HP} = 550$°C. Within this temperature range the observed decrease in V_{OC} for long passivation times is minimal.

Material Dependence Hydrogen passivation was also investigated in terms of its interplay with different material properties. The material properties were varied by different RTA treatments and using different poly-Si films, deposited by electron beam evaporation. The Si dangling bond concentration can be strongly reduced by HP. Samples of the SPC regime show a non-passivated to initial dangling bond ratio close to 1/10. The dangling bond density, observed after HP, therefore depends on the initial defect concentration. The equilibrium state for reaction 8.2 is described by Eq. 8.3. If only reaction 8.2 and a single defect level is considered (i.e. no dangling bond contributions from broken weak Si bonds), the density of unpassivated dangling bonds is given by

$$N_{\mathrm{DB},0} = N_{\mathrm{DB}} / \left(1 + \exp\left(-\left(E_{\mathrm{DB}} - \mu_{\mathrm{H}}\right)/kT\right)\right) \tag{8.6}$$

It depends on the energy level of the H chemical potential μ_{H} with respect to hydrogen binding energy E_{DB} and on the density of pre-existing dangling bonds N_{DB}. If the energy levels and the temperature are kept constant, the density of unpassivated dangling bonds depends only on the initial density of pre-existing bonds. In this simple model it can therefore be expected that the dangling bond concentration after hydrogen passivation is proportional to the dangling bond concentration before hydrogen passivation.

For $T_{dep} = 300$°C, the dangling bond concentration is lowered from $2.0 \cdot 10^{17}$ cm^{-3} to $2.5 \cdot 10^{16}$ cm^{-3} after hydrogen passivation. Carnel et al. reported a decrease in dangling bond concentration of directly grown fine-grained poly-Si by PE-CVD from $7 \cdot 10^{17}$ cm^{-3} to $1.1 \cdot 10^{17}$ cm^{-3} after 60 min of hydrogen passivation at 385°C [25]. Nickel et al. lowered the defect density of directly PE-CVD grown poly-Si from $1.8 \cdot 10^{18}$ cm^{-3} to $9.6 \cdot 10^{16}$ cm^{-3} after hydrogen passivation of several hours at 355°C [16]. This concentration could be reduced further to $2.2 \cdot 10^{16}$ cm^{-3} with an additional anneal at 160°C for 15 hours, creating a illumination sensitive metastable state [58].

It can be stated that hydrogen passivation as presented in this work is well suited to passivate Si dangling bonds during a very short treatment of 10 min. Nevertheless, it also depends on the initial dangling bond concentration, as shown for electron beam evaporated poly-Si after SPC. A minimum in Si dangling bond concentration is observed for $T_{dep} = 300°C$ before and after passivation, which corresponds to the minimum in FWHM of the crystalline TO-LO Si phonon peak, observed by Raman and coincides with the regime of largest grains and highest V_{OC} values after RTA and hydrogen passivation.

It could also be shown that high open circuit voltages rely on good material properties, which are not necessarily manifested solely in grain size. Without an RTA treatment, the direct-growth regime with small grains gives equally high or even higher V_{OC} values than the large grained material from the SPC regime. RTA affects primarily samples of the SPC regime. Possible reasons include a significant larger amount of intragrain defects, as observed in SPC material by Secco defect etching or a suggested lower dopant activation. Investigations concerning dopant activation are on-going.

After RTA and HP, open circuit voltages of 427 ± 5 mV have been obtained. Note that the fabrication of those samples has yet not been optimized in terms of thickness, doping and contacting. In addition no light trapping has been applied. Therefore further improvements can be expected. The results have provided valuable insights into processing and post-deposition treatments of high quality poly-Si solar cells.

In chapter 7 it was shown that the measured IV characteristics of the samples can be described within a two diode model and an effective diffusion length L_{eff}. Within the model, other parameters than L_{eff} are not substantially modified by a hydrogen treatment. If the hydrogen treatment improves the V_{OC}, it is by means of increasing the effective diffusion length L_{eff}. L_{eff} is again directly linked to the lifetime τ_{eff} and to the effective recombination rate which depends on the defect concentration of the solar cell device. To achieve open circuit voltages larger than 450 mV, the effective diffusion length L_{eff} needs to become larger than the film thickness (1.5 µm). Hence low recombination at the interfaces becomes more and more important.

Outlook The temperature dependence of defect passivation has only been investigated indirectly by V_{OC} measurements. The time dependent observations suggest that simultaneously with defect passivation, new defects are generated. The V_{OC} does not saturate with time but first reaches a maximum and

subsequently starts to degrade with prolonged HP. The degree of degradation seems to be temperature dependent, is minimal at $T_{HP} = 550°C$ and coincides with the observed optimum HP temperature. The microscopic mechanism of the defect generation is unknown and should be investigated. Dangling bond measurements could be done, investigating the time and temperature dependence of the hydrogen treatment. In addition also H effusion experiments should be performed, permitting to deduce the H density-of-states [166]. The experiments could reveal, to what extend H mediated defect generation and passivation affect the electronic properties of the solar cell devices.

Comparison of experiments and simulation in chapter 4 hint that the ion energy could play a role and should be minimized. Precise characterization of the plasma should be carried out to compare the plasma simulations with the experimental results and confirm the previous statement. To reduce ion energy, for example softer plasma conditions could be applied. Preliminary experiments at higher pressures of 4 mbar and 10 mbar led in our case to small further improvements. The best average V_{OC} was obtained at 4 mbar with 475 ± 3 mV (in comparison to preceding 463 ± 5 mV).

Device modeling has shown that high open circuit voltages larger than 450 mV demand an effective diffusion length L_{eff} larger than the film thickness. Recombination at the interfaces becomes more and more the limiting factor and good interface properties with low recombination velocities are required. For the rear side the influence of doping profile and thickness of the back surface field (BSF) layer could be investigated and the BSF layer should be optimized. Lower recombination velocities could also be obtained by a-Si:H/c-Si heterojunctions, as already applied in Si wafer based cell concepts. The bulk properties of poly-Si should also be improved. The experiments on material properties of electron beam evaporated Si have shown three desired requisites: (i) large grains, (ii) good grain boundary properties and (iii) low density of intragrain defects. Methods that bear the potential to achieve high quality, large-grained poly-Si films include for example laser crystallization (LC) [29] and electron-beam crystallization [167]. Once the material properties have been improved and interface recombination has been lowered, the poly-Si thin film solar cells should be more sensitive to variations in hydrogen passivation and further investigations, including for example softer passivation conditions, should be carried out.

9 Conclusion

A parallel plate rf plasma setup was used for the hydrogen passivation of poly-Si thin film solar cells. The reactor features a remote heating stage, capable of high temperatures up to 650°C. PECVD-grown test structures were used to investigate the role of plasma parameters like hydrogen pressure, electrode gap and power by open circuit voltage measurements. The plasma was characterized by measurements of breakdown voltage V_{brk} and power P_{brk}, necessary to ignite the plasma.

The dependence of the minimum in breakdown voltage V_{brk} on pressure p and electrode gap d was different to Paschen's law. With higher pressures, the value $p \cdot d$, corresponding to the minimum of the Paschen curve, shifted towards higher values. For each pressure, the best V_{OC} values were always obtained at the point of $p \cdot d$ that corresponded to the minimum in V_{brk}. It is remarkable that the optimum plasma conditions for the passivation of the poly-Si layers can be found by simple and fast voltage measurements at the RF electrode. The plasma reactor was simulated using a computational fluid dynamics code. The results indicate that optimum plasma conditions, characterized by a minimum in V_{brk}, correspond to a minimum in ion energy. On the other hand, V_{OC} does not benefit from a higher H flux and therefore a higher chemical potential μ_H.

CVD-grown solar cell test structures were also used to explore the dynamics of the hydrogen treatment, i.e. the time and temperature dependence. A plasma treatment in the lower temperature range ($\leq$ 400°C) is slow and takes several hours for the V_{OC} to saturate. Therefore this regime is irrelevant in industrial processes, requiring high throughput. Hydrogen passivation at rather high temperatures above 400°C seems to be well suited for defect passivation of poly-Si solar cell structures. Best results in terms of V_{OC} were achieved with a treatment at high temperatures ($\geq$ 500°C) with a weakly pronounced optimum at $T_{HP} = 550$°C. A short plateau time of 10 min and fast cool down steps make an industrial application feasible. Prolonged hydrogenation leads to a degradation in V_{OC}. The loss in V_{OC} is less pronounced within the observed

optimum temperature range (500°C − 600°C).

Electron beam evaporation (EBE) has been investigated as an alternative method to fabricate poly-Si absorbers, featuring high deposition rates of around 1 µm/min and a high cost reduction potential compared to CVD. The material properties of these layers can be tuned by alteration of substrate temperature during EBE and have been investigated in the temperature range of $T_{dep} = 200 - 700$°C. Raman and ESR have proven to be valuable characterization tools. The extracted FWHM of the c-Si Raman peak (520 cm^{-1}) correlated well with the Si dangling bond concentration, measured by ESR, and with average grain size. Largest grains were obtained after solid phase crystallization (SPC) of a-Si, deposited in the temperature range of 300°C. By HP, the Si dangling bond concentration is lowered by about one order of magnitude. The lowest dangling bond concentration of $2.5 \cdot 10^{16}$ cm^{-3} was found for $T_{dep} = 300$°C after HP (before HP: $2 \cdot 10^{17}$ cm^{-3}).

A correlation between grain size and V_{OC} could be observed only with an additional RTA treatment. Without RTA, samples with small grains ($T_{dep} >$ 400°C) exhibited equally high or even higher V_{OC} values than large grained samples ($T_{dep} < 400$°C). However, after an additional RTA treatment highest V_{OC} values were obtained for large grained material. The difference is suggested to be caused by intragrain defects, which are present in large grained samples. If present, apparently a larger improvement can be observed after RTA. Hydrogen passivation of EBE-grown films results in a large improvement in V_{OC} by +240 mV and +260 mV for non-RTA and RTA treated samples, respectively. The shape of the deposition temperature dependence of V_{OC} remains nearly unchanged. It appears that neither intragrain defects nor grain boundaries are passivated preferentially, resulting in similar improvements after passivation. Mini-modules recently prepared by EBE yield equivalent good results than the corresponding PECVD grown devices.

Hydrogen passivation of poly-Si films can be successfully achieved with a parallel plate rf H plasma treatment at elevated temperatures around 500°C to 600°C. Yet it seems that treatment induced defect generation causes degradation and should be minimized. In the future, further advances could be made going to softer passivation conditions, either at higher pressures or using a quasi-remote plasma setup. Also careful matching of RTA together with material properties and HP promises further improvements and should make poly-Si competitive with other thin film technologies.

Acknowledgement

I would like to thank everybody who has helped and encouraged me during the time that I worked on this thesis: my supervisors, colleagues, my friends and family and everybody else who has made this experience worthwhile. In particular my thanks go to:

- Prof. Dr. Bernd Rech for giving me the opportunity to work on this exciting project, for his support and guidance throughout my thesis.
- Prof. Dr. Uwe Rau, who showed interest in my study and agreed to evaluate my work.
- Dr. Stefan Gall for supervision of my work, being always supportive and approachable for stimulating discussions. Thanks go also to Stefan for closely proof-reading my thesis.
- Dr. Eleftherios Amanatides for the amount of work and energy that he put into the plasma simulations. He was always helpful in discussions and a very kind and amicable host during my stay in Patras.
- Dr. Björn Rau for helpful discussion on post-deposition treatments, his support for my work and close proof-reading. Most important he helped with technical issues (getting the passivation chamber to run and keeping it that way) and was a very pleasant and enjoyable room-companion. Thanks go also to Björn, Thomas Weber and Matthias Zelt for joint RTA experiments.
- CSG Solar AG and especially Dr. Jens Schneider for providing the samples needed for my studies.
- Prof. Dr. Norbert H. Nickel for his advice, sharing his knowledge about hydrogen passivation and whom I respect for his excellent physical competence.
- Dr. Moshe Weizman for helpful and stimulating discussions in all kinds of life situations. He was of great support and showed me how to measure those tiny spins. Thank you also for proof-reading parts of the thesis.
- Dr. Onno Gabriel for helpful and supporting discussions and for proof-reading the plasma related parts of the thesis.

- Dr. Klaus Lips, Dr. Jan Behrends and Dr. Yury Ryabchikov for helping me with the ESR measurements and being supportive.
- Prof. Dr. Bert Stegemann, Dr. Christiane Becker and Dr. Florian Ruske for carrying out joint experiments and creating a pleasant working atmosphere.
- Stefan Common, Pinar Dogan and her successor Tobias Sontheimer for their hard work on electron-beam evaporation, providing many samples. I greatly enjoyed working with you. Thanks go also to Tobias for proof-reading my thesis and being very supportive.
- Dr. Frank Fenske for taking care of the e-beam system and being mentor and support during my diploma thesis.
- Erhard Conrad for providing amorphous Si films, maintaining the cluster tool and sharing a room with me.
- Martin Muske and Stefan Common for cutting many samples.
- Tobias Hänel, who assisted me with technical issues.
- Lars-Peter Scheller and Maurizio Rozcen for giving me a helping hand many times.
- Carola Klimm for SEM and EBSD measurements.
- Kerstin Jacob and Anja Scheu, who helped with wet chemical treatments.
- Dr. Iris Didschuns and Dennis Schaffarzik for discussions and TPCD and SPV measurements.
- Gerhard Winkler and Andreas von Kozierowski for technical support.
- Marion Krusche for always helping me with administrative issues.
- my dear colleagues Kyu-Youl Lee, Mark Wimmer, Marc A. Gluba and Felice Friedrich

And last but not least I would like to thank everybody, family, friends and colleagues, who supported me to succeed in my work and fill my life with joy and happiness.

List of Publications

Publications

B. Gorka, B. Rau, P. Dogan, C. Becker, F. Ruske, S. Gall, B. Rech "Influence of Hydrogen Plasma on the Defect Passivation of Polycrystalline Si Thin Film Solar Cells" *Plasma Processes and Polymers* 6 (2009), p. S36-S40

B. Gorka, B. Rau, K.Y. Lee, P. Dogan, F. Fenske, E. Conrad, S. Gall, B. Rech "Hydrogen passivation of polycrystalline Si thin films by plasma treatment" *Proceedings of the 22nd European Photovoltaic Solar Energy Conference*, 3 - 7 September 2007, Milan, Italy. , 2007, p. 2024-2027

B. Gorka, P. Dogan, I. Sieber, F. Fenske, S. Gall "Low temperature epitaxy of silicon by electron beam evaporation" *Thin Solid Films* 515 (2007), p. 7643-7646

F. Fenske, **B. Gorka** "Highly phosphorus-doped crystalline Si layers grown by pulse-magnetron sputter deposition" *Journal of Applied Physics* 105 (2009), p. 074506/1-5

P. Dogan, **B. Gorka**, L.P. Scheller, I. Sieber, F. Fenske, S. Gall "Low temperature epitaxy of silicon using electron beam evaporation" *Proceedings of the 21st European Photovoltaic Solar Energy Conference*, Dresden, Germany, 2006, p. 1060-1063

B. Rau, T. Weber, **B. Gorka**, P. Dogan, F. Fenske, K.Y. Lee, S. Gall, B. Rech "Development of a rapid thermal annealing process for polycrystalline silicon thin-film solar cells on glass" *Materials Science and Engineering B*, 159-160 (2009), p. 329-332

B. Rau, M. Zelt, **B. Gorka**, S. Gall, B. Rech "High-temperature interval RTA as efficient defect annealing for polycrystalline Si thin-film solar cells on glass" *Proceedings of the 24th European Photovoltaic Solar Energy Conference*, Hamburg, Germany, 2009, p. 2344-2348

C. Becker, P. Dogan, **B. Gorka**, F. Ruske, T. Hänel, J. Behrends, F. Fenske, K. Lips, S. Gall, B. Rech "Polycrystalline silicon thin-film solar cells on ZnO:Al coated glass" *Proceedings of Amorphous and Polycrystalline Thin-Film Silicon Science and Technology,* Warrendale, Pa.: Materials Research Society, 2008, p. 1066-A06-01

C. Becker, T. Hänel, **B. Gorka**, K.Y. Lee, P. Dogan, F. Fenske, M. Berginski, J. Hüpkes, S. Gall, B. Rech "Solid phase crystallization of amorphous silicon on ZnO:Al for thin film solar cells". *Proceedings of the 17th International Photovoltaic Science and Engineering Conference,* Fukuoka, Japan, 2007, p. 1122-1123

C. Becker, F. Ruske, T. Sontheimer, **B. Gorka**, U. Bloeck, S. Gall, B. Rech "Microstructure and photovoltaic performance of polycrystalline silicon thin films on temperature-stable ZnO:Al layers" *Journal of Applied Physics* 106 (2009), p. 084506/1-7

C. Becker, P. Dogan, F. Ruske, **B. Gorka**, A. Sánchez-Vicens, E. Conrad, S. Gall, B. Rech, J. Hüpkes "Solid Phase Crystallized Silicon Thin-Film Solar Cells on Temperature-Stable ZnO:Al Contact Layers" *Proceedings of the 23rd European Photovoltaic Solar Energy Conference*, Valencia, Spain, 2008, p. 2045-2048

B. Stegemann, A. Schoepke, D. Sixtensson, **B. Gorka**, T. Lussky, M. Schmidt "Hydrogen passivation of interfacial gap state defects at UHV prepared ultrathin SiO2 layers on Si(111), Si(110), and Si(100)" *Physica E*, 41, 2009, p. 1019-1024

K.Y. Lee, P. Dogan, F. Ruske, **B. Gorka**, S. Gall, B. Rech, J. Hüpkes "The properties of poly-Si films grown on ZnO:Al coated borofloat glass by aluminium-induced layer exchange (ALILE) process" *Proceedings of the 23rd European Photovoltaic Solar Energy Conference*, Valencia, Spain, 2008, p. 2261-2264

S. Gall, K.Y. Lee, P. Dogan, **B. Gorka**, C. Becker, F. Fenske, B. Rau, E. Conrad, B. Rech "Large-grained polycrystalline silicon thin-film solar cells on glass" *Proceedings of the 22nd European Photovoltaic Solar Energy Conference*, Milan, Italy, 2007, p. 2005-2009

P. Dogan, E. Rudigier, F. Fenske, K.Y. Lee, **B. Gorka**, B. Rau, E. Conrad, S. Gall "Structural and electrical properties of epitaxial Si layers prepared by E-beam evaporation" *Thin Solid Films* 516 (2008), p. 6989-6993

C. Becker, E. Conrad, P. Dogan, F. Fenske, **B. Gorka**, T. Hänel, K.Y. Lee, B. Rau, F. Ruske, T. Weber, M. Berginski, J. Hüpkes, S. Gall, B. Rech "Solid-phase crystallization of amorphous silicon on ZnO:Al for thin-film solar cells" *Solar Energy Materials and Solar Cells* 93 (2009), p. 855-858

S. Gall, C. Becker, E. Conrad, P. Dogan, F. Fenske, **B. Gorka**, K.Y. Lee, B. Rau, F. Ruske, B. Rech "Polycrystalline silicon thin-film solar cells on glass" *Solar Energy Materials and Solar Cells* 93 (2009), p. 1004-1008

S. Gall, J. Berghold, E. Conrad, P. Dogan, F. Fenske, **B. Gorka**, K. Lips, M. Muske, K. Petter, B. Rau, J. Schneider, I. Sieber "Large-grained polycrystalline silicon on glass for thin-film solar cells" *Proceedings of the 21st European Photovoltaic Solar Energy Conference*, Dresden, Germany, 2006, p. 1091-1094

C. Secouard, C. Ducros, P. Roca i Cabarrocas, T. Duffar, **B. Gorka**, A. Focsa, F. Sanchette, "Solid phase crystallized silicon thin films deposited by high rate electron beam evaporation: improved structural and electrical properties" *Proceedings of the 23rd European Photovoltaic Solar Energy Conference*, Valencia, Spain, 2008, p. 2236-2241

P. Dogan, F. Fenske, L.P. Scheller, K.Y. Lee, **B. Gorka**, B. Rau, E. Conrad, S. Gall, B. Rech "Structural and electrical properties of epitaxial Si layers prepared by e-beam evaporation" *Proceedings of the 22nd European Photovoltaic Solar Energy Conference*, Milan, Italy, 2007, p. 2019-2023

S. Gall, C. Becker, E. Conrad, P. Dogan, F. Fenske, **B. Gorka**, K.Y. Lee, B. Rau, F. Ruske, B. Rech "Polycrystalline silicon thin-film solar cells on glass" *Proceedings of the 17th International Photovoltaic Science and Engineering Conference*, Fukuoka, Japan, 2007, p. 343-344

I. Gordon, D. Van Gestel, L. Carnel, G. Beaucarne, J. Poortmans, K.Y. Lee, P. Dogan, **B. Gorka**, C. Becker, F. Fenske, B. Rau, S. Gall, B. Rech, J. Plentz, F. Falk, D. Le Bellac "Advanced concepts for thin-film polycrystalline-silicon solar cells" *Proceedings of the 22nd European Photovoltaic Solar Energy Conference*, Milan, Italy, 2007, p. 1890-1894

Conferences

B. Gorka, T. Sontheimer, C. Becker, B. Rau, J. Behrends, K. Lips, S. Gall, B. Rech "Hydrogen passivation of electron beam evaporated polycrystalline Si for thin film solar cells" E-MRS Strassbourg, France, 2009 (Oral)

B. Gorka, B. Rau, P. Dogan, C. Becker, F. Ruske, S. Gall, B. Rech "Influence of Hydrogen Plasma on the Defect Passivation of Polycrystalline Si Thin Film Solar Cells" The Eleventh International Conference on Plasma Surface Engineering Garmisch-Partenkirchen, 2008 (Oral)

B. Gorka, B. Rau, K.Y. Lee, P. Dogan, F. Fenske, E. Conrad, S. Gall "Hydrogen Passivation of Polycrystalline Si Thin Films by Plasma Treatment" 22nd European Photovoltaic Solar Energy Conference, Milan, Italy, 2007 (Poster)

B. Gorka, P. Dogan, F. Fenske, I. Sieber, S. Gall "Low-temperature epitaxy of silicon by electron beam evaporation" E-MRS Spring Meeting 2006, Nice, France, 2006 (Poster)

Nomenclature

Symbols

$\bar{E_A}$	activation energy
$\bar{E_A}$	corrected activation energy
η	efficiency
$\mu_{H,plasma}$	H chemical potential in the plasma
μ_H	H chemical potential
τ_x	excess carrier lifetime, x = (eff, rad, Auger, defect)
ε	dielectric constant of a semiconductor
d	electrode gap
D_n	diffusion constant for electrons
$E_t^{(H)}$	energy level of deep traps for H
E_{BC}	energy level of hydrogen at a BC site
E_M	migration barrier for interstital hydrogen diffusion
E_t	energy level of deep traps for charge carriers
F_{max}	maximum electric field in the SCR
FF	fillfactor
g	grain size
$H^{-,0,+}$	charge state of hydrogen
$J_{01,02}$	saturation current densities
J_i	dark current density ($i = 1, 2$)

J_{ph}	photocurrent density
J_{SC}	short circuit current density
k	Boltzmann constant
L_{eff}	effective diffusion length
L_{grb}	grain-boundary dominated diffusion length
$N_t^{(H)}$	trap density of deep traps for H
$n_{1,2}$	ideality factors
N_A	acceptor concentration
n_d	defect density
n_i	intrinsic carrier concentration
p	pressure
P_{brk}	plasma breakdown power
pFF	pseudo-fillfactor obtained from SunsVoc measurements
q	elementary charge
Q^*_{grb}	grain boundary charge density (C/cm^2)
R^*_{grb}	surface recombination rate at the grain boundary (cm^{-2}s^{-1})
R_s	series resistance
R_{sh}	shunt resistance
R_x	recombination rate, x = (eff, rad, Auger, defect)
S^*_{grb}	surface recombination velocity at the grain boundary (cm/s)
T_d	tetrahedral interstitial site
T_g	transformation temperature
T_{dep}	deposition temperature
T_{HP}	plateau temperature during hydrogen passivation

T_{RTA} plateau temperature during RTA

V_{bi} built-in voltage

V_{brk} plasma breakdown voltage

V_{OC} open-circuit voltage

V_t thermal voltage ($\frac{k_b T}{q}$)

W thickness of solar cell

w width of depletion zone ($w \leq \frac{g}{2}$)

Abbreviations

µc-Si microcrystalline silicon

a-Si amorphous silicon

a-Si:H hydrogenated amorphous silicon

AIC aluminum induced crystallization

BC bond center

BSF back surface field

c-Si monocrystalline silicon

CVD chemical vapor deposition

db dangling bond

DOS density of states

EBE electron beam evaporation

ESR electron spin resonance

FWHM full width half maximum

HP hydrogen passivation

IV current-voltage

mc-Si multicrystalline Si

PECVD plasma-enhanced chemical-vapor deposition

poly-Si polycrystalline Si

PV photovoltaics

PVD physical vapor deposition

rf radio frequency

RTA rapid thermal annealing

SCR space-charge region

SEM scanning electron microscopy

SIMS secondary ion mass spectrometry

SiN:H hydrogenated silicon nitride

SPC solid phase crystallization

SRH Shockley-Read-Hall

VWW Van Wieringen and Warmoltz

Bibliography

[1] W. P. Hirshman and A. Schug. Photon **4** (2010).

[2] T. Chu, J. Lien, H. Mollenkopf, S. Chu, K. Heizer, F. Voltmer, and G. Wakefield. Solar Energy **17**, 4 (1975).

[3] R. Brendel. *Thin-film crystalline silicon solar cells: physics and technology* (Wiley-vch, 2003).

[4] M. Keevers, T. Young, U. Schubert, and M. Green. In *Proceedings of the 22nd European Photovoltaic Solar Energy Conference*, p. 1783 (Milan, Italy, 2007).

[5] H. Charles-Jr. and A. Ariotedjo. Solar Energy **24**, 4 (1980).

[6] P. Basore. In *Proceedings of 4th World Conference on Photovoltaic Energy Conversion*, p. 2089 (Waikoloa, Hawaii, 2006).

[7] P. Basore. In *Proceedings of the 21st European Photovoltaic Solar Energy Conference*, p. 544 (Dresden, Germany, 2006).

[8] M. J. Keevers, A. Turner, U. Schubert, P. A. Basore, and M. A. Green. In *Proceedings of the 20th European Photovoltaic Solar Energy Conference*, pp. 1305–1308 (Barcelona, Spain, 2005).

[9] L. Carnel, I. Gordon, K. V. Nieuwenhuysen, D. V. Gestel, G. Beaucarne, and J. Poortmans. Thin Solid Films **487**, 1-2 (2005).

[10] O. Nast. *The Aluminium-Induced Layer Exchange Forming Polycrystalline Silicon on Glass for Thin-Film Solar Cells*. Ph.D. thesis, Universität Marburg, Germany (2000).

[11] F. Falk and G. Andrä. Journal of Crystal Growth **287**, 2 (2006).

[12] N.-P. Harder, T. Puzzer, P. Widenborg, A. Aberle, and S. Oelting. Crystal Growth and Design **3**, 5 (2003).

[13] I. Gordon, D. Van Gestel, K. Van Nieuwenhuysen, L. Carnel, G. Beaucarne, and J. Poortmans. Thin Solid Films **487**, 1-2 (2005).

[14] P. Dogan, B. Gorka, L. Scheller, I. Sieber, F. Fenske, and S. Gall. In *Proceedings of the 21st European Photovoltaic Solar Energy Conference*, pp. 1060–1063 (Dresden, Germany, 2006).

[15] T. Matsuyama, N. Terada, T. Baba, T. Sawada, S. Tsuge, K. Wakisaka, and S. Tsuda. Journal of Non-Crystalline Solids **198-200**, Part 2 (1996).

[16] N. Nickel, N. Johnson, and W. Jackson. Applied Physics Letters **62** (1993).

[17] A. V. Wieringen and N. Warmoltz. Physica **22** (1956).

[18] W. Paul, A. Lewis, G. Connell, and T. Moustakas. Solid State Commun **20** (1976).

[19] J. I. Pankove. Applied Physics Letters **32**, 12 (1978).

[20] J. I. Pankove, M. A. Lampert, and M. L. Tarng. Applied Physics Letters **32**, 7 (1978).

[21] C. H. Seager and D. S. Ginley. Applied Physics Letters **34**, 5 (1979).

[22] C. H. Seager, D. S. Ginley, and J. D. Zook. Applied Physics Letters **36**, 10 (1980).

[23] C. Dube and J. Hanoka. In *Photovoltaic Specialists Conference, 2005. Conference Record of the Thirty-first IEEE*, pp. 883–888 (2005).

[24] L. Carnel, H. Dekkers, I. Gordon, D. Van Gestel, K. Van Nieuwenhuysen, G. Beaucarne, and J. Poortmans. IEEE electron device letters **27**, 3 (2006).

[25] L. Carnel. *Thin-Film Polycrystalline Silicon Solar Cells with Passivated Grain Boundaries and with a High Absorbance*. Ph.D. thesis, Katholieke Universiteit Leuven (2007).

[26] M. Terry, D. Inns, and A. Aberle. Advances in OptoElectronics **11** (2007).

[27] P. I. Widenborg and A. G. Aberle. Journal of Crystal Growth **306**, 1 (2007).

[28] O. Kunz, Z. Ouyang, S. Varlamov, and A. G. Aberle. Progress in Photovoltaics: Research and Applications **17**, 8 (2009).

[29] G. Andrä, J. Plentz, A. Gawlik, E. Ose, F. Falk, and K. Lauer. In *Proceedings of the 22nd European Photovoltaic Solar Energy Conference*, pp. 1967–1970 (Milan, Italy, 2007).

[30] A. Focsa, A. Slaoui, O. Tuzun, A. Bah, S. Roques, N. Zimmermann, and J. Muller. In *Proceedings of the 22nd European Photovoltaic Solar Energy Conference* (Milan, Italy, 2007).

[31] C.-T. Sah, J. Y.-C. Sun, and J. J.-T. Tzou. Journal of Applied Physics **54**, 2 (1983).

[32] R. Gale, F. J. Feigl, C. W. Magee, and D. R. Young. Journal of Applied Physics **54**, 12 (1983).

[33] T. Kamins and P. Marcoux. IEEE Elec. Dev. Lett. **1** (1980).

[34] T. King and K. Saraswat. IEEE Transactions on Electron Devices **41**, 9 (1994).

[35] A. Kohno, T. Sameshima, N. Sano, M. Sekiya, and M. Hara. IEEE Transactions on Electron Devices **42**, 2 (1995).

[36] J. Pankove and N. Johnson, editors. *Hydrogen in Semiconductors* (Academic Press, 1991).

[37] M. Stutzmann and J. Chevallier, editors. *Hydrogen in Semiconductors: Bulk and Surface Properties*. Physica B 170 (North-Holland, 1991).

[38] R. Street. *Hydrogenated Amorphous Silicon* (Cambridge University Press, 1991).

[39] N. H. Nickel, editor. *Hydrogen in Semiconductors II*, volume 61 (Academic Press, 1999).

[40] N. H. Nickel and I. E. Beckers. Phys. Rev. B **66**, 7 (2002).

[41] C. H. Seager and R. A. Anderson. Applied Physics Letters **53**, 13 (1988).

[42] C. H. Seager, R. A. Anderson, and D. K. Brice. J. Appl. Phys. **68**, 7 (1990).

[43] Y. Kamiura, M. Yoneta, and F. Hashimoto. Applied Physics Letters **59**, 24 (1991).

[44] F. Jiang, M. Stavola, A. Rohatgi, D. Kim, J. Holt, H. Atwater, and J. Kalejs. Applied Physics Letters **83**, 5 (2003).

[45] M. Stavola. In *14th Workshop on Crystalline Silicon Solar Cells and Modules: Materials and Processes*, pp. 134–142 (Winter Park, CO, 2004).

[46] C. S. Fuller and J. A. Ditzenberger. Journal of Applied Physics **27**, 5 (1956).

[47] B. Goldstein. Bull. Am.Phys. Soc. Ser. II 1 **1** (1956).

[48] J. Corbett, R. McDonald, and G. Watkins. Journal of Physics and Chemistry of Solids **25**, 8 (1964).

[49] K. Wada and N. Inoue. J. Cryst. Growth **71** (1985).

[50] C. S. Fuller and J. A. Ditzenberger. Journal of Applied Physics **25**, 11 (1954).

[51] S. Yanasigawa. Nippon Kinzoku Gakkaishi **26** (1962).

[52] A. D. Kurtz and R. Yee. Journal of Applied Physics **31**, 2 (1960).

[53] M. Barry and P. Olofsen. J. Electrochem. Soc. **116** (1969).

[54] N. Johnson, C. Herring, and C. Van De Walle. Phys Rev Lett **73**, 1 (1994).

[55] N. H. Nickel, W. B. Jackson, and J. Walker. Phys. Rev. B **53**, 12 (1996).

[56] M. Stavola. *Properties of Crystalline Silicon*, volume 20, pp. 511–521 (1999).

[57] C. Herring, N. M. Johnson, and C. G. Van de Walle. Phys. Rev. B **64**, 12 (2001).

[58] N. Nickel, W. Jackson, and N. Johnson. Phys Rev Lett **71**, 17 (1993).

[59] S. Pearton, J. Corbett, and J. Borenstein. Physica B: Condensed Matter **170**, 1-4 (1991).

[60] T. Zundel and J. Weber. Phys. Rev. B **46**, 4 (1992).

[61] S. J. Pearton. J. Electron. Mater. **14a** (1985).

[62] A. Mogro-Campero, R. P. Love, and R. Schubert. Journal of The Electrochemical Society **132**, 8 (1985).

[63] R. C. Newman, J. H. Tucker, A. R. Brown, and S. A. McQuaid. Journal of Applied Physics **70**, 6 (1991).

[64] W. B. Jackson, N. M. Johnson, C. C. Tsai, I.-W. Wu, A. Chiang, and D. Smith. Applied Physics Letters **61**, 14 (1992).

[65] C. Dube, J. I. Hanoka, and D. B. Sandstrom. Appl. Phys. Lett. **44**, 4 (1984).

[66] D. S. Ginley. Applied Physics Letters **39**, 8 (1981).

[67] T. Huang, I. Wu, A. Lewis, A. Chiang, and R. Bruce. IEEE Elec. Dev. Lett. **11** (1990).

[68] C. G. Van de Walle. Phys. Rev. B **49**, 7 (1994).

[69] J. I. Pankove, D. E. Carlson, J. E. Berkeyheiser, and R. O. Wance. Physical Review Letters **51**, 24 (1983).

[70] C.-T. Sah, J. Y.-C. Sun, and J. J.-T. Tzou. Applied Physics Letters **43**, 2 (1983).

[71] J. I. Pankove, R. O. Wance, and J. E. Berkeyheiser. Applied Physics Letters **45**, 10 (1984).

[72] N. M. Johnson, C. Herring, and D. J. Chadi. Phys. Rev. Lett. **56**, 7 (1986).

[73] M. Stavola, S. J. Pearton, J. Lopata, and W. C. Dautremont-Smith. Phys. Rev. B **37**, 14 (1988).

[74] S. J. Pearton, J. W. Corbett, and T. S. Shi. Applied Physics A: Materials Science & Processing **43**, 3 (1987).

[75] S. M. Myers, M. I. Baskes, H. K. Birnbaum, J. W. Corbett, G. G. DeLeo, S. K. Estreicher, E. E. Haller, P. Jena, N. M. Johnson, R. Kirchheim, S. J. Pearton, and M. J. Stavola. Rev. Mod. Phys. **64**, 2 (1992).

[76] J. L. Benton, C. J. Doherty, S. D. Ferris, D. L. Flamm, L. C. Kimerling, and H. J. Leamy. Applied Physics Letters **36**, 8 (1980).

[77] S. J. Pearton and A. J. Tavendale. Phys. Rev. B **26**, 12 (1982).

[78] S. J. Pearton and E. E. Haller. Journal of Applied Physics **54**, 6 (1983).

[79] R. Singh, S. J. Fonash, and A. Rohatgi. Applied Physics Letters **49**, 13 (1986).

[80] N. Nickel, N. Johnson, and J. Walker. Phys Rev Lett **75**, 20 (1995).

[81] N. Nickel, W. Jackson, N. Johnson, and J. Walker. Phys Status Solidi A **159**, 1 (1997).

[82] A. Leitch, V. Alex, and J. Weber. Physical Review Letters **81**, 2 (1998).

[83] N. M. Johnson, F. A. Ponce, R. A. Street, and R. J. Nemanich. Phys. Rev. B **35**, 8 (1987).

[84] N. H. Nickel, G. B. Anderson, and J. Walker. Solid State Communications **99**, 6 (1996).

[85] D. Kaplan, N. Sol, G. Velasco, and P. A. Thomas. Applied Physics Letters **33**, 5 (1978).

[86] C. Herring and N. M. Johnson. *Hydrogen in Semiconductors*, chapter 10, pp. 321–324 (Academic Press, 1991).

[87] C. Seager. *Hydrogen in Semiconductors*, p. 17 (Academic Press, 1991).

[88] T. Sakurai and H. D. Hagstrum. Phys. Rev. B **14**, 4 (1976).

[89] K. Cho, E. Kaxiras, and J. D. Joannopoulos. Phys. Rev. Lett. **79**, 25 (1997).

[90] C. Kisielowski-Kemmerich and W. Beyer. Journal of Applied Physics **66**, 2 (1989).

[91] I. A. Veloarisoa, M. Stavola, D. M. Kozuch, R. E. Peale, and G. D. Watkins. Applied Physics Letters **59**, 17 (1991).

[92] S. K. Estreicher, J. L. Hastings, and P. A. Fedders. Phys. Rev. B **57**, 20 (1998).

[93] M. I. Symko. Private communication to Estreicher (1998).

[94] B. L. Sopori, M. I. Symko, R. Reedy, K. Jones, and R. Matson.

[95] C. Seager and D. Ginley. Sandia Report **SAND82-1701** (1982).

[96] D. Sharp, J. Panitz, and D. Mattox. Journal of Vacuum Science and Technology **16** (1979).

[97] D. Hess. Annual Review of Materials Science **16**, 1 (1986).

[98] X. C. Mu, S. J. Fonash, G. S. Oehrlein, S. N. Chakravarti, C. Parks, and J. Keller. Journal of Applied Physics **59**, 8 (1986).

[99] E. M. Lawson and S. J. Pearton. physica status solidi (a) **72**, 2 (1982).

[100] N. M. Johnson, S. E. Ready, J. B. Boyce, C. D. Doland, S. H. Wolff, and J. Walker. Applied Physics Letters **53**, 17 (1988).

[101] L. Jastrzebski, J. Lagowski, G. W. Cullen, and J. I. Pankove. Applied Physics Letters **40**, 8 (1982).

[102] H. Nagel. In *Proceedings of the 14th European Photovoltaic Solar Energy Conference*, pp. 762–765 (Barcelona, Spain, 1997).

[103] J. Schmidt, M. Kerr, and A. Cuevas. Semiconductor Science and Technology **16**, 3 (2001).

[104] A. Rohatgi, D. S. Kim, K. Nakayashiki, V. Yelundur, and B. Rounsaville. Applied Physics Letters **84** (2004).

[105] R. Lüdemann. Materials Science and Engineering B **58**, 1-2 (1999).

[106] J. Hong, W. M. M. Kessels, W. J. Soppe, A. W. Weeber, W. M. Arnoldbik, and M. C. M. van de Sanden. Journal of Vacuum Science & Technology B: Microelectronics and Nanometer Structures **21**, 5 (2003).

[107] H. Dekkers and et al. In *Proceedings of the 20th European Photovoltaic Solar Energy Conference*, pp. 721–724 (Barcelona, Spain, 2005).

[108] Y. Matsumura and et al. In *14th PVSEC*, pp. 225–226 (2004).

[109] A. Slaoui, E. Pihan, I. Ka, N. Mbow, S. Roques, and J. Koebel. Sol Energ Mater Sol Cells **90**, 14 (2006).

[110] L. Carnel, I. Gordon, D. V. Gestel, G. Beaucarne, and J. Poortmans. Thin Solid Films **516**, 20 (2008).

[111] L. Carnel, I. Gordon, D. V. Gestel, G. Beaucarne, J. Poortmans, and A. Stesmans. Journal of Applied Physics **100**, 6 063702 (2006).

[112] L. Carnel, I. Gordon, D. V. Gestel, K. V. Nieuwenhuysen, G. Agostinelli, G. Beaucarne, and J. Poortmans. Thin Solid Films **511-512** (2006).

[113] A. Straub, D. Inns, O. Kunz, M. Terry, P. Widenborg, A. Sproul, and A. Aberle. In *Conference Record of the IEEE Photovoltaic Specialists Conference 2004*, pp. 1221–1224 (2005).

[114] T. Sontheimer, C. Becker, U. Bloeck, S. Gall, and B. Rech. Applied Physics Letters **95**, 10 101902 (2009).

[115] B. Rau, T. Weber, B. Gorka, P. Dogan, F. Fenske, K. Lee, S. Gall, and B. Rech. Materials Science and Engineering: B **159-160** (2009).

[116] http://www.schott.com/borofloat. *Schott Borofloat®33 Product information.*

[117] J. S. Montgomery, T. P. Schneider, R. J. Carter, J. P. Barnak, Y. L. Chen, J. R. Hauser, and R. J. Nemanich. Applied Physics Letters **67**, 15 (1995).

[118] C.-Y. Peng, C.-F. Huang, Y.-C. Fu, Y.-H. Yang, C.-Y. Lai, S.-T. Chang, and C. W. Liu. Journal of Applied Physics **105**, 8 083537 (2009).

[119] H. Richter, Z. P. Wang, and L. Ley. Solid State Communications **39**, 5 (1981).

[120] I. H. Campbell and P. M. Fauchet. Solid State Communications **58**, 10 (1986).

[121] C. P. Poole. *Electron Spin Resonance : A Comprehensive Treatise on Experimental Techniques* (Wiley, New York, 1983), 2nd edition.

[122] Bruker. *ER Series User's Manual* (Bruker Analytische Messtechnik GmbH, 1983), first edition.

[123] R. A. Sinton and A. Cuevas. In *Proceedings of the 16th European Photovoltaic Solar Energy Conference*, pp. 1152–1155 (Glasgow, UK, 2000).

[124] D. Pysch, A. Mette, and S. Glunz. Solar Energy Materials and Solar Cells **91**, 18 (2007).

[125] B. Gorka, B. Rau, K. Lee, P. Dogan, F. Fenske, E. Conrad, S. Gall, and B. Rech. In *Proceedings of the 22nd European Photovoltaic Solar Energy Conference*, p. 2024 (Milan, Italy, 2007).

[126] F. Paschen. Annalen der Physik **273**, 5 (1889).

[127] V. Lisovskiy, J.-P. Booth, K. Landry, D. Douai, V. Cassagne, and V. Yegorenkov. Europhys. Lett. , 1 (2008).

[128] B. Lyka, E. Amanatides, and D. Mataras. Japanese Journal of Applied Physics **45**, 10B (2006).

[129] E. Amanatides, S. Stamou, and D. Mataras. Journal of Applied Physics **90**, 11 (2001).

[130] P. Scheubert. *Modelling and Diagnostics of Low Pressure Plasma Discharges*. Ph.D. thesis, Technische Universität München (2001).

[131] S. Longo and P. Diomede. Plasma Processes and Polymers **6**, 5 (2009).

[132] V. Engel. *Ionized Gases*, p. 41 & 126 (Oxford University Press, London, 1965).

[133] E. Amanatides and D. Mataras. Journal of Applied Physics **89** (2001).

[134] A. Bogaerts, E. Bultinck, M. Eckert, V. Georgieva, M. Mao, E. Neyts, and L. Schwaederle. Plasma Processes and Polymers **6**, 5 (2009).

[135] P. Diomede, M. Capitelli, and S. Longo. Plasma Sources Science and Technology **14**, 3 (2005).

[136] L. Marques, J. Jolly, and L. L. Alves. Journal of Applied Physics **102**, 6 063305 (2007).

[137] K. Radouane, B. Despax, M. Yousfi, J. P. Couderc, E. Klusmann, H. Meyer, R. Schulz, and J. Schulze. Journal of Applied Physics **90**, 9 (2001).

[138] U. Hansen and P. Vogl. Phys. Rev. B **57**, 20 (1998).

[139] S. Inanaga, F. Rahman, F. Khanom, and A. Namiki. J. Vac. Sci. Technol. A **23**, 5 (2005).

[140] G. Pietsch. Applied Physics A: Materials Science & Processing **60**, 4 (1995).

[141] S. Sze and K. Ng. *Physics of semiconductor devices*, chapter 2.3, p. 90 (Wiley-Interscience, 2007).

[142] H. Kobayashi, K. Edamoto, M. Onchi, and M. Nishijima. The Journal of Chemical Physics **78**, 12 (1983).

[143] W. Beyer. *Hydrogen in Semiconductors II*, volume 61, p. 165 (Academic Press, 1999).

[144] R. A. Street, C. C. Tsai, J. Kakalios, and W. B. Jackson. Philosophical Magazine B **56** (1987).

[145] W. Meyer and H. Neldel. Z. tech. Phys **18** (1937).

[146] W. Beyer. physica status solidi (a) **159**, 1 (1997).

[147] R. Street and C. Tsai. Philosophical Magazine B **57** (1988).

[148] W. B. Jackson and C. C. Tsai. Phys. Rev. B **45**, 12 (1992).

[149] P. V. Santos, N. M. Johnson, R. A. Street, M. Hack, R. Thompson, and C. C. Tsai. Phys. Rev. B **47**, 16 (1993).

[150] S. Zafar and E. A. Schiff. Phys. Rev. B **40**, 7 (1989).

[151] K. J. Chang and D. J. Chadi. Phys. Rev. Lett. **62**, 8 (1989).

[152] W. Jackson and S. Zhang. Physica B: Condensed Matter **170**, 1-4 (1991).

[153] N. Johnson, C. Herring, C. Doland, J. Walker, G. Anderson, and F. Ponce. Materials Science Forum **83 - 87** (1992).

[154] M. Zelt. *Hochtemperaturbehandlung mit geringem thermischem Budget zur Verbesserung von polykristallinen Silizium-Dünnschichtsolarzellen.* Master's thesis, Hochschule für Technik und Wirtschaft Berlin (2009).

[155] S. Yokoyama, M. Hirose, and Y. Osaka. Japanese Journal of Applied Physics **20**, 1 (1981).

[156] F. Secco. J. Electrochem. Soc **119** (1972).

[157] P. Dogan, E. Rudigier, F. Fenske, K. Lee, B. Gorka, B. Rau, E. Conrad, and S. Gall. Thin Solid Films **516**, 20 (2008).

[158] D. V. Gestel, M. J. Romero, I. Gordon, L. Carnel, J. D'Haen, G. Beaucarne, M. Al-Jassim, and J. Poortmans. Applied Physics Letters **90**, 9 092103 (2007).

[159] I.-W. Wu, T.-Y. Huang, W. Jackson, A. Lewis, and A. Chiang. Electron Device Letters, IEEE **12**, 4 (1991).

[160] K. Taretto, U. Rau, and J. H. Werner. Journal of Applied Physics **93**, 9 (2003).

[161] R. Brendel. *Thin-film crystalline silicon solar cells: physics and technology*, p. 250 (Wiley-vch, 2003).

[162] S. Sze and K. Ng. *Physics of Semiconductor Devices* (Wiley-Interscience, 2007).

[163] J. Seto. J. Appl. Phys. **46**, 12 (1975).

[164] A. Goetzberger, J. Knobloch, and B. Voss. *Crystalline Silicon Solar Cells*, pp. 76–78 (Wiley-VCH, 1998).

[165] K. von Maydell and N. H. Nickel. Applied Physics Letters **90**, 13 132117 (2007).

[166] N. H. Nickel and K. Brendel. Appl. Phys. Lett. **82**, 18 (2003).

[167] I. Didschuns, C. Klimm, M. Schmidt, D. Amkreutz, C. Groth, K. Ong, and J. Müller. In *Proceedings of the 23rd European Photovoltaic Solar Energy Conference* (Valencia, Spain, 2008).